



Electronic and Aromatic Structure of Kekulene Studied by Density Functional Theory

By

Alexander Reichmann

Master's Thesis

Supervisor

Assoz.-Prof. Dr. Peter Puschnig

Institute of Physics
Karl-Franzens-University Graz

2021

Acknowledgements

Firstly, I would like to thank my supervisor, Professor Peter Puschnig, for his guidance, his continuous help and his patience.

In addition, I also wish to acknowledge my colleagues, my friends, my family and a special thanks goes to my father and Shan, for supporting and encouraging me.

Lastly, I also want to show my gratitude to the Karl-Franzens University of Graz for providing the computing facilities, used for the calculations, provided in this thesis.

Abstract

In this work the geometric, aromatic and electronic structure of the polycyclic hydrocarbon kekulene ($C_{48}H_{24}$) is studied using density functional theory (DFT), the harmonic oscillation model of aromaticity (HOMA), the simple Hückel molecular orbital theory and the probe particle model.

Experimental results of kekulene adsorbed on the two copper substrates, Cu(111) and Cu(110) are compared to DFT optimized calculations regarding the same metal-organic interfaces as well as theoretical calculations of gas phase kekulene.

Firstly, the energetically most favorable adsorption position of kekulene on the copper surfaces is obtained. With the optimized configuration the aromatic structure is investigated via the HOMA. In order to further analyze the aromaticity of kekulene, various theoretical models of kekulene are constructed by fixing the geometric structure of kekulene and by fixing electronic structure via the Hückel molecular orbital model. These models, the DFT optimized structures of free kekulene as well as the kekulene/Cu interface are examined in terms of their photoemission intensity, in order to gain insights into their electronic structure. The photoemission momentum maps are compared with photoemission momentum maps gained from angle resolved photoemission spectroscopy measurements. Furthermore, the density of states is investigated for the DFT optimized calculations and the charge density distribution and real space distribution of the frontier orbital nodal structure are investigated of all theoretical configurations. Finally the probe particle model is used in order to simulate non-contact atomic force microscopy and inelastic tunneling spectroscopy measurements.

From the theoretical, as well as the experimental results, it is concluded that the aromatic Clar's sextet model is a good predictor of kekulene's aromatic structure.

Kurzzusammenfassung

In dieser Arbeit wird die geometrische, aromatische und elektrische Struktur des polyzyklischen Hydrogenkarbonats Kekulene ($C_{48}H_{24}$) untersucht. Hierfür werden mehrere theoretische Ansätze verwendet, darunter die Dichtefunktionaltheorie (DFT), das sogenannte „harmonic oscillator model of aromaticity (HOMA)“, das einfache Hückel-Molekülorbital-Modell und das Probe-Particle-Modell.

Im ersten Teil der Arbeit liegt der Fokus auf der metall-organischen Grenzfläche Kekulene/Cu(111) und es wird versucht, durch Vergleiche zu experimentellen Resultaten und theoretischen Berechnungen von Kekulene in der Gasphase, die aromatische und elektrische Struktur von Kekulene genauer zu ergründen. Im ersten Schritt wird dafür die energetisch günstigste Adsorptionsgeometrie von Kekulene/Cu(111) bestimmt. Die aromatische Struktur von Kekulene ist bis heute noch ein offenes Problem und zwei Modelle haben sich als potentielle Lösungen durchgesetzt. Das erste Modell beschreibt Kekulene mithilfe von Clars Sextettregel und das zweite, superaromatische Modell, fasst Kekulene als zwei aromatische Annulene-Ringe auf, welche durch Einfachbindungen miteinander verbunden sind. Es wird versucht, diese zwei Modelle geometrisch als auch elektronisch nachzubilden, um diese dann mit den DFT-optimierten Strukturen und den experimentellen Daten vergleichen zu können. Geometrisch erfolgt dies über Anpassung der C-C Bindungslängen und elektronisch mithilfe des Hückel Molekülorbital Modells. Danach verwenden wir das Konzept des HOMAs um die aromatische Struktur von Kekulene genauer zu analysieren. Um einen Einblick in die elektronische Struktur von Kekulene zu bekommen, werden Photoemissions-Impulskarten von DFT-optimierten Strukturen der Kekulene/Cu Grenzflächen, sowie Kekulene in der Gasphase berechnet. Diese simulierten Impulskarten werden schließlich mit Resultaten aus ARPES Messungen verglichen. Zusätzlich wird die elektronische Struktur von Kekulene durch Berechnungen von Zustandsdichten und diverser Realraumdistributionen der Grenzorbitale erforscht. Die theoretischen als auch die experimentellen Resultate führen zu dem Schluss, dass das Clar'sche Sextettmodell am besten mit der aromatischen Struktur von Kekulene übereinstimmt.

Danach widmen wir uns der metall-organischen Grenzfläche Kekulene/Cu(110), um die Reaktion von Kekulene auf einer Oberfläche mit stärkerer Wechselwirkung zu untersuchen. Hierzu wurden dieselben Berechnungsmethoden verwendet wie für Kekulene/Cu(111), um die elektronische und die aromatische Struktur von Kekulene/Cu(110) zu analysieren. Zudem werden experimentelle Rastertunnelmikroskopiebilder (STM-Bilder) einer Monolage des Moleküls untersucht, die sich nach der Oberflächenreaktion auf der Cu(110) Oberfläche gebildet hat. Hierbei zeigt es sich, dass neben Kekulene auch noch andere, zunächst noch unbekannte, Moleküle identifiziert werden konnten. Eine Kekulene-ähnliche Struktur, welche potentiell bei der Synthetisierung von Kekulene entstehen kann, ein Isomere von Kekulene, genannt Iso-Kekulene, wurde näher beschrieben. Um diese neuen Moleküle auf der Cu(110) Oberfläche identifizieren zu können, wurden Simulationen von Rasterkraftmikroskopiebildern (AFM-Bildern) und STM-Bildern erzeugt, mithilfe des Probe-Particle Modells.

Table of Content

Acknowledgment	iii
Abstract	v
Kurzzusammenfassung	vii
List of Abbreviations	xii
1 Introduction	1
2 Background	3
2.1 Density Functional Theory	3
2.1.1 The Many Body Problem	3
2.1.2 Kohn-Sham Equations	6
2.1.3 Exchange and Correlation	8
2.1.4 Van der Waals Corrections	10
2.2 DFT in Practice	12
2.2.1 Vienna Ab-Initio Simulation Package	12
2.2.2 Equilibrium Geometries	13
2.2.3 Surfaces of Crystals and Adsorption of Molecules	14
2.3 Aromaticity	16
2.4 Density of States	18
2.5 Photoemission Intensity	19
2.6 Hückel Molecular Orbital Model	21
2.7 Probe Particle Model	22
3 Results	25
3.1 Kekulene on Cu(111)	26
3.1.1 Motivation	26
3.1.2 Geometric Optimization	27
3.1.3 Aromaticity	29

3.1.4 Hückel Model	35
3.1.5 Density of States	36
3.1.6 Photoemission Intensity	38
3.1.7 Electron Charge Density	43
3.1.8 Conclusions	46
3.2 Kekulene on Cu(110).....	47
3.2.1 Motivation.....	47
3.2.2 Geometric Optimization	48
3.2.3 Aromaticity	50
3.2.4 Electronic Structure	52
3.2.5 Iso-kekulene	55
3.2.6 Probe Particle Simulations	58
3.2.7 Conclusions.....	60
4 Summary	62
Appendix	65
Bibliography	67

List of Abbreviations

ARPES	angle resolved photoemission spectroscopy
AWA	annulene within annulene
BZ	Brillouin zone
B3LYP	Becke-3-Lee-Yang-Parr
DFT	density functional theory
DNA	deoxyribonucleic acid
DOS	density of states
fcc	face-centered cubic
GGA	generalized gradient approximation
HF	Hartree-Fock
HM	Hückel molecular orbital model
HOMA	harmonic oscillator model of aromaticity
HOMO	highest occupied molecular orbital
IETS	inelastic electron tunneling spectroscopy
MOPDOS	molecular orbital projected density of states
nc-AFM	non-contact atomic force microscopy
LDA	local density approximation
LEED	low-energy electron diffraction
LUMO	lowest unoccupied molecular orbital
PAH	polycyclic aromatic hydrocarbon
PAW	projector augmented wave
PBE	Perdew-Burke-Ernzerhof
pDOS	projected density of states

PPM	probe particle model
RNA	ribonucleic acid
STM	scanning tunneling microscopy
TS	Tkatchenko-Scheffler
VASP	Vienna Ab-initio Simulation Package
vdW	van der Waals
VWN	Vosko-Wilk-Nusair

1 Introduction

Organic compounds comprised entirely of hydrogen and carbon, so called hydrocarbons, are the most prevalently used compounds on the planet. Not only are they the makeup of the fossil fuels but also synthetic materials. For this reason they are considered the driving force of modern civilization. One of the most used hydrocarbons, benzene (C_6H_6), which was first described in its hexagonal shape by August Kekulé in the year 1865^[1,2], led to the discovery of a property many cyclic hydrocarbons share, but which is not restricted to just hydrocarbons. Today this property is known as aromaticity and it describes the increased stability of cyclic planar structures with π -bonds. Aromatic properties can be found in amino acids serving as basic building blocks of proteins and even our genetic code in the DNA and RNA consists of aromatic purines or pyrimidines. Therefore, understanding the fundamental questions of the concept of aromaticity is of great interest. A special class of polycyclic aromatic hydrocarbons, the cycloarenes^[3], have been useful in the quest of uncovering these questions, as well as uncovering fundamental questions of other useful structures, such as graphene nano pores^[4,5]. The most studied member of this class, kekulene ($C_{48}H_{24}$) is the main focus of this thesis.

Since its first synthesis in 1978^[6,7] kekulene's aromatic structure was not fully understood and has led to debates trying to explain it with two opposing models. On the one hand, the model following Clar's sextet rule^[8], describing kekulene's aromatic structure by maximizing the number of benzene like aromatic π -sextets connected via benzene units comprised by single and double bonds and, on the other hand, the superaromatic model or "annulene within annulene" (AWA) model^[9], which describes kekulene as two aromatic annulene circuits, namely the outer [30]-annulene ring and the inner [18]-annulene ring connected via single bonds. Although recent discoveries led to the favoring of the Clar sextet model for describing kekulene's aromaticity^[4], further analysis of kekulene's aromatic and electric properties are desirable. For example, the electronic structure of the frontier orbital plays a key role when it comes to the chemical and physical properties of a molecule. Especially when a transfer of electrons between atoms and molecules is observed, looking at the highest occupied molecular orbital (HOMO) and the lowest unoccupied molecular orbital (LUMO) can lead to a deeper understanding of many chemical processes.

For this purpose, further studies into the kekulene system were conducted by the Karl-Franzens-University Graz in cooperation with the Forschungszentrum Jülich of Aachen University, the Philipps-University of Marburg and the Westfälische Wilhelms University of Münster. The results of this cooperation have been recently published in ACS Nano^[10]. This thesis includes many of the theoretical calculations provided in this paper. In Ref. [10] firstly a new method of synthesizing kekulene was introduced, after which angle-resolved photoemission spectroscopy experiments as well as scanning tunneling microscopy measurements of kekulene on Cu(111) were compared with density functional theory (DFT) calculations. The electronic structure of the frontier orbitals were analyzed in more detail.

In this thesis, a more detailed look into some of these theoretical calculations will be provided as well as comparisons of theoretical results with experimental data from the organic/metal interface kekulene/Cu(110).

This thesis is organized as follows. In Chapter 2 the theoretical background will be reviewed. A short introduction into DFT is provided, as well as an overview of some methods used in applied DFT calculations. The concept of aromaticity, including some models describing its stabilization will be introduced. Methods of simulating the electronic structure via the photoemission intensity as well as the projected density of states are also provided. The Hückel molecular orbital model is then presented in more detail. And to finish off this chapter, an overview of the probe particle model is given, which is used to simulate microscopy imaging methods, with sub-atomic resolution, such as the non-contact atomic force microscopy and the inelastic tunneling spectroscopy.

The results of the calculations will be shown in Chapter 3. This chapter is divided into two sections, the first one concentrates on the organic/metal interface kekulene/Cu(111) while the second one focuses on kekulene/Cu(110). After studying the adsorption configuration of kekulene on Cu(111) in Section 3.1.2, the fundamental aromatic and electronic structure of kekulene is investigated in more detail. The harmonic oscillator model or aromaticity is used to examine kekulene's aromaticity through its geometric structure. After that, the Hückel model was used in addition to an investigation of kekulene's frontier orbitals to analyze kekulene's aromaticity through its electronic structure. In Section 3.2, the specific case of kekulene adsorbed onto Cu(110) was investigated in more detail. Firstly, the adsorption configuration was studied, after which the aromatic and electronic structure was compared to the previous case. Finally, sub-atomic microscopy simulations were done via the probe particle model.

2 Background

In this chapter an overview of the theoretical background, necessary throughout this thesis, is provided. Starting with an introduction into density functional theory (DFT), its mathematical foundation will be laid out as well as its computational application. Afterwards the concept of aromaticity will be explained, as well as the concept of density of states, the photoemission intensity and the Hückel molecular orbital model. To finish this chapter off, the probe particle model will be reviewed.

2.1 Density Functional Theory

2.1.1 The Many Body Problem

In order to study quantum mechanical systems, such as atoms and molecules, the wave functions of the system have to be calculated. The wave function is a probability amplitude for finding a system in a certain state at a given time. In the case of a stationary system, the wave function can be gained by solving the non-relativistic, time-independent Schrödinger equation,

$$\hat{H} |\psi\rangle = E |\psi\rangle, \quad (2.1)$$

where \hat{H} is the Hamiltonian, an operator accounting for the total energy of the system. E is the energy of a stationary state and $|\psi\rangle$ is the wave function.

When treating a many body system, for example a molecule, with a large number of electrons and nuclei, the Hamiltonian \hat{H} has to account for the interaction amongst those particles as follows:

$$\hat{H} = -\frac{1}{2} \sum_{i=1}^N \Delta_i - \frac{1}{2M_k} \sum_{k=1}^K \Delta_k + \frac{1}{2} \sum_{i,j \neq i} \frac{1}{|\vec{r}_i - \vec{r}_j|} + \frac{1}{2} \sum_{k,l \neq k} \frac{Z_k Z_l}{|\vec{R}_k - \vec{R}_l|} - \sum_{i=1}^N \sum_{k=1}^K \frac{Z_k}{|\vec{r}_i - \vec{R}_k|}. \quad (2.2)$$

Here, \vec{R}_k are the spatial coordinates of the atomic nuclei and \vec{r}_i denote the spatial coordinates of the N electrons. Note that K is the number of nuclei, with Z_k as the nuclear charge and M_k as the mass of the atomic nucleus k . It also has to be noted that throughout this work atomic units are used. Thus, Planck's reduced constant is set to $\hbar = 1$, the electron mass is set to $m_e = 1$ and the term $\frac{e^2}{4\pi\epsilon_0} = 1$.

The Hamiltonian in Eq. 2.2 is comprised of five terms, of which two account for the kinetic energy for the electrons and the nuclei and three describe the Coulomb interaction. The first two terms represents the kinetic energy of the electrons \hat{T}_e and the nuclei \hat{T}_n , respectively. The third term represents the Coulomb repulsion between the electrons \hat{V}_{ee} , while the fourth term represents the Coulomb repulsion between the nuclei \hat{V}_{nn} , and the last term represents the electron-nuclei attraction \hat{V}_{en} .

Since the above mentioned problem is only solvable for small molecules, consisting of only very few atoms, an approximation has to be made. Due to the very large mass difference between the nuclei and the electrons, one reasonable approach is to treat the nuclei as stationary with respect to the electrons. This means that the nuclear positions only enter as parameters in the remaining electronic Hamiltonian and the kinetic energy of the nuclei \hat{T}_n vanishes. This is known as the Born-Oppenheimer approximation^[11]. The resulting Hamiltonian then reduces to

$$\hat{H} = \hat{T}_e + \hat{V}_{ee} + \hat{V}_{ext}, \quad (2.3)$$

where \hat{V}_{ext} is external potential, which is given by the interaction between the electrons and the electro-static field of the nuclei. There are many sophisticated methods in order to solve the many body Schrödinger equation, such as the Hartree-Fock method^[14-18] which approximates the wave function $|\psi\rangle$ as a Slater determinant in the following way

$$\psi(r_1, \dots, r_N) = \frac{1}{\sqrt{N!}} \begin{vmatrix} \varphi_1(r_1) & \dots & \varphi_N(r_1) \\ \vdots & \ddots & \vdots \\ \varphi_1(r_N) & \dots & \varphi_N(r_N) \end{vmatrix}. \quad (2.4)$$

However, the problem with many of these methods is the computational costs, with which they scale. The computational costs of the Hartree-Fock method, for example, scales with N^4 , when taking into account also excited states in the Slater determinants, the scaling with the system size becomes even worse.

A more efficient method, scaling with N^3 , is to use the electron density $n_\sigma(\vec{r})$ to describe the system, instead of the wave function. The electron density can be obtained from the N -electron wave function $\psi(\vec{r}_1\sigma_1, \dots, \vec{r}_N\sigma_N)$ as follows:

$$n_\sigma(\vec{r}) = N \sum_{\sigma_2 \dots \sigma_N} \int d^3r_2 \dots \int d^3r_N |\psi(\vec{r}_1\sigma_1, \dots, \vec{r}_N\sigma_N)|^2. \quad (2.5)$$

Here $\vec{r}_1, \dots, \vec{r}_N$ are the spatial coordinates of the electrons and $\sigma_1, \dots, \sigma_N$ are their spin coordinates. Using the electron density instead of the wave function reduces the amount of variables that describe the electron system from $3N$ to 3.

As shown before (cf. Eq. 2.3 and Eq. 2.1), the wave function $|\psi\rangle$ is a functional of the external potential \hat{V}_{ext} , which means that the electron density $n_\sigma(\vec{r})$ is also dependent on the external potential. It has to be proven that this dependency is unique and that there are not two or more electron densities which derive from the same external potential. This was shown by Hohenberg and Kohn^[19] and is the first Hohenberg-Kohn theorem. The second Hohenberg-Kohn theorem states, that the ground state density $n_0(\vec{r})$ exactly minimizes the total energy $E[n(\vec{r})]$ and therefore leads to the ground state energy E_0 .

For the purpose of calculating the ground state energy E_0 from the electron density, the Rayleigh-Ritz variational principle^[20,21] can be used. The Rayleigh-Ritz variational principle approximates the ground state energy by minimizing the expectation value of the energy functional over the trial wave function ψ .

$$E[\psi] = \min_{\psi} \frac{\langle \psi | \hat{H} | \psi \rangle}{\langle \psi | \psi \rangle} \quad (2.6)$$

Minimizing the energy can also be done using trial densities $n(\vec{r})$, which are obtained by integrating the trial wave function ψ over all space variables except the first. This is known as the Levy's constraint-search formalism^[22], in which the minimization is separated into two steps.

Step one is to apply the Rayleigh-Ritz variation method (Eq. 2.6) onto the Hamiltonian (Eq. 2.3) such as to minimize all the electron wave functions ψ . All wave functions resulting in a given density $n(\vec{r})$ are denoted by $\psi \rightarrow n$. Since the wave function is normalized

$$\langle \psi | \psi \rangle = \sum_{\sigma_1 \dots \sigma_N} \int d^3 r_1 \dots \int d^3 r_N |\psi(r_1 \sigma_1, \dots, r_N \sigma_N)|^2 = 1, \quad (2.7)$$

the total energy functional $E[n(\vec{r})]$, depending on the electron density, can be obtained by

$$\begin{aligned} E[n(\vec{r})] &= \min_{\{\psi \rightarrow n\}} \langle \psi | \hat{H} | \psi \rangle = \min_{\{\psi \rightarrow n\}} \langle \psi | \hat{T} + \hat{V}_{ee} + \hat{V}_{ext} | \psi \rangle \\ &= \min_{\{\psi \rightarrow n\}} \langle \psi | \hat{T} + \hat{V}_{ee} | \psi \rangle + \int d^3 r v(\vec{r}) n(\vec{r}) \\ &= F[n(\vec{r})] + \int d^3 r v(\vec{r}) n(\vec{r}). \end{aligned} \quad (2.8)$$

Here the total energy is separated into the universal functional $F[n(\vec{r})]$ and the external potential \hat{V}_{ext} . Since the universal functional is independent of the external potential \hat{V}_{ext} it is therefore universal for a given system of N -electrons.

In the second step $E[n(\vec{r})]$ is then minimized, in order to gain the ground state energy E_0 . This is done under the constraint $\int n(\vec{r}) d^3 r = N$ (a fixed electron number) and using the Lagrangian multiplier μ .

$$\begin{aligned} E_0 &= \min_{n(\vec{r})} E[n(\vec{r})] \rightarrow \delta E = 0 \\ \delta \{ F[n(\vec{r})] + \int d^3 r v_{ext}(\vec{r}) n(\vec{r}) \} &= 0 \\ \frac{\delta F[n(\vec{r})]}{\delta n(\vec{r})} + v_{ext}(\vec{r}) &= \mu \end{aligned} \quad (2.9)$$

This should lay out the foundation necessary to calculate the ground state energy of the many body system. How it is applied is described in more detail in the following chapter.

2.1.2 Kohn-Sham Equations

Walter Kohn and Lu Jeu Sham^[23] suggested a scheme how to derive the ground state energy from the Hohenberg-Kohn theorems. The basic idea of this scheme is to consider a fictitious (auxiliary) system of N non-interacting electrons. This reduces the Hamiltonian to a sum of single-particle contributions without coupling, as follows

$$\hat{H}_s = \sum_{i=1}^n \hat{h}_s(\vec{r}_i) , \text{ with } \hat{h}_s(\vec{r}_i) = -\frac{1}{2}\Delta_i + v_s(\vec{r}_i) , \quad (2.10)$$

where $v_s(\vec{r})$ is the Kohn-Sham potential, which will differ from the case of interacting electrons mentioned before. The resulting N -electron wave function can be exactly written as a single Slater determinant (Eq. 2.4) which is denoted as $|\psi_s\rangle$. Using this Slater determinant in the Levy's constraint search formalism and minimizing the energy, as explained before leads to ground state energy as follows:

$$\begin{aligned} E[n(\vec{r})] &= \min_{\{\psi_s \rightarrow n\}} \langle \psi_s | \hat{H}_s | \psi_s \rangle \\ &= \min_{\{\psi_s \rightarrow n\}} \langle \psi_s | \hat{T} | \psi_s \rangle + \int d^3r v_s(\vec{r}) n(\vec{r}) \\ &= T_s[n(\vec{r})] + \int d^3r v_s(\vec{r}) n(\vec{r}). \end{aligned} \quad (2.11)$$

Here $T_s[n(\vec{r})]$ is the functional describing the kinetic energy of the system of non-interacting electrons. The ground state energy can then be obtained by minimizing over all densities corresponding to a fixed electron number N , as in Eq. 2.9:

$$\delta E[n(\vec{r})] = \frac{\delta T_s[n(\vec{r})]}{\delta n(\vec{r})} + v_s(\vec{r}) = \mu_s. \quad (2.12)$$

Since the resulting ground state density has to be the same as in the real system of interacting electrons Eq. 2.12 has to be the same as Eq. 2.9:

$$\frac{\delta T_s[n(\vec{r})]}{\delta n(\vec{r})} + v_s(\vec{r}) = \frac{\delta F[n(\vec{r})]}{\delta n(\vec{r})} + v_{ext}(\vec{r}). \quad (2.13)$$

Here, the difference of the Lagrangian multipliers μ and μ_s will be taken into account by the Kohn-Sham potential $v_s(\vec{r})$. To make progress, Kohn and Sham suggested to write the universal functional $F[n(r)]$ in the following way:

$$F[n(\vec{r})] = T_s[n(\vec{r})] + U[n(\vec{r})] + E_{xc}[n(\vec{r})]. \quad (2.14)$$

The second part, $U[n(r)]$ is the Hartree energy which describes the classical self-repulsion of the charge density $n(\mathbf{r})$. given by the following electrostatic integral:

$$U[n(\vec{r})] = \frac{1}{2} \int d^3r \int d^3r' \frac{n(\vec{r})n(\vec{r}')}{|\vec{r} - \vec{r}'|}. \quad (2.15)$$

The third part, $E_{xc}[n(\vec{r})]$ describes the exchange-correlation functional, which accumulates all yet unknown terms into one functional. $E_{xc}[n(\vec{r})]$ can be better understood by the introduction of the exchange correlation hole $\bar{n}_{xc}(\vec{r}, \vec{r}')$, which describes the phenomena, that an electron present at point \vec{r} reduces the probability of finding another one at \vec{r}' . $\bar{n}_{xc}(\vec{r}, \vec{r}')$ is created by the following three effects: the self-interaction correction, the Pauli exclusion principle and the Coulomb repulsion. The self-interaction correction cancels the self-interaction present in the Hartree energy, the Pauli exclusion principle keeps electrons with parallel spins apart from each other and the Coulomb repulsion keeps any electron apart from another. The exchange correlation energy functional $E_{xc}[n(\vec{r})]$ can then be interpreted as the interaction energy between each electron with the exchange correlation hole which surrounds it.

Inserting Eq. 2.14 into Eq. 2.13 then leads to the Kohn-Sham potential

$$v_s([n], \vec{r}) = v_{ext}(\vec{r}) + v_H([n], \vec{r}) + v_{xc}([n], \vec{r}). \quad (2.16)$$

Here the external potential

$$v_{ext}(\vec{r}) = \sum_k \frac{Z_k}{|\vec{r} - \vec{R}_k|} \quad (2.17)$$

and the Hartree potential

$$v_H([n], \vec{r}) = \frac{\delta U[n(\vec{r})]}{\delta n(\vec{r})} = \int d^3r' \frac{n(\vec{r}')}{|\vec{r} - \vec{r}'|} \quad (2.18)$$

can be calculated exactly from a given electron density. The remaining exchange-correlation energy

$$v_{xc}([n], \vec{r}) = \frac{\delta E_{xc}[n(\vec{r})]}{\delta n(\vec{r})}, \quad (2.19)$$

however, has to be approximated. This approximation will be reviewed in more detail in the following chapter. It has to be noted that, because the Hartree potential, as well as the exchange correlation potential depend on the electron density, these equations have to be solved self consistently. This iterative procedure starts from a set initial electron density, that is used to calculate the Kohn-Sham potential. Then Kohn-Sham orbitals $\varphi_i(\mathbf{r})$ are constructed, that are eigenstates of the following eigenvalue equation

$$\left[-\frac{1}{2}\Delta + v_s(\vec{r})\right]\varphi_i(\vec{r}) = \varepsilon_i\varphi_i(\vec{r}). \quad (2.20)$$

This are the so called Kohn-Sham equations. The wave functions $\varphi_i(\vec{r})$ (or Kohn-Sham orbitals) are then used to calculate a new electron density in the following way

$$n(r) = \sum_{i=1}^N |\varphi_i(\vec{r})|^2. \quad (2.21)$$

This new density is then compared to the initial density. If these two densities are identical then the ground state density has been found, if not then the Kohn-Sham scheme is repeated until the difference of the new density and old density converges.

2.1.3 Exchange and Correlation

Finding accurate approximations for the exchange-correlation energy is at the center of the density functional theory and getting reliable results depends on the usefulness of this approximation. On the other hand, its computational efficiency is also of great interest. Three widely-used approximations are presented here, which are of increasing complexity and therefore computational costs.

The first and simplest approximation of the exchange correlation energy functional, already introduced by Kohn and Sham is the local density approximation (LDA). The LDA approximates the total exchange-correlation energy at a point \vec{r} by the exchange-correlation energy of a uniform electron gas with equal density. This can be expressed with following equation:

$$E_{xc}^{LDA}[n] = \int d^3r n(\vec{r}) e_{xc}^{unif}(n(\vec{r})). \quad (2.22)$$

The corresponding exchange-correlation potential thus follows as

$$v_{xc}([n], \vec{r}) = \frac{\delta E_{xc}[n(\vec{r})]}{\delta n(\vec{r})} = \frac{\partial [n(\vec{r}) e_{xc}^{unif}(n(\vec{r}))]}{\partial n(\vec{r})}, \quad (2.23)$$

where the exchange correlation energy $e_{xc}^{unif}(n(\vec{r}))$ is commonly parameterized by quantum Monte-Carlo-Methods^[29,30].

The second approximation, which is mentioned here, also takes into account the gradient of the electron density. The inclusion of the gradient is done in order to incorporate the effects of inhomogeneities of the electron density. This method is called the generalized gradient approximation (GGA)^[31] and its most general form looks as follows:

$$E_{xc}^{GGA}[n] = E_x^{GGA}[n] + E_c^{GGA}[n] = \int d^3r f(n(\vec{r}), \nabla n(\vec{r})). \quad (2.24)$$

Here, the exchange-correlation energy is also split into the corresponding exchange and correlation part, $E_x^{GGA}[n]$ and $E_c^{GGA}[n]$, respectively. In this thesis the GGA approach of Perdew, Burke and Ernzerhof (PBE), also known as GGA-PBE, was used. In their work they defined the corresponding exchange and correlation energy as:

$$E_x^{GGA}[n] = \int d^3r n e_x^{unif}(n) F_x(s) \quad (2.25)$$

and

$$E_c^{GGA}[n] = \int d^3r n [e_c^{unif}(n) + H(r_s, \zeta, t)]. \quad (2.26)$$

The combined exchange-correlation energy is then defined as:

$$E_{xc}^{GGA}[n] = \int d^3r n e_x^{unif}(n) F_{xc}(s, r_s, \zeta), \quad (2.27)$$

where $F_x(s)$, $H(r_s, \zeta, t)$ and $F_{xc}(s, r_s, \zeta)$ are enhancement functionals, ζ is the spin polarization defined as $\zeta = \frac{n_\uparrow - n_\downarrow}{n_\uparrow + n_\downarrow}$, r_s is the Seitz radius and both s and t are dimensionless density gradients. These enhancement functionals are set to a specific form in order to ensure a universal, simplistic, non-empirical approach that at the same time can achieve good accuracy.

The third approximation mentioned here is the hybrid functional approach. Hybrid functionals are based on the idea of forming linear combinations of local and semi-local approximations with the Hartree-Fock (HF) exact exchange functional^[32]. The non-local HF exchange functional is given by:

$$E_x^{HF} = -\frac{1}{2} \sum_{i,j}^N \int d^3\vec{r} \int d^3\vec{r}' \frac{\phi_i^*(\vec{r}) \phi_j^*(\vec{r}') \phi_j(\vec{r}) \phi_i(\vec{r}')}{|\vec{r} - \vec{r}'|}. \quad (2.28)$$

Each component of the linear combination of the hybrid functionals is weighted by parameters, which are taken by fitting the functionals predictions to experimental or accurately calculated thermochemical data. Due to this mixing of local, semi-local and non-local functionals, a difference in behavior in the long-range and short-range interaction has to be taken into account^[33].

The hybrid functional used in this thesis is the B3LYP functional^[34-36], which is written as

$$E_{xc}^{B3LYP} = E_x^{LDA} + \alpha_0 (E_x^{HF} - E_x^{LDA}) + \alpha_x (E_x^{GGA} - E_x^{LDA}) + E_c^{LDA} + \alpha_c (E_c^{GGA} - E_c^{LDA}). \quad (2.29)$$

The three weighting parameter are given as $\alpha_0 = 0.2$, $\alpha_x = 0.72$ and $\alpha_c = 0.81$. The exchange and correlation functional of the GGA approximations, E_x^{GGA} and E_c^{GGA} , are given by the Becke 88^[37] exchange functional and the Lee-Yang-Parr^[38] correlation functional, respectively. The correlation functional of the LDA, E_c^{LDA} is given by the VWN^[39] local density approximation.

It has to be noted that although the hybrid functional scheme improves accuracy, it also heavily increases computational costs. This is the reason why in this thesis, for large systems, such as organic/metal interfaces, a GGA approximation was used instead.

2.1.4 Van der Waals Correction

Van der Waals (vdW) forces, first described by Johannes Diderik van der Waals in 1873^[40,41], which result from the interaction of either permanent dipoles or instantaneously induced dipoles (London dispersion force^[42,43]), play an important role when describing the bonding between molecules (intermolecular interactions) or the bonding of molecules to inorganic surfaces. In condensed matter physics typically the London dispersion force is referred to as the vdW force, because it has a non-classical origin. Using the exchange correlation methods of LDA, GGA or hybrid functionals, non-local and long-range correlations are neglected, so a correction, taking into account these vdW forces, needs to be made, in order to achieve more accurate results.

There are many different methods of vdW corrections used in DFT calculations. The ones used in this thesis are based on the works of Tkatchenko and Scheffler^[44].

In the Tkatchenko and Scheffler (DFT-TS) method, a correction energy E_{vdW} is calculated for the atoms inside a molecule or a solid, which is added to the total energy gained from LDA or GGA approach. This correction energy (vdW energy) is calculated by the atom's polarizability α , dispersion coefficients C_6 and atomic radii of the free atom R_0 , each of which is derived from their free counterparts. In addition, the effective atomic volumes are used, calculated by the Hirshfeld partitioning of the electron density. For the polarizability α , this looks as follows:

$$\frac{\kappa_A^{eff}}{\kappa_A^{free}} \frac{\alpha_A^{eff}}{\alpha_A^{free}} = \frac{V_A^{eff}}{V_A^{free}} = \frac{\int r^3 \omega_A(\vec{r}) n(\vec{r}) d^3\vec{r}}{\int r^3 n_A^{free}(\vec{r}) d^3\vec{r}}. \quad (2.30)$$

Here κ_A^i represents the proportionality constant between polarizability α_A^i and volume V_A^i and $\omega_A(\vec{r})$ is the Hirshfeld atomic partitioning weight, defined as:

$$\omega_A(\vec{r}) = \frac{n_A^{free}(\vec{r})}{\sum_B^N n_B^{free}(\vec{r})}, \quad (2.31)$$

where n_A^{free} and n_B^{free} are the electron densities of the free atoms A and B, respectively. The dispersion coefficient is also calculated, using the Hirshfeld atomic partitioning weight:

$$C_{6AA}^{eff} = \frac{\eta_A^{eff}}{\eta_A^{free}} \left(\frac{\kappa_A^{eff}}{\kappa_A^{free}} \right)^2 \left(\frac{V_A^{eff}}{V_A^{free}} \right)^2 C_{6AA}^{free}. \quad (2.32)$$

Here $\frac{\eta_A^{eff}}{\eta_A^{free}} \left(\frac{\kappa_A^{eff}}{\kappa_A^{free}} \right)^2$ is a proportionality constant. It is important to note, that this proportionality constant is not accurate for smaller atoms, but it increases in accuracy, the larger the system gets.

The vdW radius of an atom in a molecule is then given by

$$R_0^{eff} = \left(\frac{V^{eff}}{V^{free}} \right)^{\frac{1}{3}} R_0^{free}. \quad (2.33)$$

The dipole-dipole dispersion interaction, between two atoms, is given by the combination rule:

$$C_{6AB} = \frac{2C_{6AA}C_{6BB}}{\left[\frac{\alpha_B}{\alpha_A} C_{6AA} + \frac{\alpha_A}{\alpha_B} C_{6BB} \right]}. \quad (2.34)$$

Finally, the vdW energy can be calculated in following way

$$E_{vdW} = -\frac{1}{2} \sum_{A,B} f_{damp}(R_{AB}, R_A^0, R_B^0) C_{6AB} R_{AB}^{-6}, \quad (2.35)$$

where f_{damp} is a short-ranged damping function, dependent on the distance between atoms A and B, R_{AB} and the vdW radii R_A^0 and R_B^0 . f_{damp} is used to deal with the small distance singularity R_{AB}^{-6} .

2.2 DFT in Practice

2.2.1 Vienna Ab-Initio Simulation Package

The Vienna Ab initio Simulation Package (VASP)^[45-48] is a quantum chemistry program, that uses DFT for modelling materials on an atomic scale, e.g. electronic structure calculations, quantum-mechanical molecular dynamics calculations and it was also used for the calculations provided in this thesis. VASP uses a plane wave basis set which models the wave functions in the following way:

$$\phi_{\vec{k}}(\vec{r}) = \frac{1}{\sqrt{\Omega}} \sum_{\vec{G}}^{|\vec{G}| < \vec{G}_{cut}} c_{\vec{G}}(\vec{k}) e^{i(\vec{G}+\vec{k})\vec{r}}, \quad (2.36)$$

with Ω being the volume of the unit cell, \vec{k} the wave vector and \vec{G} the reciprocal space vectors. The number of \vec{G} vectors included in the summation is constrained by cut-off \vec{G}_{cut} . This cut-off is defined in regards to the maximal energy of the plane waves, also called the cut-off energy $E_{cut} = \frac{1}{2}|\vec{G}_{cut} + \vec{k}|^2$, which is usually in the range of a few hundred eV. This plane wave basis set implies periodic boundary conditions as follows:

$$\phi_{i\vec{k}}(\vec{r} + \vec{R}) = \phi_{i\vec{k}}(\vec{r}) \cdot e^{i\vec{k}\vec{R}}, \quad (2.37)$$

where i is the band index and \vec{R} is the spatial translation vector which results in an invariant Hamiltonian.

However, electron wave functions in close proximity to nuclei typically experience strong oscillations, which create problems when a plane wave basis set is used. To accurately describe these oscillations with plane waves, it requires a fine grid, which increases computational cost to an unreasonable amount. To circumvent this problem, VASP avoids such problems by utilizing the projector augmented wave (PAW)^[49-51] method. The PAW method is a combination of augmented wave methods with the pseudo-potentials approach^[52], to separate core from the valence electrons and change the wave function of the valence electrons in the region close to the nuclei into pseudo wave function $|\tilde{\phi}\rangle$, which is smooth and therefore less computationally demanding to describe, using plane waves.

2.2.2 Equilibrium Geometries

As mentioned before, the Kohn-Sham scheme (cf. Chapter 2.1.2) allows one to find the ground state electron density $n_0(\vec{r})$ and the ground state total energy E_0 of a given system. By varying the nuclear positions $(\vec{R}_1, \dots, \vec{R}_K)$, it is possible to obtain the configuration with the lowest total ground state energy, which resembles the equilibrium geometry of the system.

Instead of searching for the equilibrium geometry by minimizing the total energy, a more efficient way is to make use of the Hellman-Feynman theorem^[33]. In the general case, the Hellman-Feynman theorem links the derivative of the total energy with respect to some parameter λ to the expectation value of the derivative of the Hamiltonian with respect to the same parameter, as follows:

$$\frac{dE(\lambda)}{d\lambda} = \langle \psi(\lambda) | \frac{d\hat{H}(\lambda)}{d\lambda} | \psi(\lambda) \rangle. \quad (2.38)$$

Applied to the nuclear coordinates this is then used to derive an expression for the forces onto each nucleus also known as the electro-static force theorem^[18]:

$$\vec{F}_k = \frac{\partial E}{\partial \vec{R}_k} = \langle \psi | \frac{\partial \hat{H}}{\partial \vec{R}_k} | \psi \rangle = \int d^3r n(\vec{r}) \frac{Z_k(\vec{r} - \vec{R}_k)}{|\vec{r} - \vec{R}_k|^3} + \sum_{l \neq k} \frac{Z_k Z_l (\vec{R}_k - \vec{R}_l)}{|\vec{R}_k - \vec{R}_l|^3}. \quad (2.39)$$

The geometry of the system can now be varied, to minimize the electro-static forces, acting onto each nucleus. As a result, the total energy of the system will also be minimized. In larger systems with a large amount of degrees of freedom, it can still take many geometric steps to find the equilibrium geometry. At each step, the Kohn-Sham equations have to be solved self-consistently to gain the density $n(\vec{r})$ which then has to be used to calculate the atomic forces with Eq. 2.39.

2.2.3 Surfaces of Crystals and Adsorption of Molecules

In this thesis, DFT calculations are used to study properties of organic/metal interfaces. There is a number of interesting properties that can be derived from DFT calculations that will be briefly discussed in this chapter.

Firstly, the adsorption geometry of the system has great importance, when studying at organic/metal interfaces. In this thesis, a copper substrate (fcc crystal), in the Cu(110) and Cu(111) facet, has been used. A representation of those two surfaces can be seen in Fig. 2.1. The directions in dependence of each facet are also depicted which will be later used in order to describe the orientation of the molecule on top of the crystal surface. There are four different adsorption positions for each Cu facet, which are marked in red.

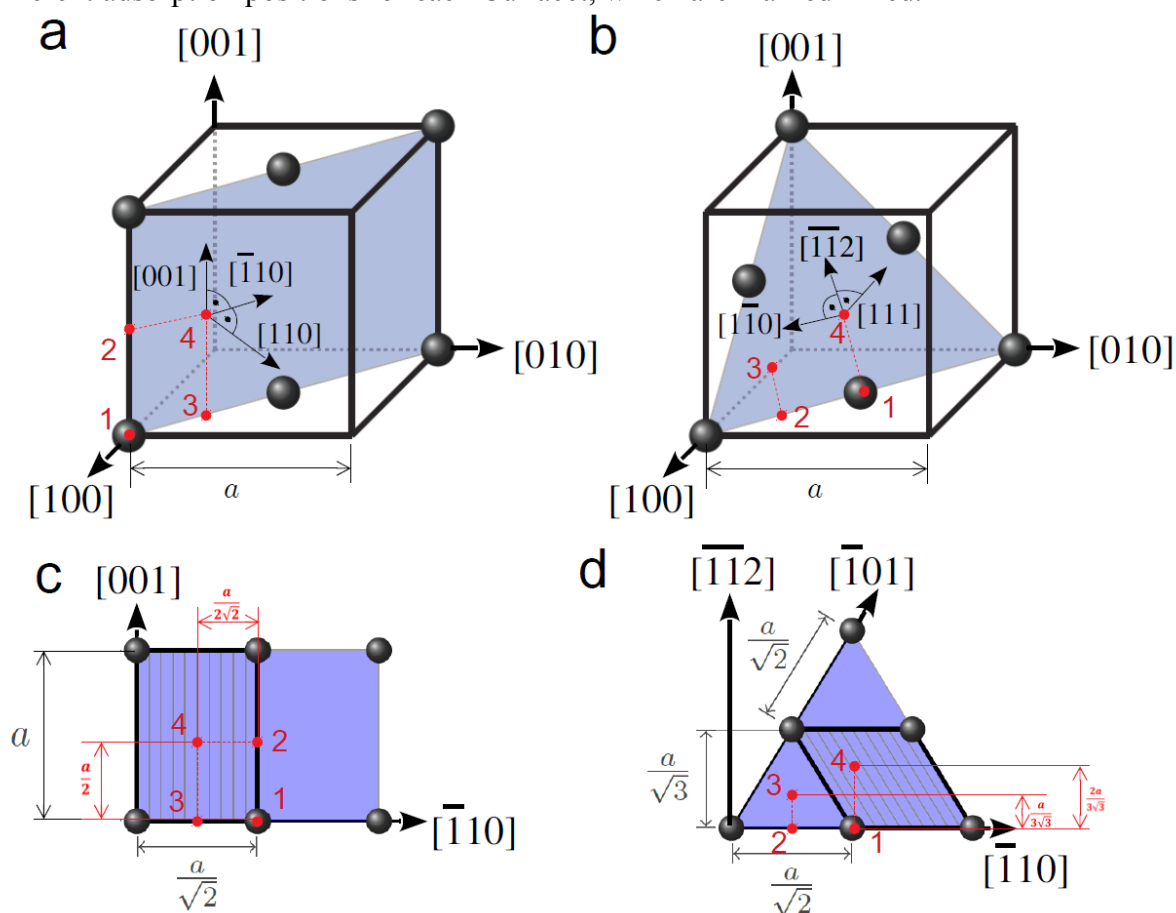


Fig. 2.1 (a) and (c) depict the (110) facet of the fcc crystal, with the adsorption positions 1- top, 2-short bridge, 3-long bridge and 4-hollow. (b) and (d) depict the (111) facet of the fcc crystal with the adsorption positions 1- top, 2-bridge, 3-hollow fcc and 4- hollow hcp. The difference in the hollow fcc and hollow hcp are also in their position in regards to the second and third layer of the crystal slab, with the hcp being directly above the top position of the second layer and the fcc being directly above the top position of the third layer of the crystal. The area marked with diagonal lines in (d) and vertical lines (c) is the unit cell of the corresponding facet. (This picture was taken from Ref. [53] and then later modified)

Another important property is the adsorption height, which is defined as the vertical distance of the adsorbate to the substrate. In this thesis, the adsorption height was calculated by taking the average height of adsorbates atoms (also a differentiation was made between kekulene's carbon atoms and the full kekulene molecules including the hydrogen atoms) and subtracting it from the average height of the top layer of the Cu substrate.

When using a basis set which is periodic in all three Cartesian directions (such as plane waves), the only way to simulate a surface is to cut out a slab of a certain thickness, which itself is also periodic in all three Cartesian directions. This approach is referred to as the repeated slab approach^[53] of which an illustration can be seen in Fig. 2.2, where it was used on the organic/metal interface of kekulene/Cu(111) with 3 layer of Cu atoms.

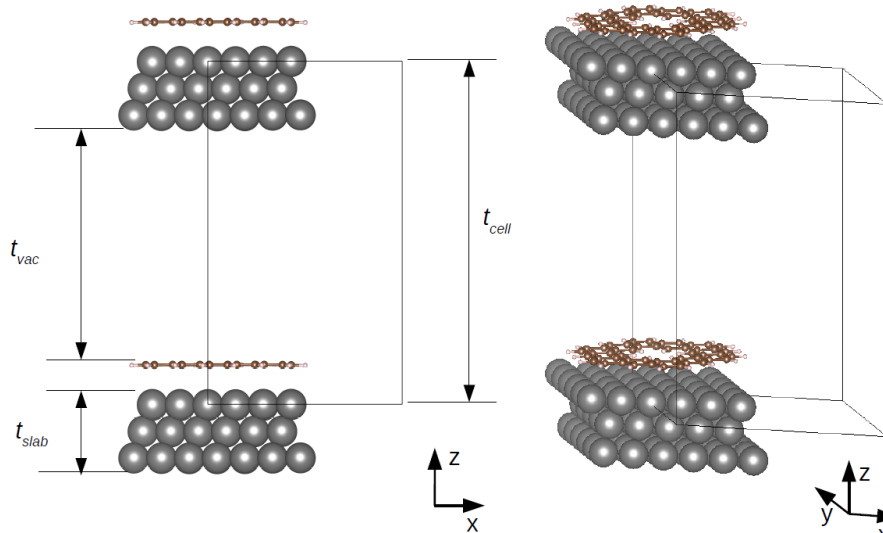


Fig. 2.2 Repeated slab approach shown on the kekulene/Cu(111) system with 3 layers of Cu in the x,z plane (left) as well as in an perspective view (right). t_{vac} describes the thickness of the vacuum layer, t_{slab} the thickness of the slab and t_{cell} the thickness of the cell.

The number of metal layers used is of key importance, when simulating organic/metal interfaces. Of course, the more layers are used the higher is the resemblance to the real metal surface. However, with increasing the number of atoms in the system, the computational cost will also increase, as mentioned before in Chapter 2.1 by a factor of N^3 . The thickness of the vacuum layer is also important since it isolates each repeated system from each other, consequently it should be large enough to prevent interactions among them. Therefore the appropriate arrangement of metal layers and vacuum layer thickness has to be carefully chosen.

When adsorbing molecules onto a crystal surface, another property of interest is the adsorption energy, which describes the energy gain when two initially separated systems from a combined system. The adsorption energy can be calculating by taking the difference between the combined system and each isolated system of surface and molecule, as follows:

$$E_{adsorb} = E_{Combined} - (E_{substrate} + E_{molecule}), \quad (2.40)$$

where $E_{Combined}$ represents the total energy of the combined system, $E_{molecule}$ represents the total energy of the isolated (free) molecule and $E_{substrate}$ represents the total energy of the isolated substrate. So in order to compute the adsorption energy, three separate DFT calculations need to be performed.

2.3 Aromaticity

The concept of aromaticity has its origin in cyclic planar π -electron compounds, such as the hydrocarbon benzene and its derivatives. It has been shown that these cyclic compounds are more stable and do not break apart, to react with other substances as easily as their chain analogues. The most common model of an aromatic ring, benzene was first developed by August Kekule 1865^[1,2], by combining six alternating single and double C-C bonds. Aromatic structures, however, show bond lengths roughly equalized, in between usual single and double bond lengths, for their respective bond type. This equalization can be attributed to the delocalization of the molecules π -electrons. It is important to note here, that the number of delocalized π -electrons of a system with aromaticity is always even, but not a multiple of 4, so $(4n + 2)$ π -electrons, where n is a whole number. This is called Hückel's rule and is a topological description of aromaticity, which can already be seen to be fulfilled for the smallest aromatic cyclic hydrocarbons: benzene (6 π -electrons), naphthalene (10 π -electrons), anthracene (14 π -electrons), tetracene (18 π -electrons) and pentacene (22 π -electrons). Delocalization increases the stability of the molecule and can be observed by the increase of the magnetic susceptibility^[55], when aromatic molecules are exposed to an external magnetic field. This increase is due to the formation of a ring current created by the delocalized π -electrons. Molecules with $4n$ π -electrons on the other hand, that show similar characters to the ones found in aromatic structures, such as a planar form and the arrangement of all contributing atoms in one or more rings, are called anti-aromatic.

Another topological description is Clar's sextet rule^[10], which only refers to benzenoid hydrocarbons. It postulates that the number of disjoint aromatic π -sextets (i.e. benzene) is required to be maximal and the number of benzene units, with localized double and single bonds are minimal. This rule provided reliable predictions, when looking at delocalization patterns of polycyclic aromatic hydrocarbons (PAHs). An illustration of Clar's sextet rule can be seen in Fig. 1(d), where the PAH kekulene is depicted, with the aromaticity of its twelve benzene compounds arranged as described by Clar's rule.

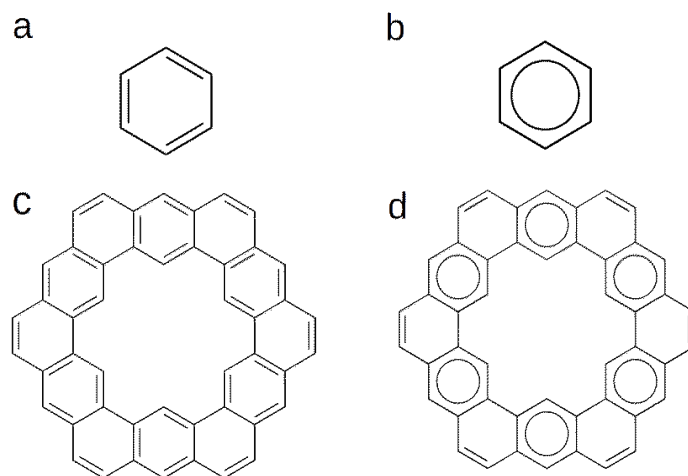


Fig.2.3 Different chemical models of benzene (a,b) and kekulene (c,d) in regards to their aromaticity depicted by the CC-bond lengths. (a) benzene with alternating single and double bonds. (b) aromatic benzene(π -sextets) with six equalized bond lengths due to the delocalization of its π -electrons. (c) kekulene (benzene derivative) drawn as a sequence of single and double bonds only. (d) kekulene according to Clar's sextet rule, with alternating disjointed sextets and benzene rings that show single and double bonds in between.

There are many more methods of describing aromaticity, such as more topological ones (double-bond equivalents), approaches using thermochemical properties such as the molecular energy (enthalpy), theories using magnetic properties of aromatic molecules with the help of the diamagnetic susceptibility exaltation $\Delta\chi$, methodologies using the electron density distribution by using Bader's virial partitioning analysis, procedures using the vibrational frequencies by utilizing local CC stretching force constants to derive an aromaticity index and many more.^[56]

In this work, a purely geometrical approach has been considered, which is the so called harmonic oscillator model of aromaticity (HOMA)^[57-60]. Compared to other geometrical procedures, in which the bond length of the molecule is compared to the mean bond length, in the HOMA model the concept of an optimal bond length is proposed as follows:

$$H = 1 - \frac{\alpha}{n} \sum (R_{opt} - R_i)^2, \quad (2.41)$$

where n is the number of bonds, R_i is the length of each individual bond and R_{opt} is the optimal bond length. The optimal bond length is the length of a bond in an ideal aromatic system and is calculated by minimizing the energy need for compressing a bond to the length of a double bond, and for expanding a bond to the length of a single bond. This energy is estimated by use of a harmonic potential. For a system of ideal aromaticity H should yield 1 and α represents a normalization constant, that is often chosen such that a system of alternating single and double bonds yields $H = 0$. While this definition is somewhat arbitrary, it is useful when comparing the aromaticity of different molecules.

Using the HOMA model, it is also possible to separate the physical effects into two terms as follows:

$$H = 1 - \alpha \left[(R_{opt} - R_{av})^2 + \frac{1}{n} \sum (R_{av} - R_i)^2 \right] \quad (2.42)$$

$$H = 1 - EN - GEO, \quad (2.43)$$

where R_{av} is the average bond length of the system. The first term, EN, is the elongation, which is a measure for the weakening and strengthening of the bonds, while the second term, GEO, describes the bond length alternation. These two terms describe the de-aromatization of a system with EN being the reduction of aromaticity by energetically destabilization of the system, without changes of its shape and GEO being the geometry-changing alternation, that break aromaticity.

It has to be noted, that all these geometric measures of aromaticity lose their usefulness, when the Badger rule is not fulfilled. The Badger rule connects the strength of a bond with its length, meaning that a shorter bond has to be the stronger bond.

In order to derive reliable results, an appropriate reference molecule has to be found from which this optimal bond length is taken. The acyclic polyene trans-1,3 butadiene has been proven to serve this purpose and the optimal bond length can easily be calculating by averaging over its single and double bond lengths^[56].

It should also be noted, that the reliability of the geometry is a key factor when looking at the aromaticity. Ab initio techniques, which are applied here, are dependent on the quality of the basis set and on the level of theory used.

2.4 Density of States

The density of states (DOS)^[61,62] is an important quantity, containing information about the electronic structure of a system. The DOS essentially describes the number of electron states, per unit energy and per unit volume, or in the case of a crystal per unit cell. In a crystal it is defined by

$$\rho(E) = \frac{1}{N_k} \sum_{n,\vec{k}} \delta(\epsilon_{n,\vec{k}} - E), \quad (2.44)$$

where $\epsilon_{n,\vec{k}}$ describes the energy of the band n , at the Brillouin zone point, given by the Bloch vector \vec{k} , and N_k is the number of k-points inside the Brillouin zone. The number of different electron states in the range E to $E + dE$, per unit cell is given by $\rho(E)dE$.

If the system is comprised of multiple parts, such as in the case of an organic/metal interface, the relative contribution of one of these parts to the total DOS can be calculated by projecting the eigenstates of this subsystem onto an orthonormal basis set. This is called the projected density of states (pDOS), or in the case of molecular orbitals it is called the molecular orbital projected density of states (MOPDOS). In the MOPDOS, the Kohn-Sham eigenstates of the full molecule/metal system $|\psi_{n,\vec{k}}\rangle$ are projected onto the Kohn-Sham eigenstates of the molecule $|\phi_i\rangle$. Using the orthonormality relation $\sum_i |\phi_i\rangle\langle\phi_i| = 1$ leads to

$$\rho_\phi(E) = \frac{1}{N_k} \sum_{n,\vec{k}} |\langle\phi_i|\psi_{n,\vec{k}}\rangle|^2 \delta(\epsilon_{n,\vec{k}} - E). \quad (2.45)$$

It should also be noted that for reasons of better presentation, the eigenvalues of the DOS and pDOS are broadened by a Gaussian function. The width of this Gaussian function is given by the Gaussian broadening σ .

2.5 Photoemission Intensity

Photoemission spectroscopy is a powerful technique to study the electronic structure of surfaces and interfaces. It is based on the photoelectric effect, first explained by Einstein 1905^[63]. In his work he describes the phenomena of electrons being emitted from a metal surface, after being exposed to electromagnetic radiation. Einstein used the concept of the photon, which was first conceptualized by Max Planck. The photon is light, in the form of a tiny packet of energy. The energy of the photon is proportional to the frequency of the corresponding electromagnetic wave. Then the kinetic energy of the electron which is emitted from the metallic surface is

$$E_{kin} = h\nu - \Phi - E_B , \quad (2.46)$$

where $h\nu$ describes the energy of the photon, with ν being the frequency of the electromagnetic wave and h being the proportionality constant, which has become known as the Planck constant. Φ is the work function, which is a surface specific constant, that describes the minimum energy required to remove an electron from the surface. E_B is the energy of the electrons initial state and is called the binding energy of the electron.

In typical photoemission spectroscopy measurements, such as the angle-resolved photoemission spectroscopy (ARPES)^[64,65], a monochromatic light source is used, with a defined energy, to excite electrons from an sample. The kinetic energy and the angle of emission of the emitted electron is then measured and can be characterized in regards to its polar angle θ and azimuthal angle ϕ . The momentum of the electron therefore is split into two components parallel to the substrate's surface

$$k_x = k \cdot \sin \theta \cos \phi \quad (2.47)$$

$$k_y = k \cdot \sin \theta \sin \phi, \quad (2.48)$$

where k is the wavenumber of the emitted electron. Because of the de-Broglie-relation $p = \hbar k$, the momentum and wavenumber of the electron are directly linked. Maps of the measured intensity $I(k_x, k_y)$, at constant binding energy, are called the photoemission momentum maps (k-maps).

A quantum mechanical description of the photoemission is given by the one-step model of photoemission^[66], which views the photoemission as a single coherent process, rather than multiple separated ones. In this thesis, the one-step model was used, following Ref. [66], to simulate theoretical k-maps.

When simulating k-maps, the photoemission intensity (or photoemission current) has to be calculated by evaluating the transition probability from initial state to final state. This can be achieved by applying Fermi's golden rule^[67]:

$$I(\theta, \phi; E_{kin}) \propto \sum_i |\langle \psi_f(\theta, \phi; E_{kin}) | \vec{A} \cdot \vec{p} | \psi_i \rangle|^2 \times \delta(E_{kin} + \Phi + E_B - h\nu) \quad (2.49)$$

Here \vec{A} is the vector potential from the photon's electromagnetic field, \vec{p} is the momentum operator of the photoelectron, ψ_i and ψ_f are the initial and final state of the photoelectron, respectively and the delta function expresses the energy conservation. Finding the appropriate treatment of the final state ψ_f represents the main problem when trying to evaluate Eq. 2.49.

A simple solution is to assume that the final state can be approximated by a plane wave $\psi_f \sim e^{i\vec{k}\vec{r}}$. This sets the photoemission intensity from a particular initial state $I_i(\theta, \phi)$ proportional to the Fourier transform of the initial state wave function $\tilde{\psi}_i(\vec{k})$ in the following way

$$|\tilde{\psi}_i(\vec{k})|^2 \propto \frac{I_i(\theta, \phi)}{|\vec{A} \cdot \vec{k}|^2}, \quad (2.50)$$

where $|\vec{A} \cdot \vec{k}|^2$ is a so-called polarization factor. For a number of organic, π -conjugated molecules, this has proven to lead to results in agreement to experimental data^[68-70].

However, when looking at organic/metal interfaces, the plane wave final state approximation tends to overestimates the photoemission signal from the substrate. This is because in photoemission experiments the limiting free mean path of the emitted electron only allows for the top most layers to be investigated. This is not accounted for in the plane wave final state approximation.

One way of dealing with the inelastic mean free path is to include a damping term into the final state^[71,72]. This is only included in close proximity to the substrate and therefore the plane wave final state approximation is split into two parts. The final state then looks as follows

$$\psi_{fd}(\vec{r}) = \begin{cases} e^{i\vec{k}\vec{r}} e^{\gamma(z-z_0)} & , z < z_0 \\ e^{i\vec{k}\vec{r}} & , z > z_0 \end{cases}. \quad (2.51)$$

Here, the mean free path length of the photoemitted electron is mimicked by the damping term $e^{\gamma(z-z_0)}$, where $\frac{1}{\gamma}$ is chosen such that it matches the mean free path. The range for when the damping term is included into the plane wave final state approximation is given by the point z_0 on the z-axis and is chosen to be in close proximity to the substrate.

2.6 Hückel Molecular Orbital Model

The Hückel molecular orbital model, or short Hückel model (HM)^[73-76], is a theory for determining the energies of π -electron orbitals in conjugated molecules and furthermore the charge density of a system. In this thesis, the simple Hückel model is used, and for the purpose of abbreviation, is referred to as the Hückel model. In its simple form, the HM can only be used with conjugated hydrocarbons and is the theoretical basis for the $4n + 2$ Hückel rule for π -electron systems (cf. Chapter 2.3).

The HM assumes that molecular orbitals can be written as a linear combination of atomic p_z -orbitals. For this purpose, the linear combination of atomic orbitals (LCAO) ansatz is used, in which the molecular orbitals ψ_i can be written as a linear combination of the atomic orbitals ϕ_r , as follows:

$$\psi_i = \sum_r c_{ri} \phi_r, \quad (2.52)$$

where c_{ri} is a coefficient determining the weight of each atomic orbital contribution. If the LCAO is then substituted into the Schrödinger equation (cf. Eq. 2.1), the following equation can be gained:

$$\sum_r c_{ri} \phi_r H = E \sum_r c_{ri} \phi_r. \quad (2.53)$$

The variational theorem then states that for a given eigenvalue problem with smallest eigenvalue $E^{(0)}$ and corresponding wave function $\psi^{(0)}$, any trial wave function ψ_i normalized by

$$\int \psi_i^* \psi_i dV = 1 \quad (2.54)$$

will satisfy

$$\varepsilon = \int \psi_i^* \hat{H} \psi_i dV \geq E^{(0)}. \quad (2.55)$$

Therefore, the ground state wave function and its energy can be obtained by substituting the ansatz into the expression for E which leads to

$$\sum_{j=1}^n c_j (H_{ij} - E S_{ij}) = 0, \quad (2.56)$$

with

$$H_{ij} = \int \phi_i^* \hat{H}_m \phi_j dV \quad (2.57)$$

$$S_{ij} = \int \phi_i^* \phi_j dV. \quad (2.58)$$

When $i \neq j$, the H_{ij} are called the hopping integrals and, while H_{ii} are the on-site integrals. S_{ij} is a matrix of the overlap integrals and $S_{ii} = 1$ (cf. Eq. 2.54). The corresponding $n \times n$ matrices $[H_{ij}]$ and $[S_{ij}]$ are the Hamiltonian and overlap matrices, respectively.

Eq. 2.56 has a solution only if $(H_{ij} - ES_{ij})$ is singular. Therefore E has to satisfy

$$\det([H_{ij} - ES_{ij}]) = 0. \quad (2.59)$$

This determinant is known as the secular equation. In the HM additional approximations are made. The overlap matrix is approximated to be the identity matrix $[S_{ij}] = I_n$. This assumes no overlap among distinct ϕ_i . For planar, unsaturated hydrocarbons the Hamiltonian matrix is parameterized as

$$H_{ij} = \begin{cases} \epsilon & i = j \\ t & i, j \text{ adjacent} \\ 0 & \text{otherwise.} \end{cases} \quad (2.60)$$

Here t is the previously mentioned hopping integral (cf. Eq. 2.57), or hopping parameter and ϵ is the on-site integral, or on-site parameter. The value of ϵ represents the energy of a $2p$ -electron, relative to an unbound electron, while t represents the energy of an electron localized in a $2p$ -electron orbital, compared to a delocalized π -electron orbital, formed by the $2p$ -electron orbitals of adjacent atoms.

2.7 Probe Particle Model

The probe particle model (PPM)^[78-81] is a model designed to simulate high-resolution scanning probe imaging techniques, such as high-resolution scanning tunneling microscopy (HR-STM), inelastic tunneling microscopy (IETS-STM) and non-contact atomic force microscopy (nc-AFM). These techniques all rely on the interaction of a probe tip, which ideally consists of a single atom, with the sample. While in the nc-AFM measurement the forces acting upon the probe tip are measured, by vibrational modes, both STM and IETS are based on the quantum mechanical tunneling effect. The IETS-STM, however, uses inelastic tunneling in order to change the vibrational state of the sample, which is then measured. Carbon monoxide (CO) is often used as a probe particle, with the oxygen atom representing the tip atom, while the carbon atom is fixed to the tip apex. This configuration has many advantages, such as its flexibility and reproducibility.

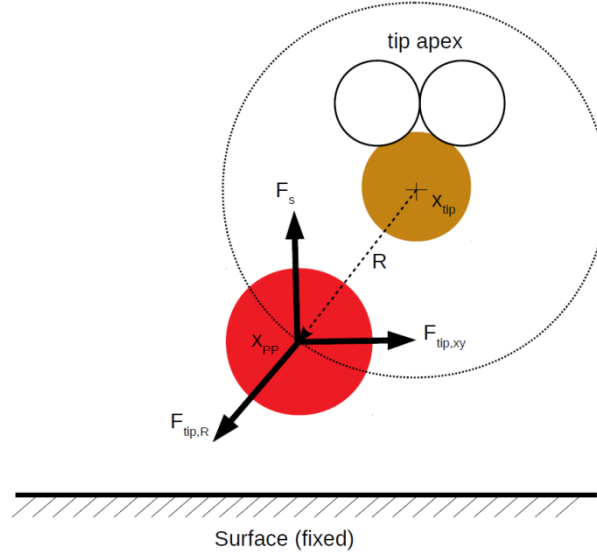


Fig. 2.4 The forces acting on the probe particle (red circle): F_s is the force from the fixed surface, $F_{tip,R}$ is the force from the tip apex and $F_{tip,xy}$ is the lateral force.

In the PPM, the forces in the tip/surface interaction (cf. Fig. 2.4) are approximated by using classical force fields, while the system to be measured is treated as fixed in time. The Leonard-Jones force field is used to approximate the Pauli repulsion, which dominates the interaction at short-range, as well as the vdW attraction which dominates the long-range interaction. The Lennard-Jones force field is calculated with following equation:

$$\vec{F}_{LJ}(\vec{R}) = \vec{R} \left(\frac{C_{12}}{|\vec{R}|^{14}} - \frac{C_6}{|\vec{R}|^8} \right). \quad (2.61)$$

Here the first term $\frac{C_{12}}{|\vec{R}|^{14}}$ represents the short-ranged Pauli repulsion, while the second term $\frac{C_6}{|\vec{R}|^8}$ represents the vdW attraction. Furthermore, the electro-static force field also has to be taken into account. The electro-static forces are approximated by a multipole approach using monopoles, dipoles and quadrupoles, which can be expressed with following equation:

$$\vec{F}_{el}(\vec{R}) = \frac{\partial}{\partial \vec{R}} \int \rho_{probe}(\vec{r}) V_{surf}^H(\vec{r} - \vec{R}) d\vec{r}, \quad (2.62)$$

where V_{surf}^H is the electrostatic surface Hartree potential and ρ_{probe} is the charge density of the probe particle.

Since nc-AFM and IETS-STM are methods using vibrational modes, the spring force acting upon the probe particle also has to be modelled, as follows:

$$F(\Delta x) = -k_x \Delta x, \quad (2.63)$$

where k_x is the stiffness of the probe particle. The PPM achieves results that are in good agreement to what experimental measurements of nc-AFM, IETS-STM and high resolution STM have shown.

The PPM Python code used in this thesis was provided by Ref. [82].

3 Results

In this section the calculation results and comparisons to experimental data are given. Chapter 3.1 is dedicated to the aromaticity and electronic structure of kekulene (cf. Fig. 3.1). Calculations of kekulene were compared to experimental results of kekulene on Cu(111). In Chapter 3.2, the kekulene/Cu(110) system was analyzed in more detail.

For both chapters a motivation is given at the beginning, followed by an investigation of adsorption of kekulene on the respective substrate. Then a look into the aromatic and electronic structure is given in each chapter after which a conclusion is given at the end.

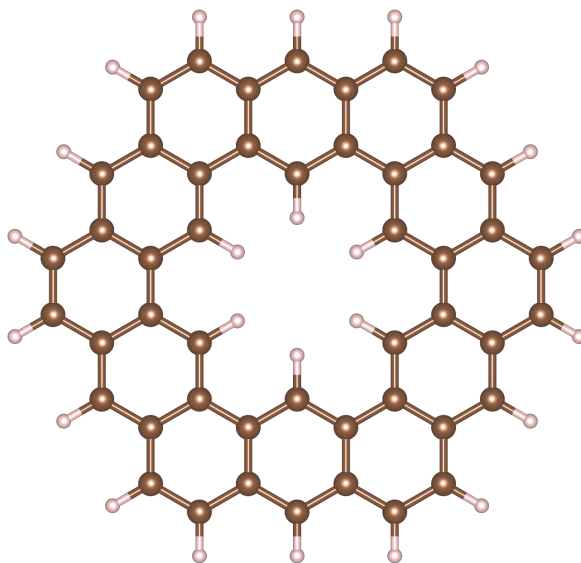


Fig. 3.1 The polycyclic hydrocarbon kekulene ($C_{48}H_{24}$)

3.1 Kekulene/Cu(111)

3.1.1 Motivation

In order to study the aromatic and electronic structure of the kekulene molecule, an appropriate substrate for synthesis has to be found. Copper has been known to be such a substrate, especially its most stable facet Cu(111). Relatively low interaction strengths are observed between the Cu atoms and the adsorbent, which guarantee that the geometric and electronic structure of the adsorbent is not altered to a too large degree. In addition, the 3-fold symmetric nature of Cu(111) fits nicely with the 3-fold symmetric nature of kekulene. For these reasons, Cu(111) has been used as a substrate for synthesis of kekulene in previous works^[4].

Here, DFT calculations of free kekulene as well as kekulene on Cu(111) are compared to experimental results of kekulene on Cu(111). These experimental results, the synthesis of kekulene on Cu(111) as well as comparisons to theoretical calculations, which also can be found in this thesis, are documented in detail in Ref. [10].

Previous studies of kekulene's aromaticity^[4] have already provided insights into the kekulene system and concluded, that the Clar sextet model (cf. Chapter 2.4) most likely provides an accurate depiction of the aromaticity of kekulene. The goal of Ref. [10] has been to give further insights into the aromaticity, geometric and electronic structure of kekulene and providing a new way of kekulene's synthesis. Kekulene's ideal adsorption geometry (adsorption position, height and energy) have been calculated, the electronic structure of kekulene's frontier orbitals have been analyzed and comparisons between various theoretical configurations of kekulene and the experimental results of the kekulene/Cu(111) system have been made. These theoretical configurations include geometric models of kekulene, in which the bond lengths have been varied, Hückel molecular orbital models of kekulene, in which the inter-ring electron coupling has been varied as well as DFT optimized configurations of free kekulene and kekulene on Cu(111). These models have been made for comparing kekulene's aromatic behaviors to those of the theoretical AWA model of aromaticity and the Clar sextet model. Both of these models have been postulated in the past to predict the aromatic structure of the kekulene molecule^[83-86]. This analysis of the electronic structure includes calculations of the DOS and the MOPDOS (cf. Chapter 2.4), experimental measurements and simulations of the photoemission intensity (cf. Chapter 2.5) and an investigation of the charge density distribution and nodal structure of kekulene's frontier orbitals.

In this thesis, compared to Ref. [10], further investigations into the kekulene molecule are provided, including its optimal adsorption position and its aromatic and electronic structure. In addition, comparisons to the aromaticity of related structures such as coronene (C₂₄H₁₂), super kekulene (C₇₂H₃₆) and the three annulene circuits, [18]-annulene, [30]-annulene and [42]-annulene are made.

3.1.2 Geometric Optimization

The first step in optimizing the geometry of kekulene/Cu(111) consists of choosing an appropriate lattice parameter a for setting up the structural model of the Cu surface. Initial relaxations used the lattice parameter of bulk Cu optimized with PBE-GGA (cf. Chapter 2.1.3) in combination with the TS-vdW correction method (cf. Chapter 2.1.4), which results into $a = 3.55 \text{ \AA}$. In later relaxations the experimentally measured lattice parameter of copper, $a = 3.61 \text{ \AA}$ ^[87] has been used.

Three Cu layers in a repeated slab approach are taken into account, adding enough vacuum layers in order to ensure proper spacing in between each periodic replica. In the middle of the vacuum region a dipole layer, calculated self-consistently, has been added to account for the asymmetric slab and the resulting artificial electric field. The generalized gradient approximation (GGA) (cf. Chapter 2.1.3) is used as treatment of the exchange-correlation effects. Van der Waals corrections, according to Tkatchenko and Scheffler (TS), as explained in Chapter 2.1.4, have been included. The following four principal adsorption positions on Cu(111) have been used as a starting point of the relaxations: the top, bridge, hollow fcc and hollow hcp position (cf. Chapter 2.2.2). The kekulene/Cu(111) system with kekulene in the hcp position can be seen in Fig. 3.2 (a).

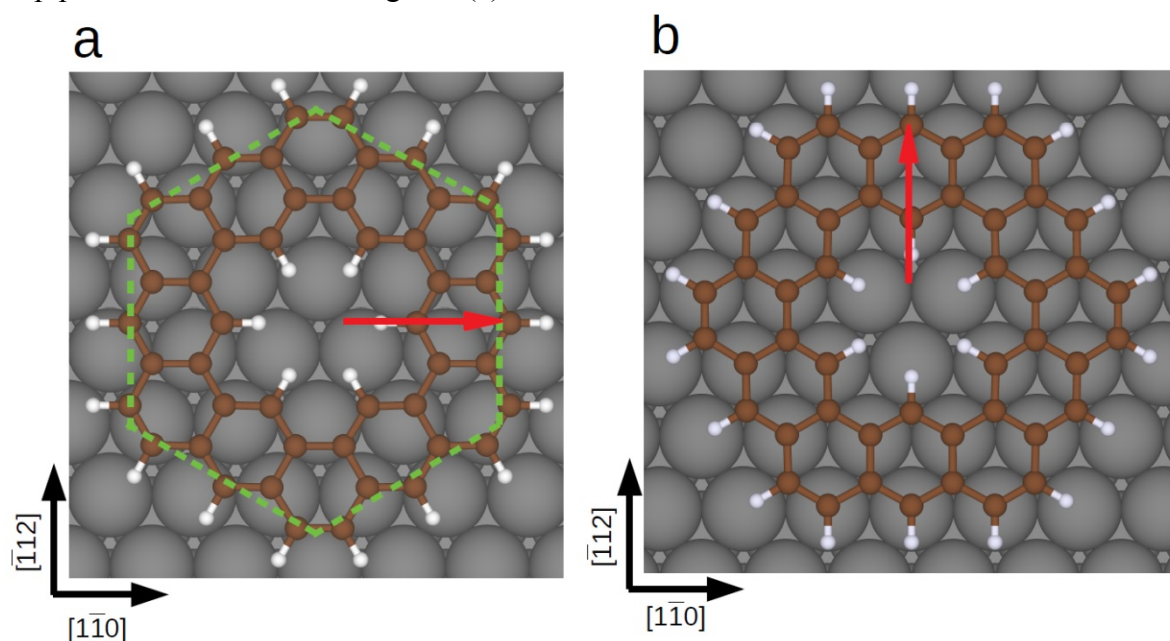


Fig. 3.2 Structural model of kekulene/Cu(111) for the two principal azimuthal orientations. (a) shows kekulene's apothem (red arrow) oriented parallel to the $[1 -1 0]$ direction of the Cu(111) substrate, which shall be denoted as "orientation 1", while (b) shows kekulene's apothem oriented parallel to the $[-1 1 2]$ direction of the Cu(111) substrate, which shall be denoted as "orientation 2". The green dashed lines in (a) depict the hexagonal sides of kekulene. In addition, (a) shows kekulene in the hollow hcp adsorption position, while (b) shows kekulene the hollow fcc adsorption position of the Cu(111) substrate.

Because kekulene belongs to the D_{6h} symmetry group and therefore possesses a six-fold symmetry when rotated around the z-axis, two azimuthal orientations separated by 30 degrees have been considered, which are denoted as orientation 1 and orientation 2 in Tab. 1. The orientation can be expressed with respect to kekulene's apothem (in a hexagon the apothem

(which is illustrated by the red arrow in Fig. 3.2 (a)) is the line segment from the center to the midpoint of one of its sides (green dashed lines in Fig. 3.2 (a)). Here orientation 1 represents the position when kekulene's apothem is parallel to the $[1 -1 0]$ direction of the Cu(111) substrate and orientation 2 represents the orientation when kekulene's apothem is parallel to the $[-1 1 2]$ direction of the substrate and can be seen in Fig. 3.2 (a). This leads to a total of eight different configurations to be analyzed. For each a 7×7 supercell has been used in order to have a horizontal separation between the kekulene molecules of at least 4 \AA , which should be sufficient to reduce intermolecular interactions, while at the same time keeping the computational costs at a reasonable expense. A thickness of 3 Cu layers has been chosen for each configuration and all degrees of freedom, including the Cu(111) substrate, have been relaxed.

The adsorption energy of the kekulene on Cu(111) have been calculated as laid out in Eq. 2.40 (cf. Chapter 2.2.2). The adsorption height was calculated by taking the average height of kekulene's carbon atoms and subtracting it to the average height of the top layer of the Cu(111) substrate. The resulting adsorption heights and adsorption energy for the above mentioned setups are compiled in Tab. 3.1.

Tab. 3.1: Average carbon height h_c [\AA] and adsorption energy E_{ad} [eV] of kekulene on Cu(111) obtained for the four different adsorption positions and two different azimuthal orientations.

Adsorption position	Orientation	h_c [\AA]	E_{ad} [eV]
top	1	3.143	-5.993
bridge	1	3.148	-6.047
hollow fcc	1	3.143	-6.038
hollow hcp	1	3.154	-6.047
top	2	3.278	-5.862
bridge	2	3.114	-6.173
hollow fcc	2	3.108	-6.186
hollow hcp	2	3.057	-6.201

The results indicate that the energetically most favorable adsorption configuration of kekulene on Cu(111) is the hollow hcp position and the orientation of molecule with its apothem parallel to the $[-1 1 2]$ direction of Cu(111). In Ref. [10] it can also be seen that these results were compared to calculations from a different team using localized basis set instead of VASP's plane wave basis set. Both calculations yielded the same configuration as the energetically most favorable.

In order to test the sensitivity of the adsorption height and adsorption energy on the computational setup, additional calculations with a slightly altered setup have been done. Note that these additional tests have only been performed with kekulene in the hollow hcp position of the Cu(111) substrate. The additional calculations used the experimentally measured lattice parameter of Cu, $a = 3.61 \text{ \AA}$ and fixed positions of the copper atoms, taking into account 6 Cu layers. Other than these changes, the setup was the same as the one mentioned above. These calculations yielded a slightly reduced adsorption energy of -5.925 eV while the adsorption height stayed roughly the same at 3.05 \AA .

3.1.3 Analysis of Aromaticity

In order to describe kekulene's aromaticity (i.e. its bonds), we apply the HOMA concept introduced in Chapter 2.3. To this end, the bond lengths of the system are analyzed and the H value of four different sub-segments are compared for different systems. Here a comparison between a free kekulene molecule, kekulene/Cu(111) and two idealized models, namely the "Clar" and the so called "annulene-within-an-annulene" (AWA) model of kekulene is made. These two models represent the two opposing ends of the spectrum of aromaticity in which kekulene is believed to lie in between^[4]. These two models have been constructed using the bond labels which can be seen in Fig. 3.3. Since the length of all sides of the hexagonally shaped benzoic compounds of kekulene are fixed, the inter-bond angles have to be adjusted and will deviate from the six-fold symmetry benzene angles usually show. Here only the angle denoted as β , inside sextet 1 has been used specifically to adjust the bond length e .

The Clar model depicts the kekulene system in a situation where Clars sextet rule is fulfilled (cf. chapter 2.3). For this model six disjoint benzoic sextet (denoted with 2 in Fig. 3.3) are supposed to have ideal aromaticity ($H_2 = 1$) by setting $R_a = R_c = R_d = R_{opt}$. All other bonds lengths are set to be in the single bond range except the e bond which is set to a value typical for a double bond.

The AWA model, in the other extreme, describes the kekulene system as two annulene circuits, the inner [18]-annulene and the outer [30]-annulene ring, which are connected to each other by single bonds. To fulfill the ideal aromaticity of the two annulene rings, the choice $R_a = R_b = R_d = R_e = R_f = R_{opt}$ has been made to ensure $H_{[18]} = 1$ and $H_{[30]} = 1$. To have a detailed comparison of the HOMA between those four systems, the H values of the inner circuit ($H_{[18]}$), the outer circuit ($H_{[30]}$) and the two benzoic rings denoted as 1 and 2 in Fig.3.3 (H_1 and H_2) have been calculated (cf. Fig. 3.4 (c) and (d)).

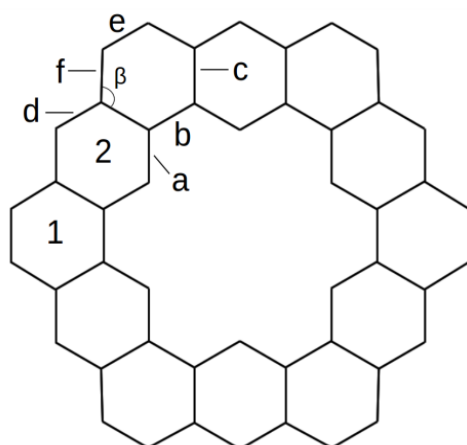


Fig. 3.3 Labelling of the bonds of the kekulene molecule, the angle β and the benzoic rings 1 and 2.

The optimal C-C bond length R_{opt} has been calculated by averaging the C-C single and double bond lengths of the reference molecule trans-1,3 butadiene (cf. Appendix). This results in the optimal bond length being $R_{opt} = 1.403 \text{ \AA}$. The single (longest) and double (shortest)

bond length of the reference molecule is taken in order model the Clar and AWA model, which are $R_{single} = 1.456 \text{ \AA}$ and $R_{double} = 1.350 \text{ \AA}$. The empirical normalization parameter α is set to $\alpha = 282.94 \text{ \AA}^{-2}$ which has been taken from Ref. [62]. The bond lengths and the resulting HOMA value of the four systems in question can be seen in Tab. 3.2.

Tab.3.2 Bond lengths [\AA] and H values, including EN and GEO values for DFT-optimized free kekulene and kekulene/Cu(111) as well as the AWA and Clar models of kekulene.

	AWA model	free kekulene	kekulene/Cu(111)	Clar model
<i>a</i>	1.403	1.400	1.397	1.403
<i>b</i>	1.403	1.461	1.452	1.456
<i>c</i>	1.456	1.438	1.431	1.403
<i>d</i>	1.403	1.411	1.407	1.403
<i>e</i>	1.403	1.373	1.370	1.350
<i>f</i>	1.403	1.444	1.437	1.456
H_1	0.735	0.527	0.651	0.472
H_2	0.735	0.878	0.923	1.000
$H_{[18]}$	1.000	0.678	0.767	0.735
$H_{[30]}$	1.000	0.756	0.802	0.526
EN_1	0.088	0.252	0.155	0.089
EN_2	0.088	0.051	0.022	0
$EN_{[18]}$	0	0.087	0.045	0.088
$EN_{[30]}$	0	0.052	0.035	0.032
GEO_1	0.177	0.221	0.195	0.439
GEO_2	0.177	0.07	0.05	0
$GEO_{[18]}$	0	0.235	0.189	0.177
$GEO_{[30]}$	0	0.193	0.163	0.442

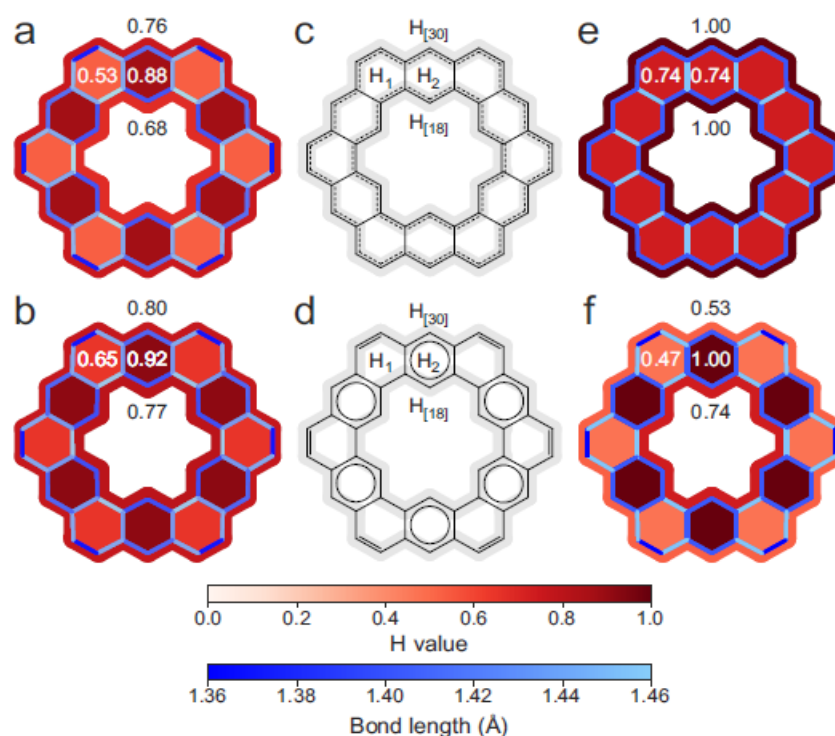


Fig. 3.4 HOMA comparison between (a) DFT optimized kekulene in the gas phase (b) DFT optimized kekulene on Cu(111) (e) kekulene in the AWA model and (f) kekulene in the Clar model. (c) and (d) are a chemical drawings of the AWA and Clar model of kekulene's aromaticity, respectively.

Many of the bond labels of the DFT optimized systems show values closer to the Clar model. Especially the bond b , which the Clar model presumes to be a single bond, is computed to be in the range of being considered a single bond in the DFT optimized system. In the case of free kekulene, it is even longer than the single bond of the reference molecule trans-1,3 butadiene. Other values such as a , being the presumed double bond (of the Clar model), deviate from the aromatic length the AWA model postulates, however, the bond is not as short (strong) as the Clar model predicts.

Moreover, the H values demonstrate that the more favorable model for the DFT optimized system is the Clar model. Especially the $H_{[18]}$ value from the inner circuit shows a strong deviation from being annulene as predicted by the AWA model, most likely due to the previously mentioned b bond being in the range of a single bond instead of being aromatic.

What can also be seen is that in general the adsorption onto the Cu(111) substrate causes the bond lengths and H value to be modified towards the AWA model and away from the Clar model, however this seems to be only in a miniscule amount and does not suggest a large change of the aromaticity of the system.

The EN and GEO values, describing the de-aromaticity, however, present a more balanced picture, with some values of the DFT optimized systems being closer to the AWA models while others are closer to the Clar model. It should be noted that many of the values are not in between the values of the Clar and AWA models. Since these two models should represent the two opposing extremes, it is difficult to recognize a trend towards a certain model if some of the value deviate very much from the scale. Such a behavior could actually be foreseen by considering the length of the bond label a . Even though the Clar and AWA model both predict a to be the length of an aromatic bond (1.403 Å), the geometrically optimized values deviated from this value a little bit with $a_{free} = 1.400$ Å and $a_{kekulene/Cu(111)} = 1.397$ Å. Small changes of course are expected due to approximations in the DFT optimization as well as because the reference molecule not being absolutely perfect for comparison. When looking at a similar occurrence in the EN_1 value, it can be seen that both the Clar and the AWA model predict that EN_1 is roughly 0.088. The DFT optimized values, however, differ to a much higher margin (with $EN_{free} = 0.255$ and $EN_{kekulene/Cu(111)} = 0.155$) compared to the case of the bond lengths. With such a large margin of error in the values of de-aromatization, it is questionable if these values can be used in this case to see a trend of the system towards either the Clar or the AWA model. Because of this, the EN and GEO values have been excluded in further analysis of the aromaticity of the kekulene system.

In addition to the limiting cases of Clar and AWA models, the H values of intermediate model structures have been calculated. To this end, C-C bonds are monotonously adjusted using a structural parameter S constructed such that for Clar model $S = 1$, while for AWA model $S = 0$. The pathway of structure adjustment is given by

$$b(S) = b_{\text{Clar}} - (1 - S)^{\gamma_b}(b_{\text{Clar}} - b_{\text{AWA}}) \quad (3.1)$$

$$c(S) = c_{\text{AWA}} - S^{\gamma_c}(c_{\text{AWA}} - c_{\text{Clar}}) \quad (3.2)$$

$$\beta(S) = \beta_{\text{Clar}} - (1 - S)^{\gamma_\beta}(\beta_{\text{Clar}} - \beta_{\text{AWA}}) \quad (3.3)$$

$$f(S) = f_{\text{Clar}} - (1 - S)^{\gamma_f}(f_{\text{Clar}} - f_{\text{AWA}}) \quad (3.4)$$

while bonds a and d are kept fixed, since they both have the same value for the Clar and AWA model. Here, bonds with indices Clar and AWA correspond to Clar and AWA models, respectively, and are taken from Tab.1. In three different calculations, the exponents γ are chosen equal 1,2 and 3 (cf. below).

The above equations include the exponents $\gamma_b, \gamma_c, \gamma_\beta, \gamma_f$, by which the connection between Clar and AWA models can be adjusted. With the aim to search for a pathway containing structures with $H_1, H_2, H_{[18]}$ and $H_{[30]}$ values as close as possible to those of DFT-optimized free kekulene and kekulene/Cu(111) (cf. Tab. 3.2), three different sets were tested: (A) $\gamma_b = \gamma_c = \gamma_\beta = \gamma_f = 1$, (B) $\gamma_b = \gamma_c = \gamma_\beta = \gamma_f = 2$, and (C) $\gamma_b = \gamma_\beta = \gamma_f = 1, \gamma_c = 3$.

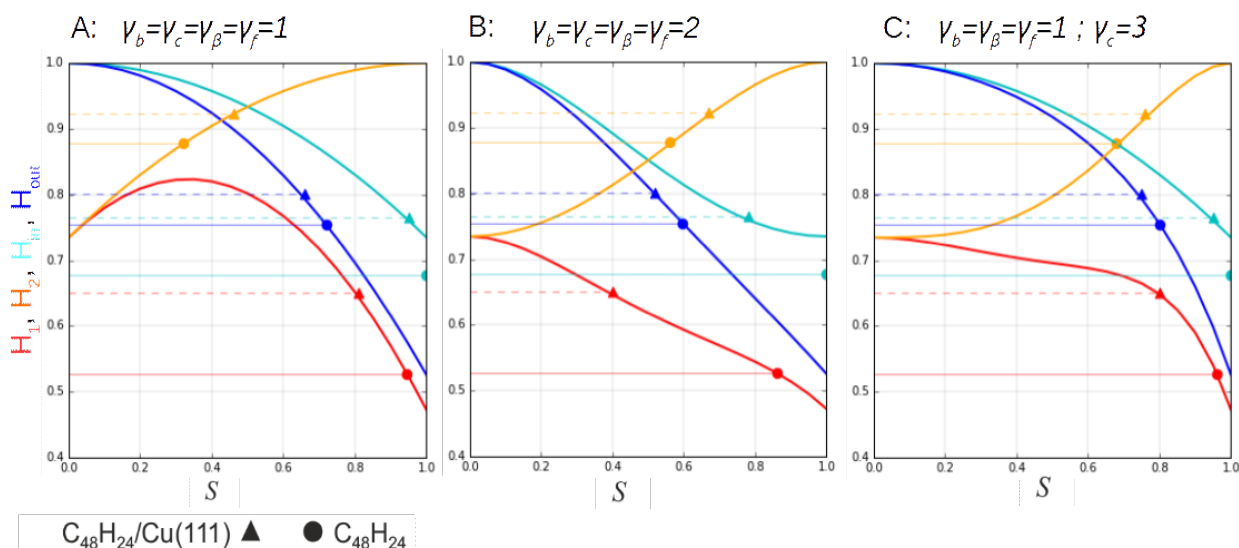


Fig. 3.5 Comparison of the H values for the DFT-optimized free kekulene (solid horizontal lines) and kekulene/Cu(111) (dashed horizontal lines) with H values calculated for interpolation structures defined for three different sets of γ (solid curves). Colors: H_1 – red, H_2 – orange, $H_{[18]}$ – light-blue, $H_{[30]}$ – blue. The solid circles and triangles mark the cross-section of horizontal lines and curves corresponding to same type of H values for DFT-optimized free kekulene (solid circles) and kekulene/Cu(111) (triangles). Least scatter of circles and triangles in (c) allows to use averaged value of corresponding S to draw conclusion about aromaticity of DFT-optimized free kekulene and kekulene/Cu(111).

It turns out that the choice $\gamma_b = \gamma_\beta = \gamma_f = 1, \gamma_c = 3$, leads to the smallest scatter of the intermediate structures (S values) corresponding to H values of DFT-optimized free kekulene and kekulene/Cu(111) (cf. Fig. 3.5). This allows reasonable averaging of S -values and finding a conclusion, whether DFT-optimized free and adsorbed kekulene's are closer to Clar or AWA models.

We have compared the results of $H_1, H_2, H_{[18]}$ and $H_{[30]}$ in Tab. 3.3, to the results of the intermediate structures and inscribed each HOMA value to an equivalent intermediate

structure via their S value (S_{eq}) and the scattering of S_{eq} . The average S_{eq} for each structure has been calculated by combining the S_{eq} results for H_1 , H_2 , $H_{[18]}$ and $H_{[30]}$ for a given structure. The scattering of S_{eq} is the biggest difference between the average and a single S_{eq} result.

Tab. 3.3 Comparison of average S_{eq} and scattering of S_{eq} (for the free kekulene and kekulene/Cu(111) system) between the three choices of intermediate pathways A, B and C.

	Structure	average S_{eq}	Scattering of S_{eq}
A: all $\gamma = 1$	free kekulene	0.7465	0.4263
	kekulene/Cu(111)	0.72	0.23
B: all $\gamma = 2$	free kekulene	0.7538	0.2463
	kekulene/Cu(111)	0.5925	0.1925
C: $\gamma_c = 3$ $\gamma_b = \gamma_\beta = \gamma_f = 1$	free kekulene	0.86	0.18
	kekulene/Cu(111)	0.815	0.135

In Tab. 3.3 it can be seen that by increasing γ and therefore the order of the interpolation, a reduction of the scattering of S_{eq} for free kekulene, as well as the kekulene/Cu(111) structure can be achieved. In order to describe each structure by a single S_{eq} , it is preferable to reduce scattering of the different S_{eq} for each HOMA value. Comparing panel A with panel C, it can also be seen that the average S_{eq} values increased for C in both structural cases, meaning that panel C would suggest a structure closer to the Clar model. In the panel B the free kekulene structure remains close to the results of panel A, however, the kekulene/Cu(111) results have moved closer to the center between the Clar and AWA structure. It should also be kept in mind that increasing γ , the order of interpolation, creates a bias towards either side and should therefore also be reduced. Comparing panel B and C shows that by selectively increasing specific γ values, the scattering can be further reduced, even when keeping the other γ values at 1. This would mean that the structural interpolations from panel C is kept closer to panel A, with less bias, but at the same time leading to better results than panel B.

Here panel C has been chosen to fit best for assigning a unique S value to the relaxed gas phase and adsorbed structures of kekulene, respectively, but since the choice of exponent influences the results so heavily, it should be kept in mind that the conclusion given is only of qualitative character.

When analyzing bond lengths and HOMA values of kekulene, it might also be of interest to compare these with the bond lengths and HOMA values of similar polycyclic aromatic hydrocarbons such as coronene ($C_{24}H_{12}$) and super-kekulene ($C_{72}H_{36}$), as well as annulene structures of similar size as the ones found in kekulene. For this purpose DFT optimizations of these structures were done using B3LYP hybrid functionals (cf. Chapter 2.1.3). These were compared to the kekulene structure also optimized using the same hybrid functionals. This structure differs from the previous calculated kekulene structure, using PBE, only by a small margin, as can be seen when comparing Fig. 3.6 with Tab. 3.3, but it should also be noted that the reference molecule trans-1,3 butadiene has also been calculated again using hybrid functionals (cf. Appendix A) which lead to a new $R_{opt} = 1.399\text{\AA}$. The empirical normalization parameter α was kept at $\alpha = 282.94 \text{\AA}^{-2}$.

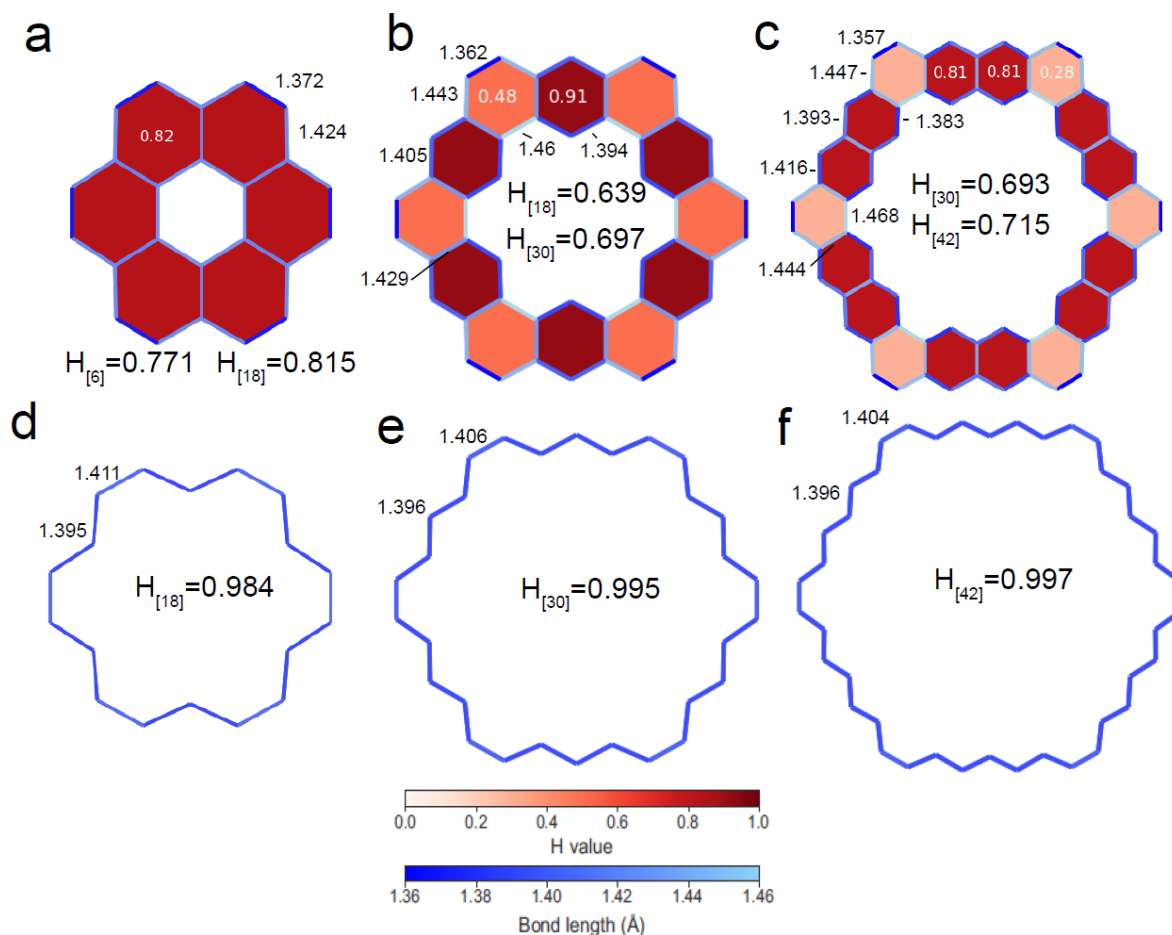


Fig. 3.6 Comparison of bond lengths and aromaticity between (a) coronene ($C_{24}H_{12}$) (b) kekulene ($C_{48}H_{24}$) (c) super kekulene ($C_{72}H_{36}$) (d) [18]-annulene (e) [30]-annulene and (f) [42]-annulene. All structures were calculated in the gas phase. The numbers next to the bonds represent their respected bond lengths in [Å]. In the case of the annulene circuits (d,e,f) one number is given which represents all the bond lengths in between the corners.

What can be seen when comparing the three similar hydrocarbons, coronene ($C_{24}H_{12}$), kekulene ($C_{48}H_{24}$) and super kekulene ($C_{72}H_{36}$) is, that the bond lengths and therefore the resulting HOMA values appear to all form a six-fold symmetrical structures, making all three structures part of the symmetry group D_{6h} . This, however, is only accounting to the carbons. When the hydrogen atoms are also included the small alternating out of plane bending of the inner hydrogens makes these structures D_{3d} . It also appears like super kekulene ($C_{72}H_{36}$) does not seem to follow Clar's sextet rule, since the aromatic sextets are not disjoint anymore. When comparing the annulene rings to the polycyclic structure, it can be observed that the annulene rings show a more aromatic behavior (which would also be expected of kekulene in the AWA model), the polycyclic structure, however, have a reduced aromaticity in their inner and outer circuits. In the case of the outermost bond (cf. bond *e* in Fig. 3.3), which is also the shortest (double bond) for the polycyclic structure, it seems that the larger the structure the more compressed this bond becomes (with $e_{\text{coronene}}=1.372$ Å, $e_{\text{kekulene}}=1.362$ Å and $e_{\text{super-kekulene}}=1.357$ Å). The longest (single) bond (cf. bond *b* in Fig. 3.3) also seems to become more extreme the larger the structure becomes (with $b_{\text{coronene}}=1.424$ Å, $b_{\text{kekulene}}=1.46$ Å and $b_{\text{super-kekulene}}=1.468$ Å).

3.1.4 Hückel Model

As described in Chapter 2.6, the Hückel model can be used to simulate the electronic coupling of the C-C bonds in kekulene in a variety of ways. Here, the Hückel model was used to compare theoretical models of kekulene with varying interconnection strength between its inner and outer annulene circuits ([18]-annulene and [30]-annulene, respectively) among each other and to other previously mentioned models. No interaction between the inner and outer ring of kekulene would resemble the electronic structure, which the previously mentioned AWA model would propose, while a stronger interaction between the rings would be closer to what the Clar model suggests.

First the Hückel matrix has to be constructed, which is a 48×48 Matrix, since each carbon atom of kekulene contributes one p_z orbital. A cut-out of this 48×48 Hückel Matrix which contains the information of the interaction among all the carbon atoms of kekulene can be seen in Fig. 3.7 including the labeling of the 11 carbon atoms shown in the matrix. The bonds follow the same labeling as before (cf. Fig. 3.3).

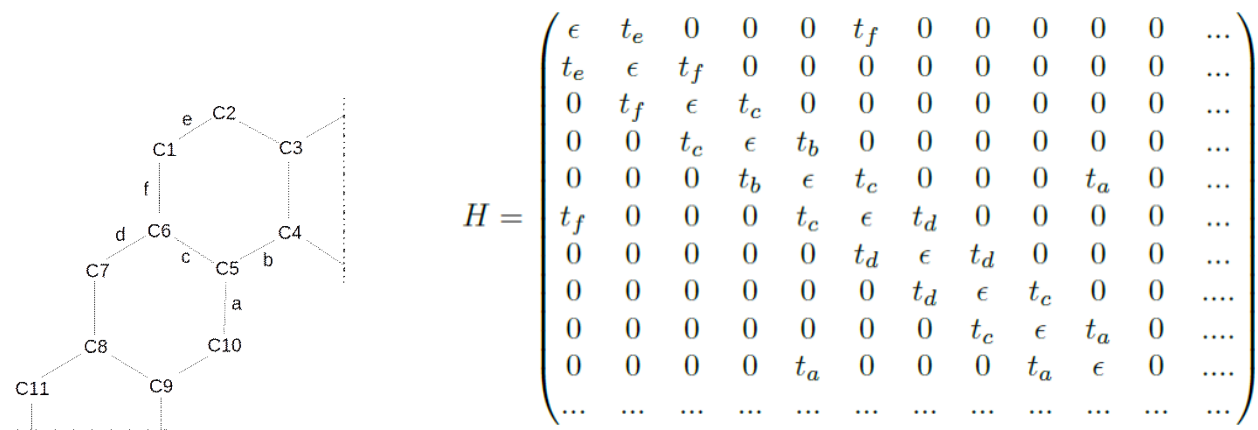


Fig. 3.7 Labelling of atoms and bonds in kekulene molecule for the Hückel model and the corresponding H matrix. The letters a-f denote the bonds of adjacent carbon atoms. The numbers 1-11 enumerate the single carbon atoms of kekulene.

The hopping parameter t_c of the bond connecting the inner and outer annulene circuits has been varied between $t_c = 0$ eV (no coupling between circuits) to $t_c = -3.5$ eV (typical coupling between C atoms in graphene). All other hopping parameter (t_a , t_b , t_d , t_e and t_f) are kept constant at $t = -4.1$ eV and the values of ϵ are set to $\epsilon = -3.35$ eV. With this choice of parameters, orbital energies in good agreement with DFT results, are obtained.

3.1.5 Density of States

It is interesting to analyze how the adsorption onto Cu(111) affects kekulene's orbital structure. To this end, a comparison between the DOS of free kekulene and kekulene/Cu(111) is made. Gasphase calculations for kekulene in D_{6h} symmetry have been performed using the *ab initio* quantum chemistry software package NWChem^[88], using a 6-31G* basis set. The exchange-correlation effects are approximated using the PBE-GGA approach in order to have good comparison to the aforementioned kekulene/Cu(111) system. The energy and number of electrons of the orbitals are given in Tab. 3.4.

Tab. 3.4 Orbital energies of the molecular orbitals of free kekulene relative to the vacuum energy (E_{vac}). Each orbital is also labeled with the number of electrons it holds.

Orbital symmetry	$E-E_{vac}$ [eV]	electrons	Label
e_{1g}	-2.279	0	LUMO+3
e_{1g}	-2.279	0	LUMO+2
e_{2u}	-2.363	0	LUMO+1
e_{2u}	-2.363	0	LUMO
e_{1g}	-4.819	2 e	HOMO
e_{1g}	-4.819	2 e	HOMO-1
e_{2u}	-4.943	2 e	HOMO-2
e_{2u}	-4.943	2 e	HOMO-3
a_{2u}	-5.466	2 e	HOMO-4
b_{2g}	-5.789	2 e	HOMO-5
a_{1u}	-5.972	2 e	HOMO-6
b_{1g}	-6.181	2 e	HOMO-7

When looking at free kekulene with undisturbed D_{6h} symmetry, it can be seen that several orbitals are doubly degenerate. Especially the highest occupied molecular orbital (HOMO) which belongs to the irreducible representation e_{1g} , as well as the lowest unoccupied molecular orbital (LUMO), belonging to the irreducible representation e_{2u} . The two orbitals below the HOMO/HOMO-1 are also doubly degenerate, also known as HOMO-2/HOMO-3. HOMO-4 and HOMO-5, belonging to a_{2u} and b_{2g} , respectively, are not degenerate, as well as the following HOMO-6 and HOMO-7.

For the calculation of the kekulene/Cu(111) system, the energetically most optimal configuration calculated in Chapter 3.1.2 was used, with an increased number of substrate layers to 6 Cu(111) layers. In Fig. 3.8 the total density of states of the kekulene/Cu(111) system is given. Also the density of states projected onto the Cu(111) substrate as well as the kekulene molecule is given. It can be seen that the HOMO of kekulene (filled primarily with electrons in the p_z -state) is located roughly 1.5 eV below the fermi level, which is at the onset of the Cu-d states.

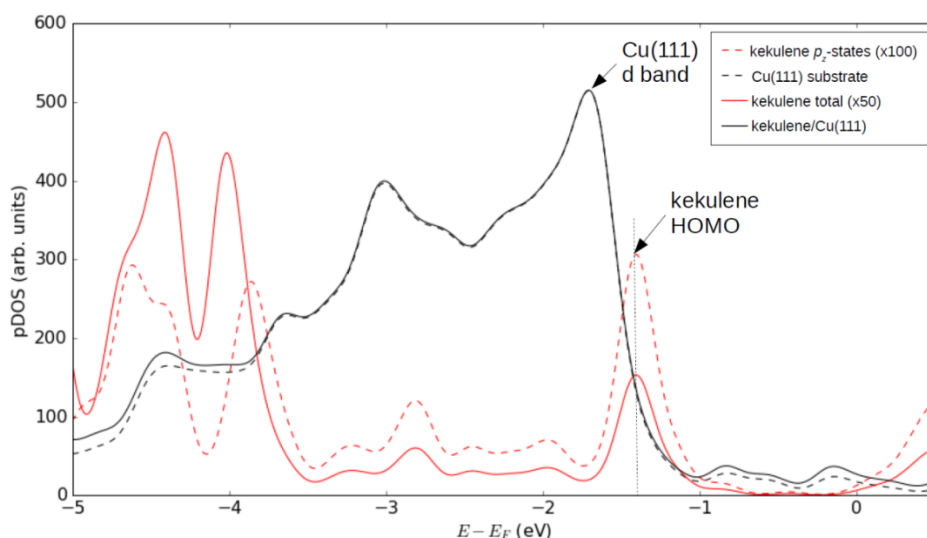


Fig. 3.8 DFT calculated density of state (DOS) of the kekulene/Cu(111) system and the projected density of states (pDOS) of the kekulene molecule, as well as the Cu(111) substrate..

A graphical representation of Tab. 3.4 together with a comparison to the kekulene/Cu(111) system can be seen in Fig. 3.9, where the DOS (cf. Chapter 2.4) of free kekulene as well as kekulene/Cu(111) are depicted. When kekulene is adsorbed onto a Cu(111) substrate a slight lifting of the degeneracy of each molecular orbital can be seen. Both the DOS and the MOPDOS are here in relation to the Fermi-level, which means every orbital beneath the Fermi-level (at 0 eV) is expected to be occupied. Since for both cases the LUMO is above the Fermi-level, no charge transfer is expected.

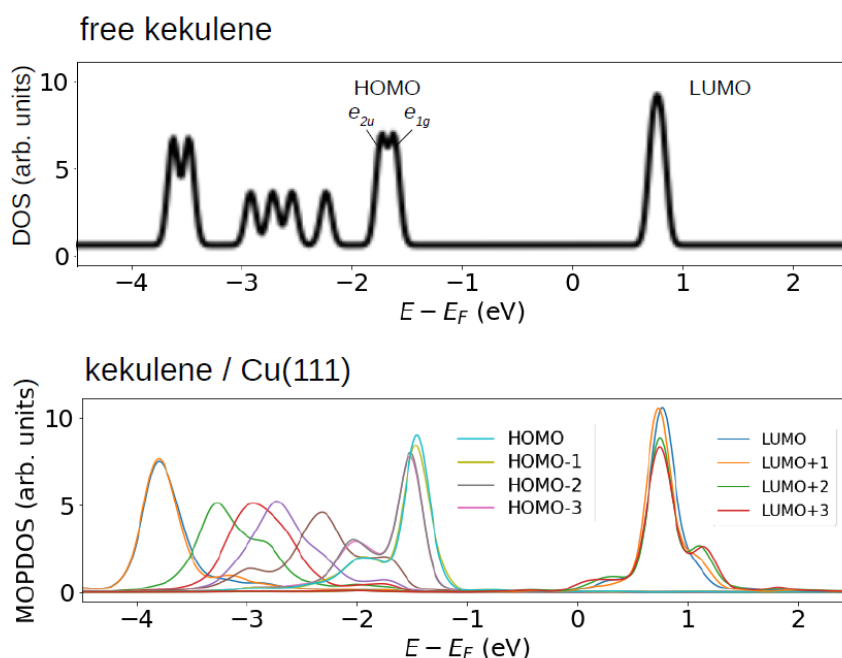


Fig. 3.9 Comparison between the free kekulene and the kekulene/Cu(111) system of the molecular orbital projected density of states (MOPDOS). In the case of the free kekulene the binding energy is compared to the vacuum energy, while for the kekulene/Cu(111) system the energy is compared to the fermi level, setting the fermi level at 0 eV. A Gaussian broadening of 0.1 eV was employed in the computed spectra.

3.1.6 Photoemission Intensity

To analyze the electronic structure of the kekulene/Cu(111) system, photoemission momentum maps (k-maps) (cf. Chapter 2.4) have been calculated using Eq. 2.50. These have been compared to k-maps calculations done for the free kekulene system^[89] as well as to experimental ARPES k-maps.

For the photoemission intensity simulations of the kekulene/Cu(111) system, the geometry of the energetically most optimal configuration (cf. Chapter 3.1.2) was used, as in Chapter 3.1.5. The k-point mesh was set to $3 \times 3 \times 1$ for all the simulations. Since the DOS of kekulene/Cu(111) (cf. Fig. 3.8) has shown that the HOMO is located on the onset of the Cu d-states, a damped plane wave (cf. eq. 2.54) has to be used for the photoemission intensity simulations, otherwise the substrate interference will be too strong to identify the molecular orbital.

For the damped plane wave the damping parameter γ was set to 0.5 \AA^{-1} and z_0 was set to be half way between the kekulene molecule and the Cu(111) substrate. Both, the experimental as well as the theoretical k-maps used a photon energy of $h\nu = 35 \text{ eV}$. The polarization factor has been considered and an angle of incidence of 60° has been presumed. The resulting k-maps can be seen in Fig. 3.10. The binding energies of these k-maps have been calculated for binding energies suggested from the DOS and MOPDOS results given in Fig. 3.8 and Fig. 3.9.

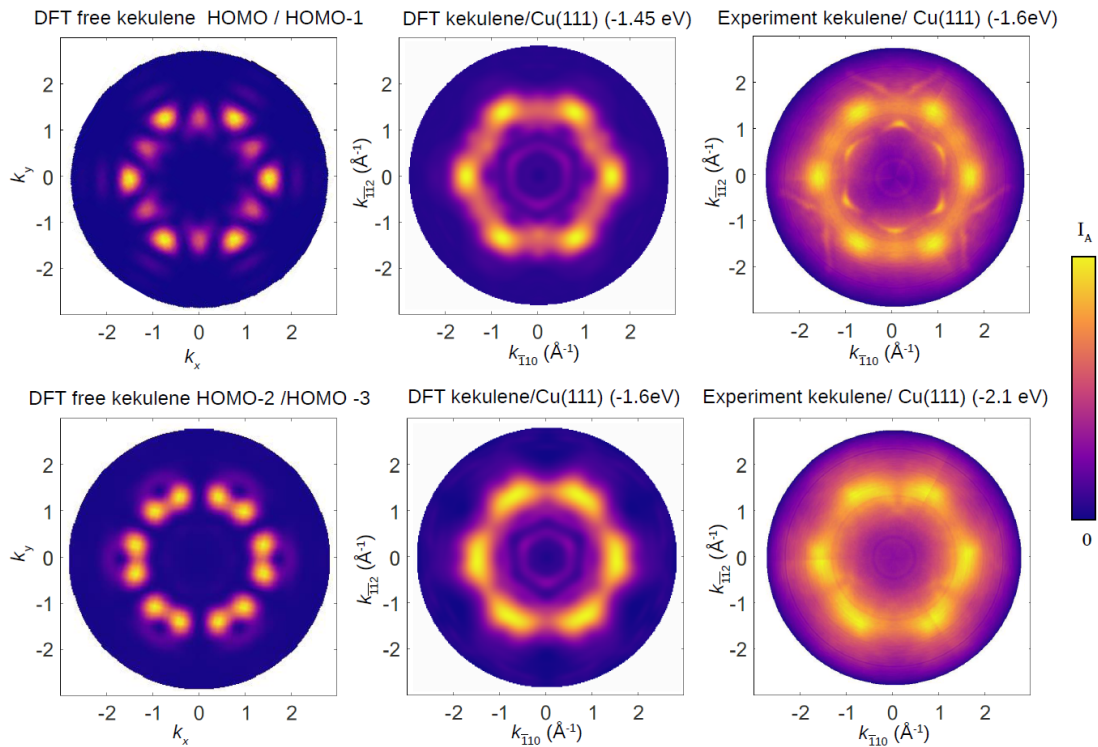


Fig. 3.10 The top row represents the theoretical k-maps of free kekulene at the binding energy of the HOMO/HOMO-1 (left panel) in comparison with theoretical k-maps from the kekulene/Cu(111) system (middle panel) and experimental angle-resolved photoemission k-maps of kekulene on Cu(111) (right panel) at the respective binding energy of the HOMO/HOMO-1 orbitals. The bottom row shows the k-maps at the binding energy of the HOMO-2/HOMO-3 for the same systems.

The first row shows a superposition of the doubly degenerate orbital HOMO and HOMO-1 of free kekulene (left), DFT calculated kekulene/Cu(111) (middle) and ARPES results for kekulene/Cu(111) (right). The second row shows the k-maps for the double degenerate orbital HOMO-2 and HOMO-3 for the same systems.

For the emission feature at $E_B = -1.6$ eV, the experimental k-map clearly resembles the calculated HOMO/HOMO-1 maps, both, for the free and the adsorbed molecule. In the case of the ARPES measurements, a stronger background intensity can be noticed which most likely comes from the Cu(111) substrate. Because damped plane wave were used in the theoretical k-maps of the kekulene/Cu(111) systems this background intensity is missing.

The HOMO-2/HOMO-3 case, depicted in the bottom row of Fig. 3.10, also shows a clear resemblance between the theoretical and experimental k-maps of kekulene/Cu(111). However, the resemblance between the k-maps of kekulene/Cu(111) (middle and right side) and free kekulene (left side), is not as clear. This is most likely due to the lifting of the degeneracy which already could be seen in the MOPDOS (cf. Fig. 3.9) as well as the binding energy being closer to the range in which the Cu(111) d-band is dominating as seen in the DOS (cf. Fig. 3.8).

In both the theoretical as well as the experimental k-maps of kekulene/Cu(111) system a change from a 6-fold symmetry towards a 3-fold symmetry of the kekulene's nodal structure can be observed. In the case of HOMO/HOMO-1 this can only slightly be seen with the minor nodes alternating in intensity. This is visualized more clearly in the azimuthal intensity line scans analyzed further below (cf. Fig. 3.13). For the HOMO-2/HOMO-3 the symmetry break towards 3-fold symmetry can very explicitly be seen by the shift of the major nodes towards each other. This shift might be due to the adsorption position, which if true would give more evidence that the theoretically predicted adsorption position (cf. Tab. 3.1) is indeed correct. For this purpose k-maps in the range of the HOMO-2/HOMO-3 have also been calculated for kekulene on Cu(111) in the other three adsorption positions, but keeping the same azimuthal orientation.

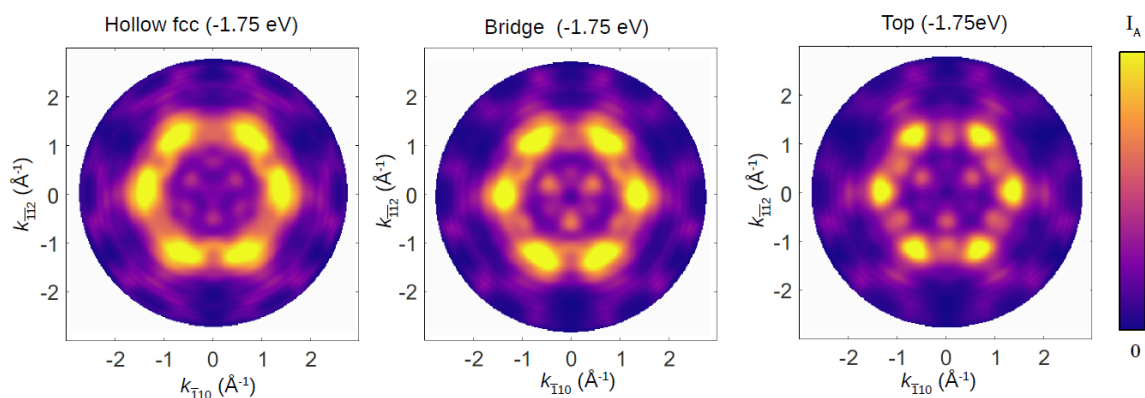


Fig. 3.11 Comparison between simulated photoemission k-maps of different kekulene/Cu(111) configurations at a binding energy in the range of the HOMO-2/HOMO-3 orbitals. Here the adsorption position of kekulene in the hollow-fcc, bridge and top position are compared.

It can be seen in Fig. 3.11 that in the hollow position, the symmetry breaking from 6-fold to 3-fold is the strongest and resembles the experimental results the best. In the bridge position, bright spots shift only very slightly and in the top position the major nodes, coming from kekulene, appear to still hold 6-fold symmetry.

It can also be observed, that the shift of the major nodes towards each other, in the k-map of kekulene in the hollow fcc position of Cu(111) (cf. Fig. 3.11 left side), is mirrored around the $k_{\bar{1}10}$ axis, when compared to the k-map of kekulene/Cu(111) in the hollow hcp position (cf. Fig. 3.10). This is most likely due to the position of kekulene's carbon backbone relative to the Cu atoms in the first layer, which can also be seen as mirrored when comparing the hollow hcp and fcc positions. This result suggests that the symmetry breaking is indeed due to the molecule-substrate interactions and the k-map of kekulene in the hollow hcp position has the best agreement to experimental data.

We now move on to discuss additionally calculated photoemission momentum maps, which have been made from the previously mentioned geometric model based on the S parameter (cf. Chapter 3.1.3), as well as the Hückel model (cf. Chapter. 3.1.4). In particular the HOMO/HOMO-1 orbitals are compared to the theoretical and experimental k-maps of the kekulene/Cu(111) system, to further analyze the electronic and aromatic structure of kekulene.

For the geometric models, three different S values have been considered: $S = 0$ (representing the AWA model), $S = 1$ (representing the Clar model) and $S = 0.5$ (representing an intermediate structure in between the AWA and Clar structures). For the Hückel model also three different k-maps have been calculated based on varying the hopping parameter t , with $t = 0$ eV (no inter-ring coupling, representing the AWA model), $t = -3.5$ eV (inter-ring coupling, representing the Clar model) and $t = -1.5$ eV (an intermediate inter-ring coupling). The resulting k-maps can be seen in Fig. 3.12.

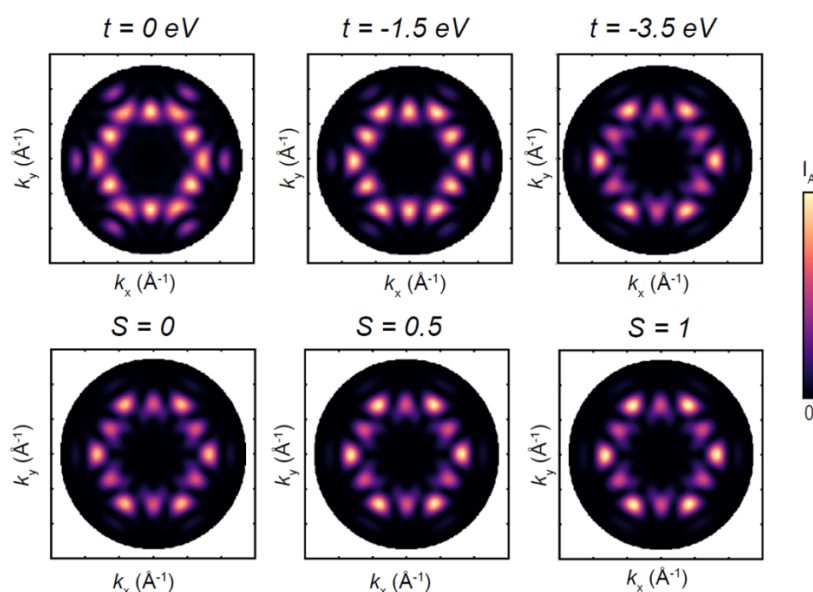


Fig. 3.12 Comparison between simulated photoemission k-maps of the HOMO/HOMO-1 orbitals using the Hückel model (left three panels) in which the electronic inter-ring coupling t was varied from 0 eV to 3.5 eV and using the geometric models were the S -value was varied, from 0 (AWA) to 1 (Clar). The maximum of the Intensity in the color-map was kept constant for the variation of each model.

Fig. 3.12 shows that the k-maps from the Hückel model, with varying inter-ring coupling, exhibit some slight change in the intensity of the lobes. The k-maps of the geometric model, however, are all very similar in nature and no clear difference can be seen with the bare eye.

To quantify the k-maps presented in Fig. 3.12, an intensity analysis was performed on the k-maps from the two extremes of each model ($S = 1$ and $S = 0$ for the geometric model and $t = -3.5$ eV and $t = 0$ eV for the Hückel model) and compared to experimental and theoretical k-maps of the kekulene/Cu(111) system with a binding energy in the range of the HOMO/HOMO-1 orbitals.

All intensities between the two k_{\parallel} -values, 1.3\AA and 1.8\AA , have been averaged and measured along an angle φ , indicated by the white lines in Fig. 3.13 (a-f). The resulting intensity curves can be seen in Fig. 3.13 (g-i).

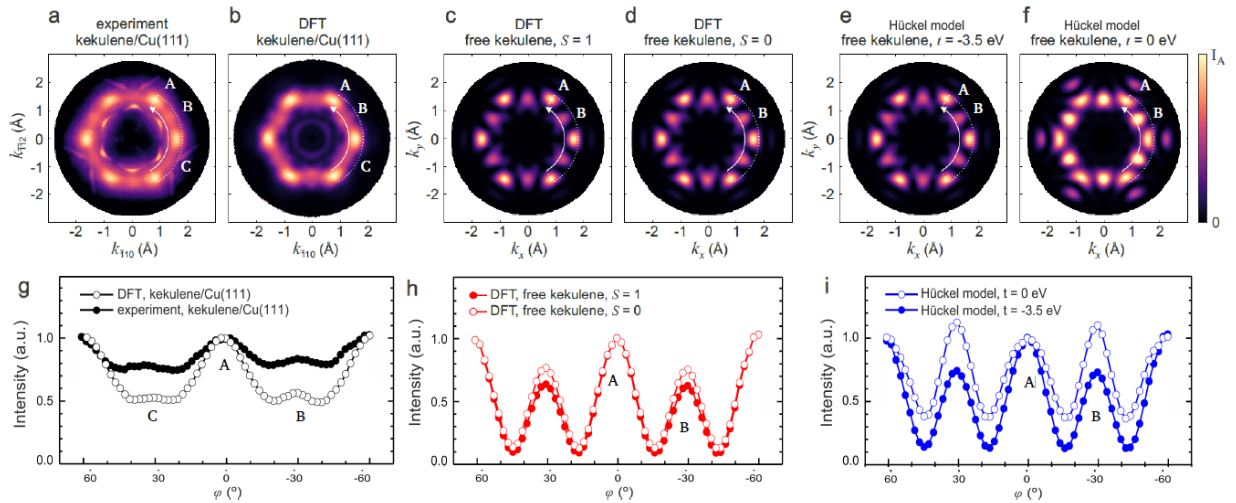


Fig. 3.13 Difference in intensity of k-maps of kekulene/Cu(111) and free kekulene systems. The intensity is plotted along a line circumfering the k-maps illustrated by the arrow in each k-map image. The nodes in the k-maps are labeled as A,B or C. (a-f) show the varies k-maps, gained from angle resolved photoemission measurements of the kekulene/Cu(111) (a), theoretical simulations of the kekulene/Cu(111) system (b), the geometrical model of free kekulene with $S = 1$ (c) and $S = 0$ (d) and the Hückel model of free kekulene with $t = -3.5$ eV (e) and $t = 0$ eV (f). (g-h) show the plotting of the intensity of each before mentioned k-map along the path indicated by the arrow. (g) shows the comparison between the theoretical and experimental k-maps of kekulene/Cu(111). (h) shows the comparison among the geometric model between $S = 1$ and $S = 0$ and (i) shows the comparison among the Hückel model between $t = -3.5$ eV and $t = 0$ eV. This image was taken from Ref. [10] and slightly altered.

In each k-map a circle with twelve lobes can be seen. 6 of these have been denoted as major lobes (lobe A) and 6 of these as minor lobes (lobe B). In the case of kekulene/Cu(111), the additional denotation of lobe C was used, because there appear to be two groups of minor lobes, which differ in intensity. When comparing two k-maps the intensity of the major lode A has been set identical. In the case of the k-maps of kekulene/Cu(111) (cf. Fig. 3.13(g)) some similarities between theoretical and experimental k-maps are noticeable. In both cases there is a difference in intensity between the minor nodes B and C, which also appear to be of the same magnitude. This is, most likely, due to the previously mentioned symmetry break. However the background intensity from the Cu(111) substrate is higher in the experimental k-

map and therefore can be seen in an overall higher intensity in the curve. In the case of the DFT calculated k-maps of kekulene/Cu(111) an overall higher intensity compared to the k-maps from the free kekulene system can be seen, due to a background contribution from the Cu(111) substrate. This contribution however smaller compared to the experimental k-maps because of the damped plane wave approach which has been utilized.

Fig. 3.13 (h) shows that the change of intensity influenced by the geometric structure of free kekulene is only minor in nature, however a slight decrease in intensity of the node B can be seen for $S = 1$. This gives the impression that the electronic structure of kekulene is insensitive to geometrical variations and it is not clear, if the proposed electronic structure of the AWA model, e.g. weak inter-ring coupling has been achieved by fixing the geometric structure. Therefore, the Hückel model, in which the inter-ring coupling was directly adjusted can better describe the electron structure difference between the Clar and the AWA model. When looking at Fig. 3.13 (i) it is noticeable that for kekulene with no inter-ring coupling ($t = 0$ eV) the intensity trend of the two nodes A and B is inverted compared to all other k-maps, making it an outlier. The k-map of kekulene with inter-ring coupling ($t = -3.5$ eV), however, shows no major deviations from the other k-maps, making the corresponding electronic structure to be the preferred one. Since the theoretical AWA model proposes low coupling between the inner and outer annulene rings of kekulene, compared to the Clar model higher coupling, this gives further indication that the AWA model can be ruled out as the aromatic structure which kekulene follows.

3.1.7 Electron Density and Molecular Orbitals

The electron charge density distribution of the degenerate frontier orbitals HOMO and HOMO-1 can give further insights about the behavior of the electrons in the kekulene system. For this purpose the plane-averaged charge density, as well as the charge rearrangement of kekulene on Cu(111) (6 layer), along the [111] direction of the Cu(111) substrate, has been calculated. The charge rearrangement depicts the change of kekulene's electron charge density, when comparing the adsorbed system to the two isolated cases free kekulene and free Cu(111). The result can be seen in Fig. 3.14.

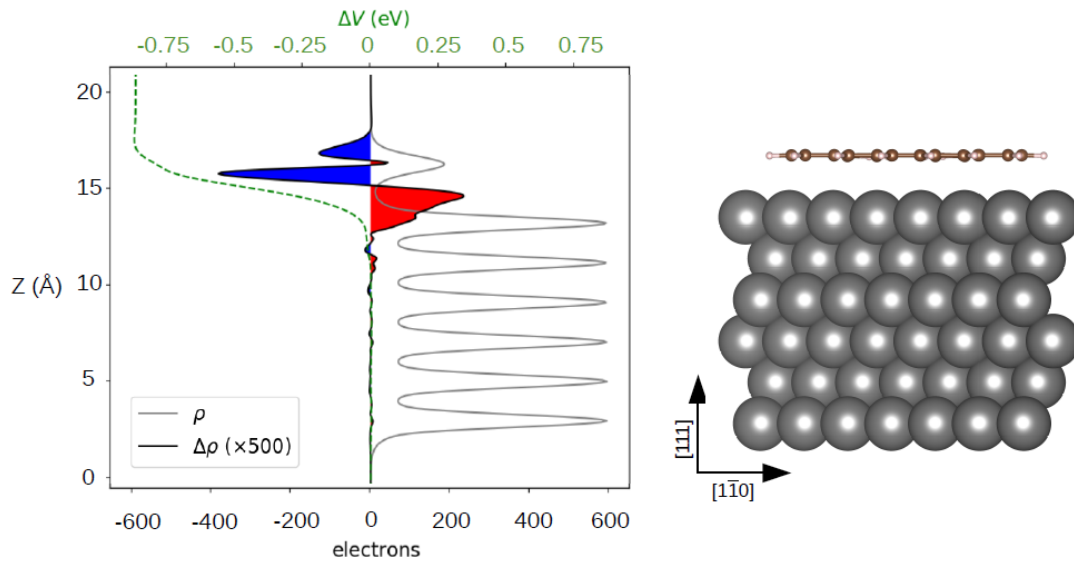


Fig. 3.14 Charge rearrangement of kekulene on 6 layer of Cu(111). The plane-averaged charge density along the [111] direction of Cu(111) is given by $\rho(z) = \frac{1}{A} \int \int dx dy \rho(\vec{r})$. The difference in charge density from the kekulene/Cu(111) system to the free gas phase kekulene and isolated Cu(111) system is given by $\Delta\rho$ (the graph is multiplied by a factor of 500). The change in the electrostatic potential is denoted by ΔV [eV], which is gained from the two times integration of $\Delta\rho = \rho_{total} - (\rho_{surf} + \rho_{mol})$.

The charge rearrangement given by Fig. 3.14 and the previous findings that no charge transfer is observed (cf. Chapter 3.1.5) indicates the so-called Pauli push back effect, in which the electrons of the molecule push electrons back into the substrate. This leads to a decreased surface dipole, indicated by the electrostatic potential ΔV . It leads to a decreased work function, which has been calculated to $\Delta\Phi = -0.754$ eV. The adsorption height of around 3\AA also indicates an adsorption in the range of physisorption, which means that the electrons of the molecule as well as the substrate are barely disturbed by the adsorption.

The particle charge density obtained by $\rho(\vec{r}) = \sum_{\vec{k}}^{BZ} \sum_n^{\varepsilon_1 < \varepsilon_{n\vec{k}} < \varepsilon_2} |\varphi_{n\vec{k}}(\vec{r})|^2$, taking into account all states in the energy window $[\varepsilon_1, \varepsilon_2]$ has also been calculated. Here, the energy window has been set to $\varepsilon_2 - \varepsilon_1 = 0.5$ eV, centered around the doubly degenerate frontier orbital HOMO/HOMO-1. The kekulene/Cu(111) system has been compared to the geometry model of free kekulene in which the S-value has been varied (from $S = 0$ to $S = 1$) and the Hückel model in which the coupling of the inner and outer annulene circuit of kekulene has been varied (from $t = 0$ eV to $t = -3.5$ eV). The results can be seen in Fig. 3.15.

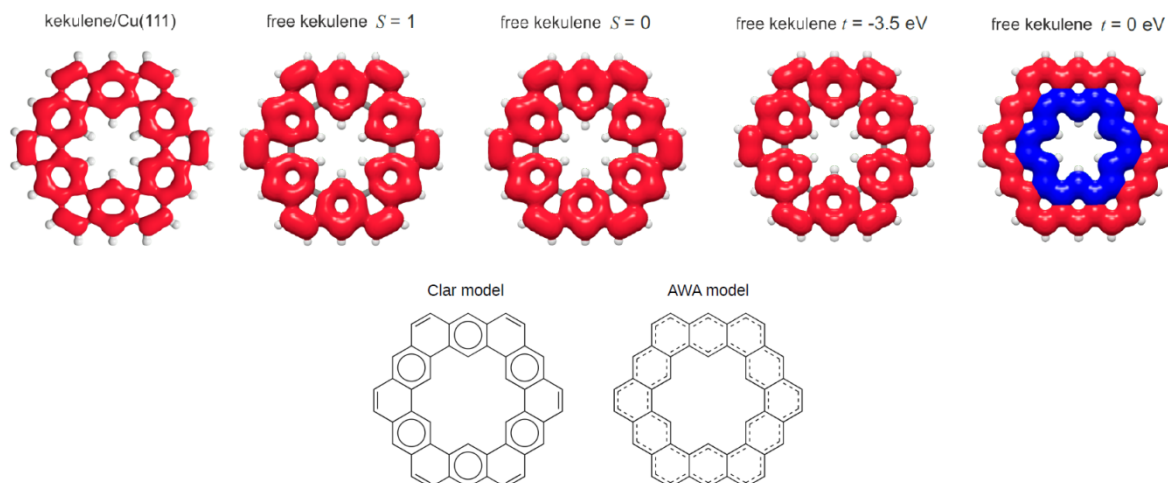


Fig. 3.15 The comparison of calculated electron density distribution plots of theoretical kekulene/Cu(111) and free kekulene systems. The comparison is between the DFT-optimized kekulene/Cu(111) structure and the DFT-optimized of free kekulene corresponding to the structural parameter $S=1$ and $S=0$ and the Hückel model corresponding to the hopping integral $t = -3.5$ eV and $t = 0$ eV, between inner and outer ring. The electron density cutoff value for the iso-surface is set to 0.0003 electron/Å³. In addition, the theoretical Clar and AWA model describing the aromaticity of kekulene is depicted as reference.

When comparing the charge density distribution of the kekulene/Cu(111) system to the theoretical Clar model and the AWA model, a clear agreement between the Clar model and the DFT calculated kekulene/Cu(111) system can be seen. The outer most bond (bond e cf. Fig. 3.3 in Chapter 3.1.3), which the Clar model proposed as a double bond shows a high electron density and the benzene units of kekulene, which are postulated as aromatic π -sextets in the Clar model, show also increased electron density along their cycles. Contrary, the bonds which are postulated by the Clar model as single bonds have decreased electron density. The same resemblance is also noticeable in both cases of the geometrical model ($S=0$ and $S=1$) and the Hückel model, allowing inter-ring coupling ($t = -3.5$ eV). The only model which does not agree with the DFT results for the charge density distribution for kekulene/Cu(111) are the one found in the Hückel model, which suppresses the coupling between the annulene rings ($t = 0$ eV). This model incorporates the postulations of the AWA model and therefore shows that the Clar model is the preferred model of kekulene in the findings of the charge density distribution.

Furthermore, in order to see if the nodal structure of the frontier orbitals can give further insights of the aromaticity of kekulene, real space distributions from the nodal structure of the HOMO and HOMO-1 have been calculated. For this the free kekulene system as well as the four previously used model cases ($S = 0$ and $S = 1$ for the geometric model and $t = 0$ eV and $t = -3.5$ eV for the Hückel model) were calculated using a hybrid functional B3LYP (cf. Chapter 2.1.3). The results can be seen in Fig. 3.16.

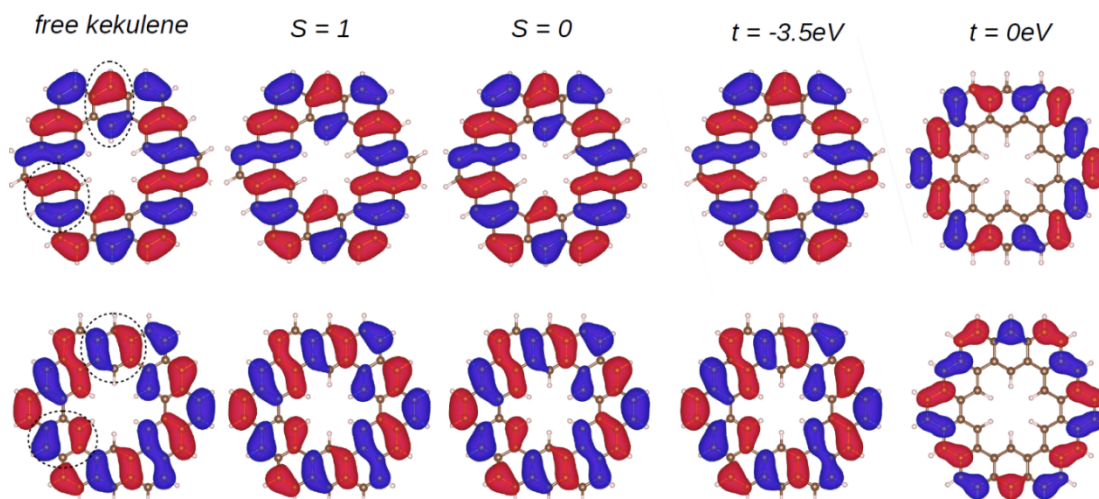


Fig. 3.16 The degenerate HOMO and HOMO-1 of free kekulene compared to the geometric model dependent on the S -value and the Hückel model dependent on the inner ring coupling t .

The molecular orbital nodal structures show that the molecular orbitals of free kekulene is not confined to either the inner nor the outer annulene circuit, except in the case where inter-ring coupling was suppressed ($t = 0$ eV). All other cases show a similar nodal structure, which also has benzene-like HOMO nodal features (indicated by the dashed circles). These benzene-like HOMO nodal structures also appear at precisely the same location in the kekulene structure as the Clar model postulates aromatic π -sextets. This is a further indication that Clar's sextet model gives a better description of kekulene's aromatic structure over the AWA model. Geometric changes of bond lengths show to have only a minimal effect on the nodal structure of the frontier orbitals, which gives additional indications that geometric variations of kekulene's bond lengths have not led to significant changes in its electronic properties.

3.1.8 Conclusion

When adsorbing kekulene on a Cu(111) substrate, the hollow hcp position has been found to be the energetically most favorable adsorption site with the orientation of kekulene's apothem parallel to the $[\bar{1}12]$ direction of the Cu(111) substrate. The adsorption energy in this configuration was found to be approximately -6 eV and an adsorption height of 3.05 Å, depending on the number of Cu layer used. Together with the findings of the projected density of states calculations (MOPDOS), which concluded that no charge transfer can be observed, this gives an indication that kekulene physisorbs on Cu(111).

The HOMA analysis of kekulene's geometric structure indicates the Clar model as kekulene's preferred aromatic arrangement. With the help of an interpolation model an estimate has been made to determine where the geometric structure of DFT calculated kekulene lies in between the Clar and AWA model. This interpolation model indicates an agreement of kekulene to the Clar model with around 70-80%, however the margin of error is high and in further investigations of the electronic structure of kekulene (photoemission momentum maps, charge density distribution and real space distribution of frontier orbitals), the geometric model proved to not be a reliable indicator of changes in aromaticity. This showed that by fixing the geometric structure of the AWA model of kekulene's aromaticity, one cannot force the electronic structure to follow the same model, i.e., geometric alterations do not necessarily lead to the same degree of electronic changes in a structure.

An agreement between experimental and theoretical photoemission momentum maps for the kekulene/Cu(111) system, in the binding energy range of the doubly degenerate frontier orbital HOMO and HOMO-1, gave further confirmation of the theoretically predicted energetically favorable adsorption site. Additional investigations into the intensity distribution of k-maps of kekulene/Cu(111) and the free kekulene favored the Clar model of kekulene's aromaticity over the AWA model. The comparison between these two systems showed that inter-ring coupling of the outer [30]-annulene circuit surrounding kekulene and the inner [18]-annulene circuit inside kekulene can be seen, which is contrary to the AWA model postulating weak inter-ring coupling.

Finally, the nodal structure and the charge density distribution of the molecular frontier orbitals also indicate that the Clar sextet model is the preferred model of kekulene's aromaticity. In the charge density distribution, a clear increased charge density in the aromatic π -sextets can be seen, and in the nodal structure, of kekulene's frontier orbitals, benzene-like HOMO nodal features can be seen at the exact positions where the Clar model postulates aromatic π -sextets.

3.2 Kekulene/Cu(110)

3.2.1 Motivation

To further analyze the electronic and aromatic properties of kekulene, it is interesting to test, how the adsorption on a 2-fold symmetric substrate affects kekulene's electronic structure.

The substrate which has been chosen for this purpose is Cu(110). First, kekulene's energetically most favorable adsorption configuration was investigated, revealing the optimal geometry, thus the adsorption height and the adsorption energy. Then, the aromaticity of kekulene/Cu(110) in its most favorable adsorption configuration was studied and compared to the previous case of kekulene/Cu(111). Furthermore, the electronic structure of the kekulene/Cu(110) system was analyzed using the DOS (cf. Chapter 2.4), photoemission intensity (cf. Chapter 2.5), charge rearrangement and the real space distribution of the frontier orbitals, including its corresponding charge density.

After looking into the aromatic and electronic properties of kekulene/Cu(110), the experimental STM results of the on-surface synthesis of kekulene on Cu(111) and Cu(110) have been analyzed. It has been identified that on Cu(110), other reaction products, besides kekulene are present to a large degree. The other, yet unknown reaction product, is believed the so-called "iso-kekulene", which can be found on a substrate in two different configurations, which we tentatively term "iso-kekulene up" and "iso-kekulene down". A more detailed description of "iso-kekulene" will be given in Chapter 3.2.5, as well as looking at "iso-kekulene's" adsorption geometry.

Lastly, nc-AFM and IETS-STM simulations have been created, utilizing the probe particle model (cf. Chapter 2.7), to better identify various kekulene-like surface species on the Cu(110) substrate. Experimental nc-AFM and IETS-STM results to confirm the findings of STM (cf. Fig 3.17) have yet to be made.

3.2.2 Geometric Optimization

The equilibrium geometry of the kekulene/Cu(110) system has been calculated in similar fashion to the geometric optimization calculations of the kekulene/Cu(111) system, discussed in Chapter 3.1.2, with the PBE-GGA+TS approach. The same lattice parameter and repeated slab approach setup has been chosen. The supercell, however, could be chosen smaller, because a 5×7 supercell already ensures, that the kekulene molecules are far enough apart. Using three layers for the Cu(110) substrate and allowing all degrees of freedom has shown to be problematic for the kekulene/Cu(110) system, because of the stronger molecule/substrate interaction. A small number of Cu(110) layers leads to unrealistic effects in the simulated molecule/metal interface, such as copper atoms moving out of the slab. In order to reduce this effects the number of Cu(110) layers has been increased to 5 and the bottom 3 copper layers have been frozen in space, only allowing all degrees of freedom for the two topmost layers of the Cu(110) slab.

Similar to the Cu(111) setup, four different adsorption sites and two different azimuthal orientations have been analyzed differing by 30 degrees from each other. The adsorption sites which have been considered are the top, short bridge, long bridge and hollow position of the Cu(110) substrate (cf. Fig. 2.1). The two azimuthal orientations are depicted in Fig. 3.17, both with kekulene in the long bridge position of Cu(110). When kekulene's apothem (red arrow) is parallel to the $[0\ 0\ 1]$ direction of Cu(110) (a) it is denoted as "orientation 1" and when kekulene's apothem is parallel to the $[-1\ 1\ 0]$ direction of Cu(110) (b) it is denoted as "orientation 2". The resulting adsorption heights and total energy difference, for the above mentioned setup, can be seen in Tab. 3.6.

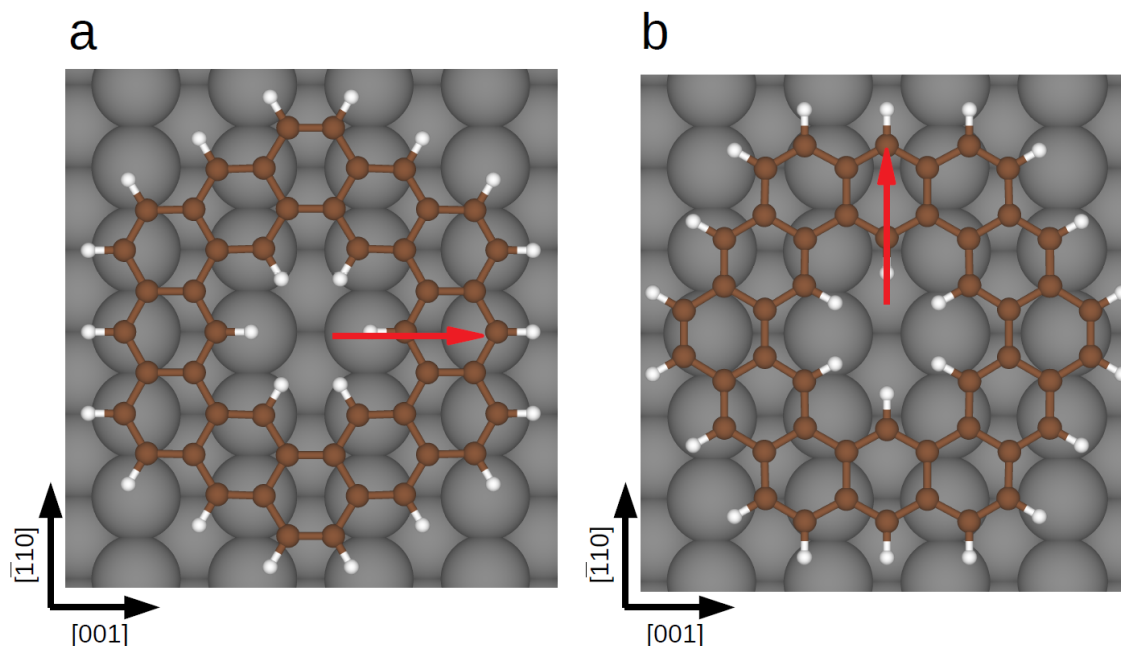


Fig. 3.17 Structural models of kekulene/Cu(110) for the two principle azimuthal orientations. Both (a) and (b) are in the long bridge adsorption position of Cu(110). (a) shows kekulene's apothem (red arrow) oriented parallel to the $[0\ 0\ 1]$ direction of the Cu(110) substrate, which is denoted as "orientation 1", while (b) shows kekulene's apothem oriented parallel to the $[-1\ 1\ 0]$ direction of the Cu(110) substrate, which is denoted as "orientation 2".

Tab. 3.6 Average carbon height h_c [Å] and difference in total energy E [eV] of kekulene on Cu(110) obtained for the four different adsorption positions and two different azimuthal orientations. The difference in total energy ΔE [eV] was measured by setting the configuration with the lowest total energy to 0 and comparing the remaining configurations to the most favorable.

Adsorption position	Orientation	h_c [Å]	E [eV]	ΔE [eV]
top	1	2.54	-1185.21	1.28
short bridge	1	2.46	-1185.82	0.67
long bridge	1	2.41	-1186.49	0
hollow	1	2.48	-1185.98	0.51
top	2	2.52	-1185.76	0.73
short bridge	2	2.39	-1185.93	0.55
long bridge	2	2.43	-1185.75	0.73
hollow	2	2.37	-1185.70	0.79

It can be seen, that the energetically most favorable adsorption configuration is the long bridge position, with the azimuthal orientation of kekulene's apothem parallel to the [001] direction. The adsorption energy of this configuration was calculated to be -7.8 eV.

From the different configurations of kekulene on Cu(110), it seems that the lowest adsorption height (2.37 Å, for the hollow adsorption position with orientation 2) does not correlate with the energetically best configuration. This is in contrast to the case of Cu(111) (cf. Chapter 3.1.2). However, this is only the case when looking at the adsorption height of only the carbon atoms, as was done similarly in the case of kekulene/Cu(111). When including the hydrogens in calculating the average adsorption height, the long bridge position in orientation 1 has the lowest adsorption height with 2.423 Å, while the hollow position in orientation 2 has a total adsorption height of 2.433 Å.

Because of the less-coordinated Cu(110) surface and its concomitant higher reactivity, it is expected to see higher molecule/substrate interaction and therefore possible molecule deformation. Therefore, an atom-resolved adsorption heights analysis of the kekulene molecule has been conducted. A comparison between kekulene/Cu(110) to kekulene/Cu(111) can be seen in Fig. 3.18.

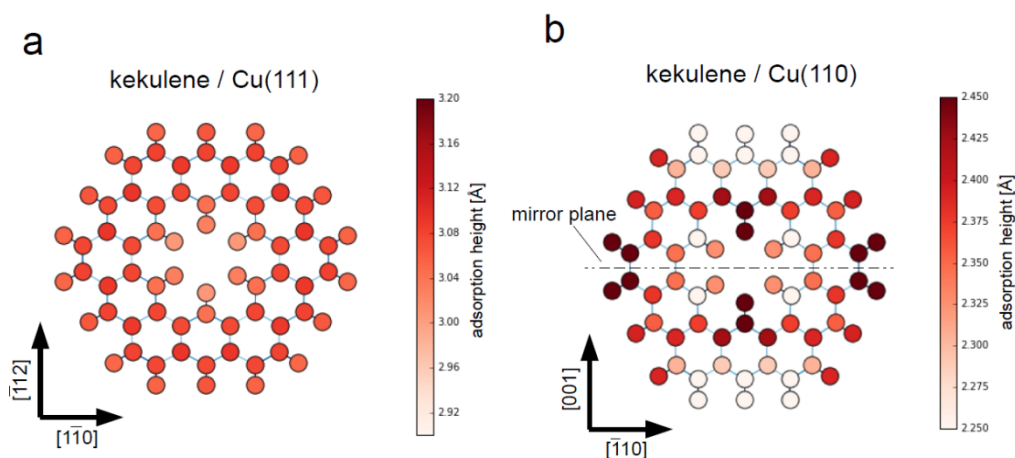


Fig. 3.18 Atom-resolved adsorption heights of each atom of kekulene/Cu(111) compared to kekulene/Cu(110).

The adsorption heights of the individual atoms of kekulene adsorbed on Cu(111) (cf. Fig. 3.18 (a)) resembles free kekulene. Strictly speaking, free kekulene belongs to the symmetry group D_{3d} , because of the slight alternating bending of the inner hydrogen atoms. The alternating bending of the hydrogen atoms, which can hardly be seen in Fig. 3.18 (a), but amounts to 0.02 Å. The carbon atoms and outer hydrogen atoms of kekulene appears to be 6-fold symmetric. The corrugation of kekulene adsorbed on Cu(111), has been calculated to be between 0.05 Å and 0.15 Å, depending on the adsorption configuration.

When looking at the adsorption height of the individual atoms of kekulene adsorbed on Cu(110) (cf. Fig. 3.18 (b)), kekulene appears bent along the $[-1\ 1\ 0]$ axis towards the Cu(110) substrate, meaning that atoms further away from symmetry line, parallel to the $[-1\ 1\ 0]$ axis, have a smaller adsorption height. As a result, kekulene becomes 2-fold symmetric, rather than the 6-fold (or 3-fold considering the inner hydrogens) as seen by kekulene/Cu(111). The corrugation of kekulene, adsorbed on Cu(110), ranges between 0.3 Å and 0.4 Å, depending on the adsorption configuration, and is therefore significantly larger than on Cu(111).

3.2.3 Aromaticity

In analogy to Chapter 3.1.3, the HOMA concept is applied to assess the aromaticity of kekulene/Cu(110), and will be compared to HOMA values of kekulene/Cu(111) and to the Clar and AWA model (cf. Chapter 3.1.3). For this analysis, the same optimal bond length $R_{opt} = 1.403\text{Å}$, gained from the reference molecule trans-1,3 butadiene (cf. Appendix A) has been used.

The bond lengths and HOMA values of kekulene/Cu(110) in its energetically most favorable adsorption configuration (long bridge position, with orientation 1), as well as a comparison to the bond lengths of the kekulene/Cu(111) system are given in Fig. 3.19.

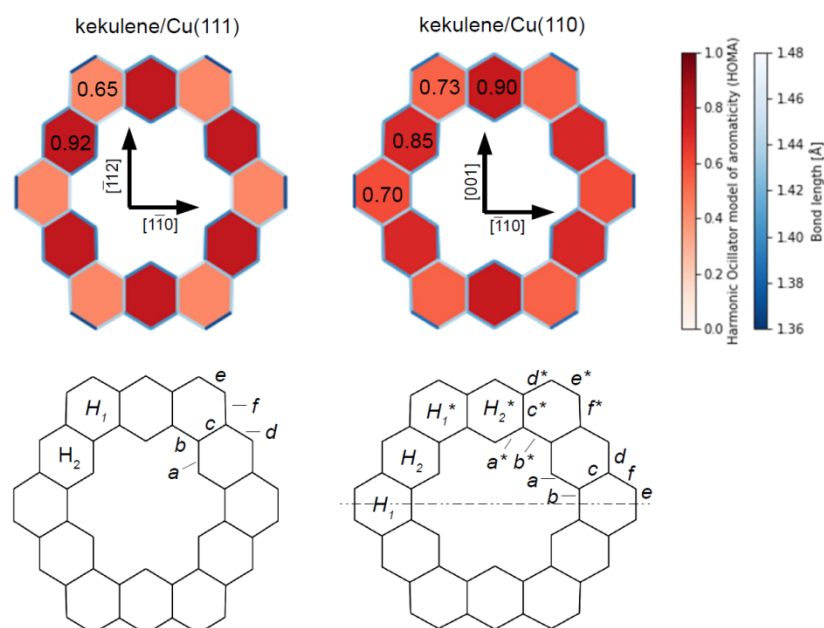


Fig. 3.19 HOMA comparison and labelling of the bonds of kekulene/Cu(111) and kekulene/Cu(110). For the kekulene/Cu(110) system, a difference between the bonds closer and further away from the 2-fold symmetry line have been noticed, which is why additional bond labels are introduced.

The bond lengths and HOMA values of kekulene on Cu(110) show a 2-fold symmetry, as previously described. It has to be noted that due to kekulene's distortion on Cu(110) more than six different bond labels are necessary to fully describe its geometric structure. Additional bonds have been introduced for kekulene/Cu(110), because of the 2-fold symmetry of kekulene. Therefore, two sets of six bond labels each are given, as depicted in Fig. 3.19. The comparison of each individual bond length, as well the HOMA values for individual benzene units and for the inner [18]-annulene and outer [30]-annulene ring are given in Tab. 3.7.

Tab. 3.7 Bond lengths in Å units and H values for AWA and Clar models of kekulene and for DFT-optimized kekulene/Cu(110) and kekulene/Cu(111).

bond	AWA model	kekulene /Cu(110)*	kekulene/Cu(111)	Clar model
a / a^*	1.403	1.414 / 1.404	1.397	1.403
b / b^*	1.403	1.424 / 1.443	1.452	1.456
c / c^*	1.456	1.434 / 1.425	1.431	1.403
d / d^*	1.403	1.407 / 1.418	1.407	1.403
e / e^*	1.403	1.373 / 1.388	1.370	1.350
f / f^*	1.403	1.43 / 1.427	1.437	1.456
H_1	0.735	0.702 / 0.734	0.651	0.472
H_2	0.735	0.851 / 0.904	0.923	1.000
$H_{[18]}$	1.000	0.842	0.767	0.735
$H_{[30]}$	1.000	0.835	0.802	0.526

*in the case of kekulene on Cu(110) the first number represent the bond lengths and corresponding HOMA values close to the mirror plane (cf. Fig. 3.19), which is along the $[-1\ 1\ 0]$ direction of Cu(110), while the second number represents the bond lengths and corresponding HOMA values further away from the mirror plane.

In the case of kekulene/Cu(110), the difference between H_1 and H_2 is smaller, compared to the case of kekulene/Cu(111), which would indicate a shift away from the aromatic structure in accordance to the Clar model and towards the superaromatic structure of the AWA model. The HOMA values for the inner and outer annulene ring, $H_{[18]}$ and $H_{[30]}$, respectively, appear also to have shifted towards the AWA model in the case of kekulene/Cu(110), which would suggest that the adsorption on Cu(110) makes kekulene more superaromatic. However, a thorough investigation into the electronic structure of kekulene/Cu(110) should first be conducted, before concluding the aromatic structure of kekulene/Cu(110).

3.2.4 Electronic Structure

To analyze the electronic structure of kekulene/Cu(110), firstly the total DOS (cf. Chapter 2.4), the projected DOS onto fragments of the total system as well as a molecular orbital projected DOS (MOPDOS) has been calculated. The results of these calculations can be seen in Fig. 3.20.

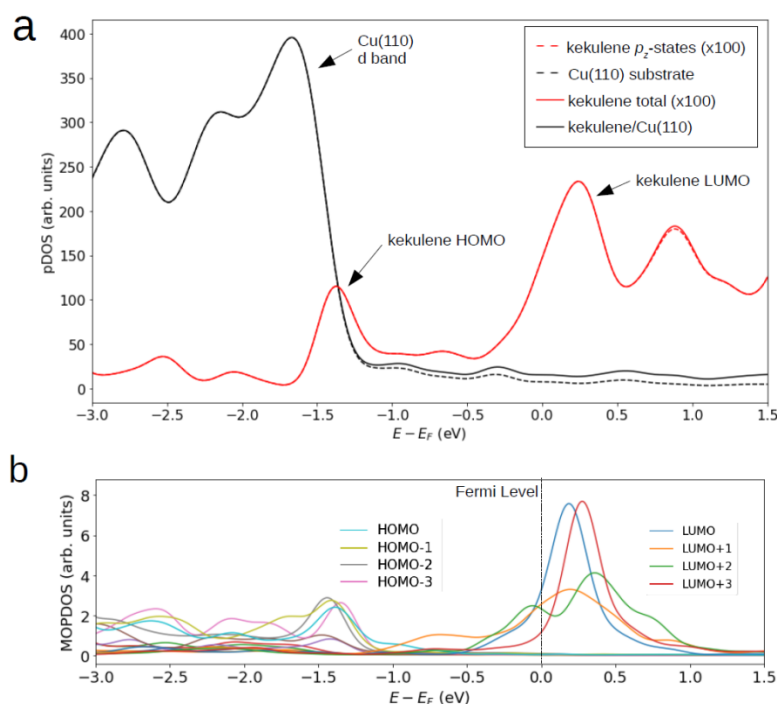


Fig. 3.20 (a) DFT calculated density of state (DOS) of kekulene/Cu(110) and the projected density of states (pDOS) of the kekulene molecule, as well as the Cu(110) substrate. (b) Molecular orbital projected density of states (MOPDOS) of kekulene. A Gaussian broadening of 0.1 eV was employed in the computed spectra.

Similar to the kekulene/Cu(111) system, it can be seen in Fig. 3.20(a), that for kekulene/Cu(110), the copper d-band is also dominating in the range of kekulene's HOMO. This suggests again that a damped plane wave (cf. Eq. 2.52) has to be used for the photoemission intensity simulations, otherwise the substrate emissions would be too strong to identify the molecular orbital.

The MOPDOS (cf. Fig. 3.20 (b)) of kekulene/Cu(110), however, differs from kekulene/Cu(111) (cf. Fig. 3.9). In the case of kekulene/Cu(110) the LUMO reaches beneath the Fermi-level indicating charge transfer into the LUMO. Also a higher lifting of the degeneracy of the LUMO/LUMO+1 and LUMO+2/LUMO+3 can be observed.

To further analyze the electronic structure of the frontier orbitals, photoemission momentum maps (k-maps) (cf. Chapter 2.4) of the kekulene/Cu(110) have been calculated and have been compared to experimental ARPES k-maps, and k-maps of free kekulene. The parameters of the theoretically calculated k-maps have been chosen similar to the case of kekulene/Cu(111) (cf. Chapter 3.1.6). For the kekulene/Cu(110) system, the energetically most favorable

adsorption configuration has been chosen in accordance to Chapter 3.2.2, k-point mesh was set to $3 \times 3 \times 1$ and a damped plane wave with damping parameter of $\gamma = 0.5$ was employed with z_0 half way between the kekulene molecule and the Cu(111) substrate. Both the experimental as well as the theoretical k-maps used a photon energy of $h\nu = 35$ eV. The polarization factor has been considered and an angle of incidence of 60° has been presumed.

The resulting k-maps can be seen in Fig. 3.21. The binding energies of these k-maps have been chosen in accordance with the most prominent peaks visible in the DOS and MOPDOS results given in Fig. 3.20. The first row shows the doubly degenerate HOMO/HOMO-1 of free kekulene (left), as well as their superposition, DFT calculated kekulene/Cu(110) k-maps (middle) and ARPES results for kekulene/Cu(110) (right). The second row shows the k-maps for the doubly degenerate orbital LUMO for the same systems.

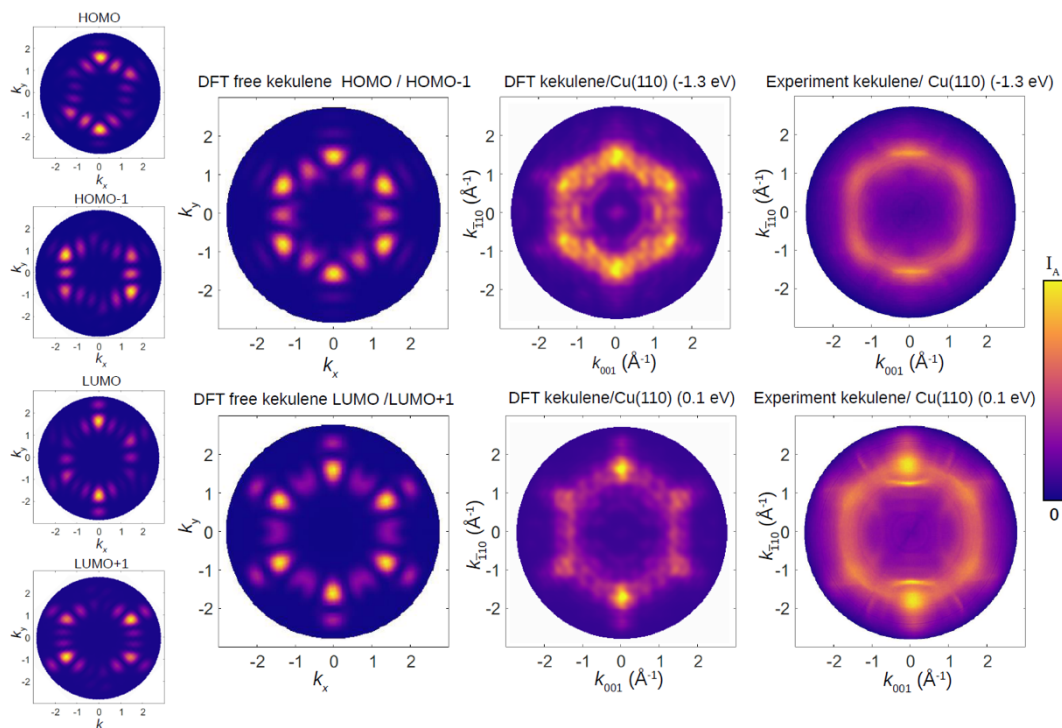


Fig. 3.21 The left side of the top row shows the individual k-maps, from free kekulene, of the HOMO and the HOMO-1, as well as a superposition of both of them. These k-maps of the free kekulene system were compared with theoretical k-maps from the kekulene/Cu(110) system (middle panel) and experimental angle-resolved photoemission k-maps of kekulene on Cu(110) (right panel) at the respective binding energy of the HOMO. The bottom row shows the k-maps at the binding energy of the LUMO/LUMO+1 for the same systems.

It can be seen that the theoretical and experimental k-maps of kekulene/Cu(110) show a clear resemblance in the range of the LUMO/LUMO+1 and somewhat of a resemblance at the range of the HOMO/HOMO-1. It can also be seen that the LUMO/LUMO+1 are occupied in the experiment.

There is also a clear lifting of the degeneracy of the orbitals visible in the case of the LUMO/LUMO+1, when comparing the kekulene/Cu(110) k-maps to the individual free kekulene k-maps of LUMO and LUMO+1. In the case of the HOMO/HOMO-1, also a slight lift in the degeneracy is visible.

In analogy to Chapter 3.1.7, the plane average charge density, as well as the charge rearrangement of the kekulene/Cu(110) system were calculated along the [110] direction of the Cu(110) substrate. The results can be seen in Fig. 3.22 as well as a size comparison to the simulated organic/metal interface.

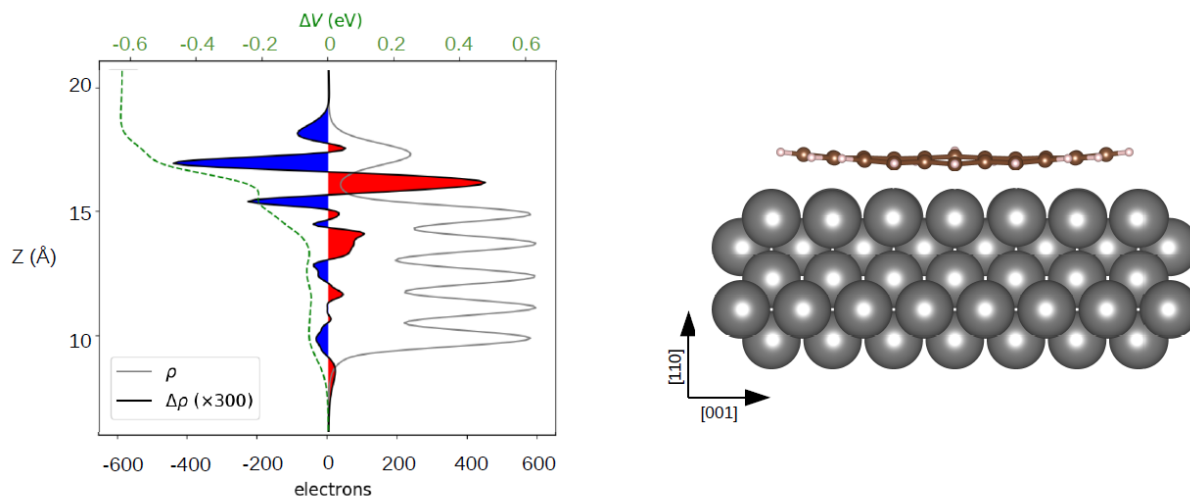


Fig. 3.22 Charge rearrangement of kekulene on 5 layer of Cu(110). The plane averaged charge density along the [110] direction of Cu(110) is given by ρ while the difference in charge density from the kekulene/Cu(110) system to the free gas phase kekulene and isolated Cu(110) system is given by $\Delta\rho$ (the graph is multiplied by a factor of 500). The change in the electrostatic potential is denoted by ΔV [eV], which is gained from the two times integration of $\Delta\rho$.

The decreased work function of the kekulene/Cu(110) has been calculated to $\Delta\Phi = -0.576$ eV. It can be seen that the charge rearrangements of kekulene/Cu(110) are stronger than in the case of kekulene/Cu(111) (cf. Fig. 3.14). This is due to the stronger molecule-surface interactions between Cu(110) and its adsorbates.

Furthermore, the real space distribution of the nodal structure of the doubly degenerate frontier orbitals HOMO and HOMO-1 have been calculated for isolated kekulene, but in the geometry adsorbed on Cu(110). This has been done to analyze the electronic interconnectivity of the outer [30]-annulene ring and the inner [18]-annulene ring of kekulene/Cu(110), similar to the case of free kekulene (cf. Fig. 3.16). Although in the case of kekulene/Cu(110), the degeneracy of these orbitals has been slightly lifted, the same labelling as in the case of free kekulene has been adapted here, to have a better comparison to the case of free kekulene. The resulting real space distribution can be seen in Fig. 3.23.

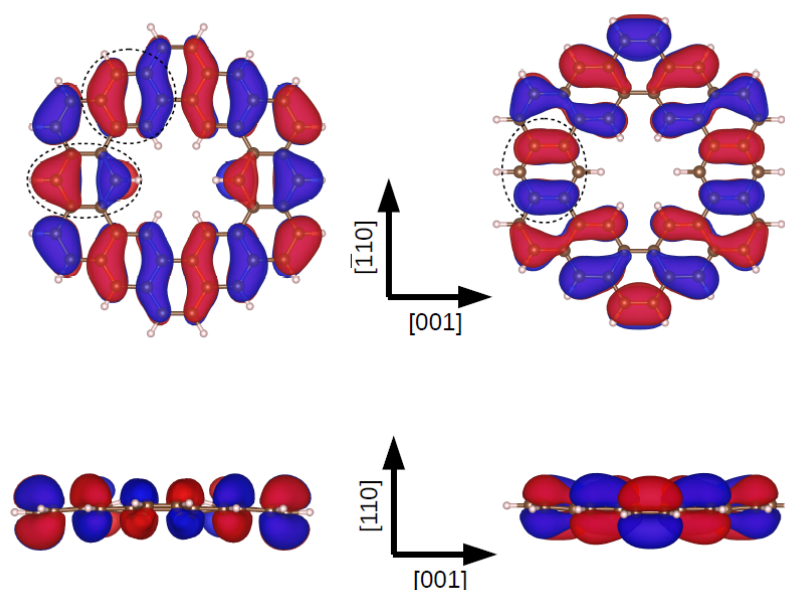


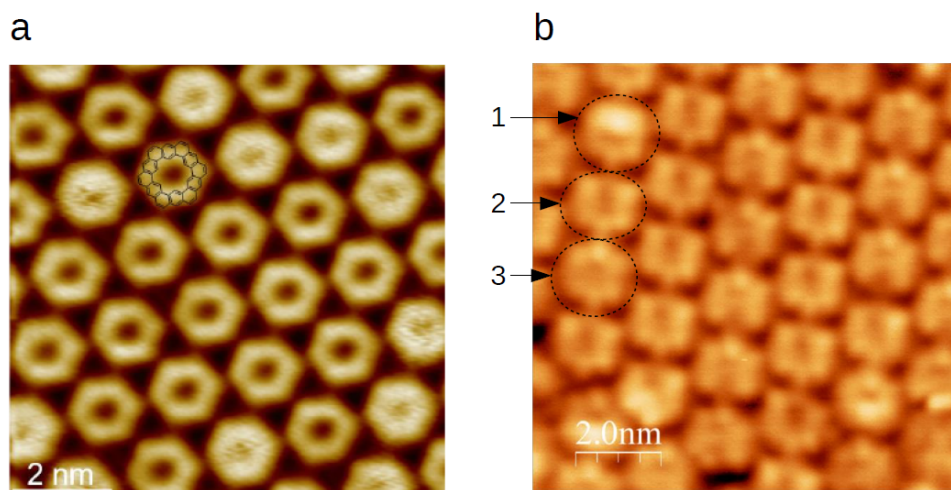
Fig. 3.23 The degenerate HOMO and HOMO-1 of the isolated kekulene molecule with the fixed geometry adsorbed on Cu(110).

From the real space distribution of the first two occupied molecular orbitals (HOMO/HOMO-1) it can be seen, that electronic inter-ring coupling still occurs in the kekulene structure after adsorption on the Cu(110) substrate. The same benzene like features (marked with dashed circles in Fig. 3.23), as in the case of the free kekulene molecule, are also visible. This means, even though the geometric structure shifted more towards the AWA model of aromaticity, the electronic structure of kekulene on Cu(110) still favors the Clar model.

3.2.5 Iso-kekulene

After analyzing the aromatic and electronic properties of kekulene/Cu(110), the actual on-surface synthesis of kekulene on Cu(110) should be discussed in more detail. When using the same on-surface synthesis process, used on Cu(111), as explained in Ref. [10], to create a monolayer of kekulene on Cu(110), the resulting STM image can be seen in Fig. 3.24. A comparison to the STM images of the monolayer of kekulene on Cu(111) has also been included.

In the case of the on-surface synthesis of kekulene on Cu(111) (cf. Fig. 3.24 (a)), planar kekulene-shaped rings can be seen, which leads to the conclusion that kekulene has successfully been synthesized on Cu(111). The brighter rings in the STM image of kekulene/Cu(111) are due to movement, induced by the scanning tip. However, in the case of the on-surface synthesis of kekulene on Cu(110) (cf. Fig. 3.24 (b)), a number of different surface species are visible. All surface species seem to be ring shaped, however, in some of them (first dashed circle) parts are sticking out of the surface, while on other (second dashed circle) part are missing, or lying more inwards, closer to the Cu(110) substrate. There are also some surface species (third dashed circle) which appear to be planar and therefore resemble kekulene the most.



3.24 (a) STM image of kekulene/Cu(111) taken from Ref. [10]. (b) yet unpublished STM image ($U = -1$ V, $I = 0.2$ nA and $T = 100$ K) of kekulene/Cu(110) produced by Qitang Fan and Michael Gottfried of Philipps-University of Marburg. The dashed circle show that at least three different molecular species are observed on the Cu(110) substrate. 1: is believed to be the iso-kekulene molecule in its up-configuration (cf. Chapter 3.2.5), indicated by the bright spot indicating atoms sticking out of the surface. 2: is believed to be the iso-kekulene molecule in its down-configuration, indicated by one benzene ring being not visible, 3: is believed to be kekulene, indicated by its uniformity.

The surface species, which have been considered the most relevant in the case of Cu(110), is the so called “iso-kekulene”, which is depicted in Fig. 3.25. “Iso-kekulene” is supposed to be an isomer of kekulene and hence has the same number of carbon atoms, arranged in a similar structure to kekulene. One of the benzene units, that in Fig. 3.25 is depicted as the upper middle benzene unit, which is why it will be referred here as the upper benzene unit, is pointing towards the center as compared to kekulene, where it is pointing away from the center. Because of steric hindrance, this benzene unit has to bend. This bend can be either away from the substrate, which will be called “iso-kekulene up” or towards the substrate, which will be called “iso-kekulene down”.

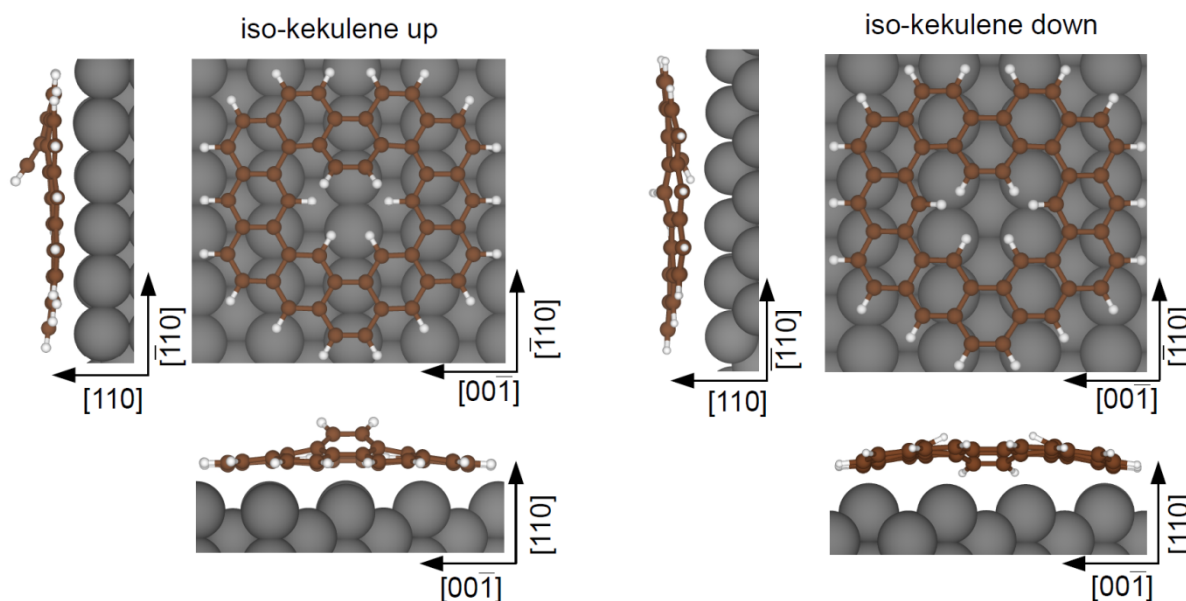


Fig. 3.25 Structural model of “iso-kekulene up”, in the short bridge adsorption position (left) and “iso-kekulene down”, in the hollow adsorption position (right). For both molecules, the side views along $[\bar{1}10]$ and $[00\bar{1}]$, respectively, are also shown.

The equilibrium adsorption geometry of the two “iso-kekulene” configurations has been calculated similar to the case of kekulene/Cu(110) (cf. Chapter 3.2.2). The same four adsorption positions as in Chapter 3.2.2 have been investigated, but the azimuthal orientation was kept the same, as in the case of the most favorable configuration of kekulene/Cu(110) (orientation 1). It has to be noted, however, that both “iso-kekulene” configurations have been calculated in the (6,0/3,4)-LEED unit cell, because it fits better with experimental STM results and therefore the total energy is not directly comparable to the one in Tab. 3.6. The average carbon height, the total energy and the difference in total energy were compared and can be seen in Tab. 3.8.

Tab. 3.8 Adsorption height and difference in total energy of iso-kekulene up and down on Cu(110) obtained for the four different adsorption positions. The azimuthal orientation of the molecules have been kept the same as the most favorable adsorption geometry of kekulene/Cu(110) in Tab. 3.6 (orientation 1).

	Adsorption position	$h_c[\text{Å}]$	$E[\text{eV}]$	$\Delta E[\text{eV}]$
iso-kekulene up	top	2.69	-979.38	1.09
	short bridge	2.59	-979.76	0.71
	long bridge	2.48	-980.47	0
	hollow	2.57	-980.43	0.43
iso-kekulene down	top	2.87	-978.87	1.44
	short bridge	2.87	-978.97	1.34
	long bridge	2.67	-979.79	0.52
	hollow	2.60	-980.31	0

It can be seen that for “iso-kekulene up”, the long bridge adsorption position is the most favorable, similar to kekulene/Cu(110). It has to be noted that the vertical corrugation of “iso-kekulene up”, in its most favorable adsorption configuration is 1.78 Å, meaning the upper benzene unit sticks 1.78 Å out of the plane. This is higher than any other adsorption position which has been investigated here. Indeed, the 2 least favorable positions (the top and short bridge position) only have a vertical corrugation of 1.21 Å and 1.18 Å, respectively. The hollow position, however, is similar to the long bridge position and the vertical corrugation of “iso-kekulene“ has been measured to 1.73 Å. So it would seem, that the upper benzene unit is sticking out of the plane the most, for the energetically more favorable adsorption configurations of “iso-kekulene up”.

For “iso-kekulene down”, however, the top adsorption position has shown to be the energetically most favorable. The vertical corrugation of iso-kekulene in this configuration has been calculated to be 1.05 Å. There seems to be no correlation between vertical corrugation and total energy in the case of iso-kekulene down, but there seems to be a larger gap in energy when comparing the hollow and long bridge position with the short bridge and top position.

3.2.6 Probe Particle Simulations

In order to further analyze the structures on the Cu(110) experimentally, which are formed after the on-surface synthesis, described in Ref. [10], high-resolution imaging techniques, such as nc-AFM or IETS-STM are necessary. To simulate nc-AFM and IETS-STM images of various surface species on Cu(110), as well as kekulene on Cu(111) (cf. Fig. 3.26), the probe particle model was used. On Cu(110), the investigated structures are kekulene (cf. Fig. 3.26), “iso-kekulene up” (cf. Fig. 3.27) and “iso-kekulene down” (cf. Fig. 3.27).

The simulations of nc-AFM and IETS-STM were performed with a CO probe particle. For the nc-AFM simulations, a bending stiffness in x and $y = 0.2$ N/m, a particle-tip bond length stiffness $R = 20$ N/m, an amplitude of the oscillation 1 \AA and a bias charge of the probe particle of $q = -0.05$ eV has been chosen. For the IETS-STM, the peak width was set to $\sigma = 0.7$ meV, following Ref. [83] and the bias offset has also been set to $V = -0.05$ eV.

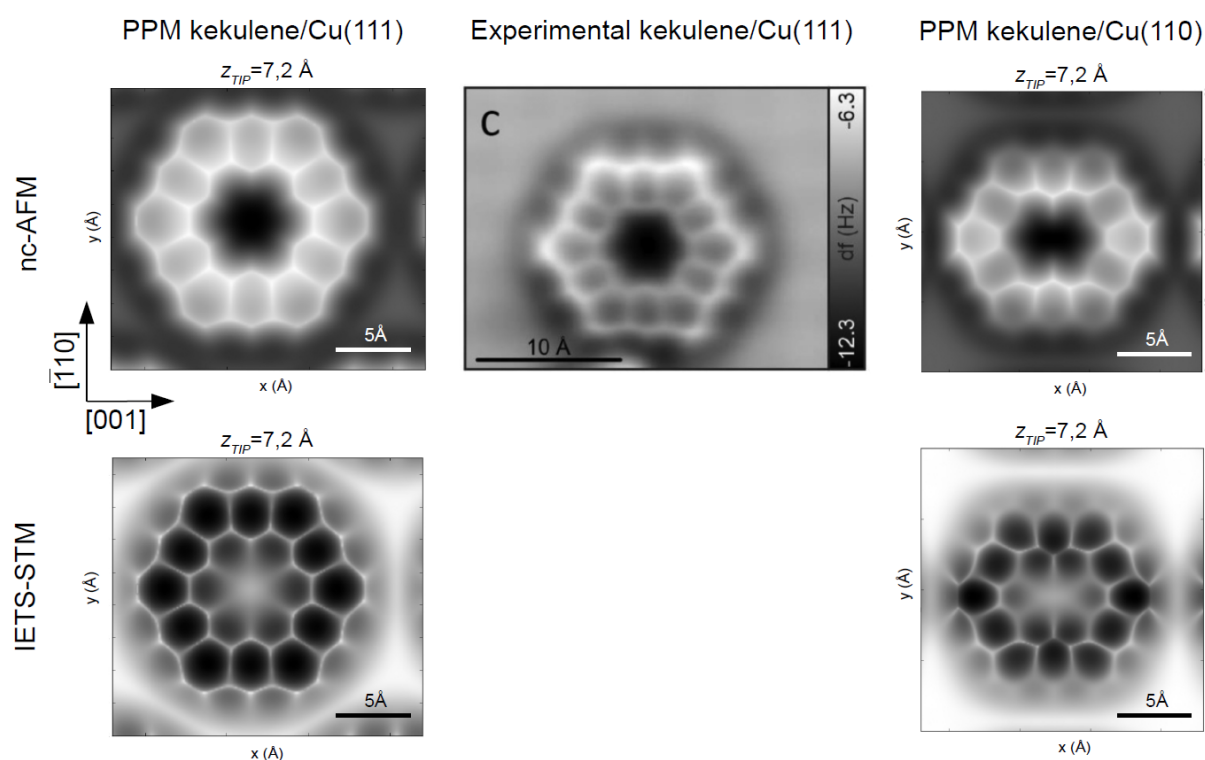


Fig. 3.26 Probe particle model (PPM) simulations for kekulene/Cu(111) (left) and kekulene/Cu(110) (right). The top row shows the nc-AFM simulations and the bottom row shows the IETS-STM simulations. The tip-sample distance in both cases is $z_{\text{tip}} = 7.2 \text{ \AA}$. The experimental nc-AFM image (center) is taken from Ref. [4].

The reference image of kekulene/Cu(111) show, that for both IETS-STM, as well as nc-AFM kekulene’s C-C bonds, as well as its C-H bonds are visible. The nc-AFM simulations are in good agreement to experimental nc-AFM images, from Ref. [4]. The tip-sample distances displayed in Fig. 3.26 are comparable to the ones in other PPM calculations^[78-81]. It can also be seen that the IETS-STM image only differ from the nc-AFM simulations in the imaging contrast and the resulting images are similar in shape and structure. In the case of kekulene/Cu(110), it can be seen that the distortion experienced by kekulene on Cu(110),

which has previously been calculated to be between 0.3 Å and 0.4 Å (cf. Chapter 3.2.2), is also visible using both IETS-STM, as well as nc-AFM simulations.

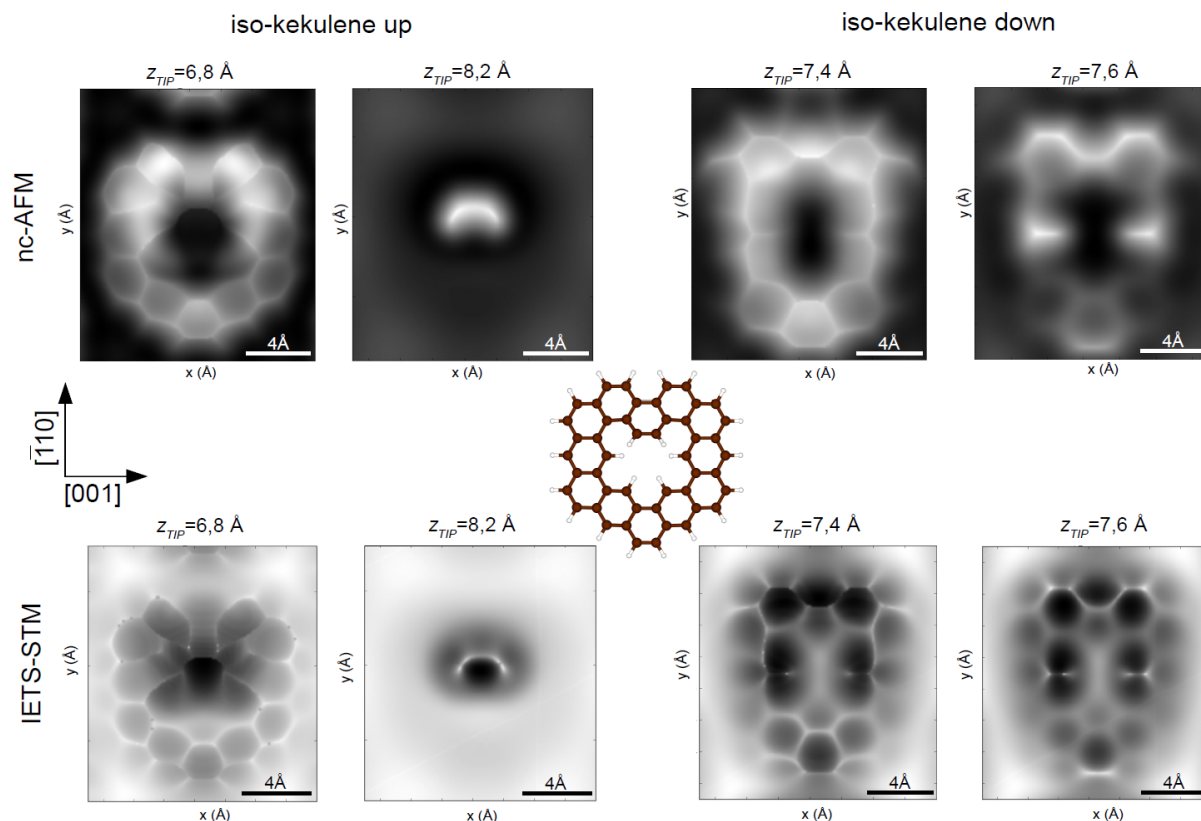


Fig. 3.27 Probe particle model simulation images for “iso-kekulene up” (left) and “iso-kekulene down” (right) on Cu(110). The top row shows the IETS-STM simulations and the bottom row shows the nc-AFM simulations.

IETS-STM and nc-AFM simulations of “iso-kekulene up” and “iso-kekulene down” revealed that these two configurations can be easily distinguished from another, as well as from kekulene, when performed on a Cu(110) substrate.

These IETS-STM and nc-AFM simulations may help identify kekulene-like structures on a Cu(110) substrate in nc-AFM and IETS-STM experiments.

3.2.7 Conclusions

The energetically most favorable adsorption configuration of the kekulene/Cu(110) system has been calculated to be the long bridge position, with kekulene's apothem parallel to the [001] orientation of the Cu(110) substrate. The adsorption energy in this configuration was calculated to be around -7.8 eV and the adsorption height to be roughly 2.4 Å. Projected density of states calculations as well as photoemission momentum maps showed that the LUMO is occupied and therefore charge transfer is expected. These findings give an indication that kekulene is chemisorbed on Cu(110).

Because of the two-fold nature of the Cu(110) substrate, also kekulene's geometric structure becomes clearly two-fold symmetric upon adsorption.

Geometric analysis of the aromaticity of the kekulene/Cu(110) system indicated that the adsorption tends to shift the aromatic structure of kekulene closer to the AWA model and away from the Clar model. However, after analyzing the real space distribution of the frontier orbitals, benzene-like structures, as well as inter-ring coupling of the inner and outer ring of kekulene indicate that the electronic structure of the Clar model is still the preferable choice.

When trying to create a monolayer of kekulene on Cu(110), the resulting STM images have shown that more than one surface species are present. One surface species of the on-surface synthesis of kekulene^[10], so-called "iso-kekulene", in its up and down configuration, has been shown to have a similar adsorption geometry as kekulene. However, the iso-kekulene down configuration has the hollow adsorption position as its energetically most favorable. In the case of iso-kekulene up, there seems to be a correlation of molecular vertical corrugation (upper benzene unit sticking out of the plane) and total energy, with the configuration in which the upper benzene unit sticks out the more have a lower total energy. However, further investigations are necessary to support this claim.

To better identify kekulene and other surface species of its synthesis, nc-AFM and IETS-STM simulations of kekulene as well as two other predicted surface species (iso-kekulene up and down) have been calculated, using the probe particle model. It has been found that using nc-AFM and IETS-STM these surface species can be distinguished from the kekulene molecules, which may help identify kekulene-like structures on a Cu(110) substrate in future nc-AFM and IETS-STM experiments.

4 Summary

In this thesis the polycyclic hydrocarbon kekulene ($C_{48}H_{24}$) has been investigated, including the two organic/metal interfaces kekulene/Cu(111) and kekulene/Cu(110). This investigation was conducted by a theoretical study and in addition comparisons to experimental data have been performed.

Firstly, the optimal adsorption configurations of both kekulene/Cu(111) and kekulene/Cu(110) have been determined. This has been done by calculating the equilibrium geometry of various adsorption configurations via DFT and comparing their total energy. The generalized gradient approximation (GGA) has been used as treatment of the exchange-correlation effects and the Van der Waals corrections have been performed according to Tkatchenko and Scheffler. For kekulene/Cu(111) the hollow hcp adsorption position with kekulene's apothem parallel to the $[\bar{1}12]$ direction of Cu(111) has been found to be the most favorable adsorption configuration. The adsorption height and the adsorption energy of this configuration are 3.05 Å and around -6 eV, respectively. The decrease in the work function of this configuration is $\Delta\Phi = -0.754$ eV. For kekulene/Cu(110) the long bridge adsorption position with kekulene's apothem parallel to the [001] direction of Cu(110) has been determined to be the most favorable adsorption configuration. The adsorption height and the adsorption energy of this configuration are 2.4 Å and around -7.8 eV, respectively. The decrease in the work function of this configuration is $\Delta\Phi = -0.576$ eV. These results lead to the conclusion that kekulene physisorbs on Cu(111) and chemisorbs on Cu(110).

Another goal of this thesis was to analyze the aromatic structure of kekulene. Previously, two different aromatic models have been postulated for describing kekulene's aromaticity, the Clar and the AWA (annulene-within-annulene) model, respectively. To investigate the aromatic structure of kekulene, two different methods have been employed. The first being the harmonic oscillation model of aromaticity (HOMA), which uses the geometric structure (bond lengths) of kekulene to derive its aromatic properties. The HOMA values of DFT optimized free kekulene and kekulene adsorbed on Cu(111) have been calculated and compared to HOMA values of two theoretical geometric structures, build to resemble the proposed Clar and AWA model. This comparison has indicated that the Clar model is the more proper description of kekulene's aromaticity.

The second method to investigate kekulene's aromaticity was done through its electronic structure. Kekulene's density of states, photoemission intensity and real space distribution of its frontier orbitals have been calculated. Photoemission momentum maps (k-maps) have been simulated and compared to experimental k-maps. The theoretical and experimental k-maps of kekulene/Cu(111) and kekulene/Cu(110) are in good agreement. Two electronic configurations, resembling the proposed Clar and AWA models, have been build using the simple Hückel molecular orbital model. Momentum maps of these electronic configurations

have been calculated and compared to the theoretical and experimental momentum maps of kekulene/Cu(111). In addition, the nodal structure and the charge density distribution of kekulene's frontier orbital have been compared between free kekulene and the electronic structures derived from the Hückel model. The investigation of the electronic structure has concluded, similar to the investigation of the HOMA, that the Clar model is the preferred description of kekulene's aromaticity.

Lastly, the on-surface synthesis of kekulene on Cu(110) has been analyzed, via STM. Various additional surface species besides kekulene can be observed on the Cu(110) substrate. One particular potential surface species, the so-called "iso-kekulene" was investigated more closely. The equilibrium geometry of "iso-kekulene" on Cu(110), in its two most logical configuration, "iso-kekulene up" and "iso-kekulene down" have been analyzed. The results have been similar to kekulene/Cu(110). To better identify kekulene-like structures on the surface of Cu(110), simulated nc-AFM and IETS-STM images have been created, by utilizing the probe particle model.

Appendix

The reference molecule for the calculations of the optimal bond length was chosen to be trans-1,3 butadiene, which is depicted in Fig. A.1. The reference molecule was geometrically optimized using the same methods as kekulene on Cu(111) and Cu(110) (cf. Chapter 3.1.2) using PBE-GGA exchange-correlation methods (bond length in blue), as well as B3LYP hybrid functionals (bond length in red).

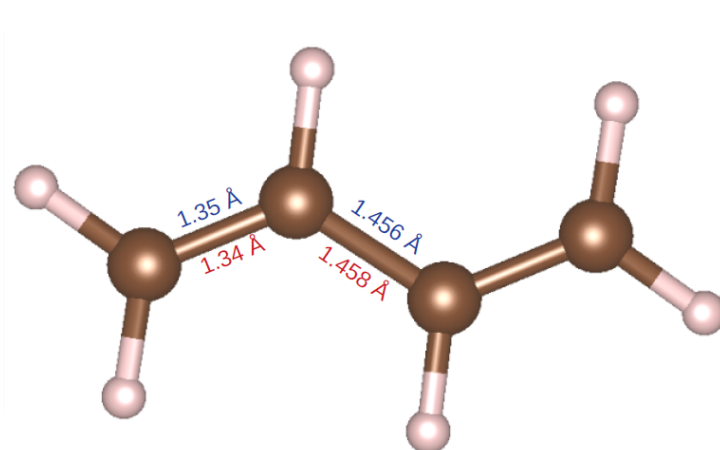


Fig. A.1 Chemical structure of trans-1,3 butadiene, the reference molecule which was used to derive the optimal bond length for HOMA calculations shown in Chapter 3.1.3 and Chapter 3.2.3. The bond lengths in blue represent the PBE-GGA calculated structure, while the bond lengths in red represent the structure given with B3LYP hybrid functionals.

For the PBE-GGA optimized free trans-1,3 butadiene (blue bond lengths) the calculated single bond is $R_{single} = 1.35 \text{ \AA}$ and the calculated double bond is $R_{double} = 1.456 \text{ \AA}$. The optimal bond length has then been calculated by averaging over the single and double bond to be $R_{opt} = 1.403 \text{ \AA}$.

For the B3LYP optimized free trans-1,3 butadiene (red bond lengths) the calculated single bond is $R_{single} = 1.34 \text{ \AA}$ and the calculated double bond is $R_{double} = 1.458 \text{ \AA}$. The optimal bond length has then been calculated to be $R_{opt} = 1.399 \text{ \AA}$.

Bibliography

- [1] August Kekulé. Sur la Constitution des substances aromatiques. *Bulletin de la Société chimique* **3**, 98-111, 1865
- [2] August Kekulé. Untersuchungen über aromatische Verbindungen. *Annalen der Chemie und Pharmacie* **137**(2), 129-196, 1866
- [3] Heinz A. Staab, François Diederich, Claus Krieger and Dieter Schweitzer. Cycloarenes, a New Class of Aromatic Compounds, II. Molecular Structure and Spectroscopic Properties of Kekulene. *Chemische Berichte* **116**(10), 1983
- [4] Iago Pozo, Zsolt Majzik, Niko Pavliček, Manuel Melle-Franco, Enrique Guitián, Diego Peña Leo Gross and Dolores Pérez. Revisiting Kekulene: Synthesis and Single-Molecule Imaging. *Journal of the American Chemical Society* **141**(39), 15488-15493, 2019
- [5] Alex W. Robertson, Gun-Do Lee, Kuang He, Chuncheng Gong, Qu Chen, Euijoon Yoon, Angus I. Kirkland and Jamie H. Warner. Atomic Structure of Graphene Subnanometer Pores. *ACS Nano* **9**(12), 11599-11607, 2015
- [6] François Diederich and Heinz A. Staab. Benzenoid versus Annulenoid Aromaticity: Synthesis and Properties of Kekulene. *Angewandte Chemie* **17**(5), 372-374, 1978
- [7] Claus Krieger, François Diederich, Dieter Schweitzer and Heinz A. Staab. Molecular Structure and Spectroscopic Properties of Kekulene. *Angewandte Chemie* **18**(9), 699-701, 1979
- [8] Erich Clar. The Aromatic Sextet. *Wiley*, 1972
- [9] Jun-ichi Aihara. Validity and Limitations of the Annulene-Within-An-Annulene (AWA) Model for Macrocyclic π -Systems. *RSC Adv.* **4**, 7256-7265, 2014
- [10] Anja Haags, Alexander Reichmann, Qitang Fan, Larissa Egger, Hans Kirschner, Tim Naumann, Simon Werner, Tobias Vollgraff, Jörg Sundermeyer, Lukas Eschmann, Xiaosheng Yang, Dominik Brandstetter, François C. Bocquet, Georg Koller, Alexander Gottwald, Mathias Richter, Michael G. Ramsey, Michael Rohlfing, Peter Puschnig, J. Michael Gottfried, Serguei Soubatch and F. Stefan Tautz. Kekulene: On-Surface Synthesis, Orbital Structure, and Aromatic Stabilization. *ACS Nano* **14**(11), 15766-15775, 2020
- [11] Max Born and Robert Oppenheimer. Zur Quantentheorie der Molekeln. *Annalen der Physik* **389**(20), 457-484, 1927
- [12] Peter Puschnig. Fundamentals of Electronic Structure Theory Lecture Notes. Available at http://physik.uni-graz.at/~pep/FEST_WS1819.html, 2018

- [13] Carlos Fiolhais, Fernando Nogueira, and Miguel A. L. Marques. A Primer in Density Functional Theory. *Springer*, 2003
- [14] Douglas R. Hartree. The Wave Mechanics of an Atom with a Non-Coulomb Central Field. Part I. Theory and Methods. *Proceedings of the Cambridge Philosophical Society* **24**(1), 89-110, 1928
- [15] John C. Slater. The Self Consistent Field and the Structure of Atoms. *Physical Review* **32**, 339–348, 1928
- [16] John C. Slater. Note on Hartree's Method. *Physical Review* **35**, 210–211, 1930
- [17] Vladimir A. Fock. Näherungsmethode zur Lösung des quantenmechanischen Mehrkörperproblems, *Zeitschrift für Physik* **61**, 126-148, 1930
- [18] Douglas R. Hartree and W. Hartree. Self-Consistent Field, with Exchange, for Beryllium. *Proceedings of the Royal Society A* **150**(869), 9-33, 1935
- [19] Pierre Hohenberg and Walter Kohn. Inhomogeneous Electron Gas. *Physical Review* **136**(3B), 864-871, 1964
- [20] Walter Ritz. Über eine neue Methode zur Lösung gewisser Variationsprobleme der mathematischen Physik. *Journal für die reine und angewandte Mathematik* **135**, 1-61, 1909
- [21] John William Strutt. The Theory of Sound, *Cambridge University Press*, volume 1, 2011
- [22] Mel Levy, John P. Perdew. The Constrained Search Formulation of Density Functional Theory. *Springer*, NATO ASI Series, volume 123, 1985
- [23] Walter Kohn and Lu Jeu Sham. Self-consistent equations including exchange and correlation effects. *Physical Review* **140**(4A), 1133-1138, 1965
- [24] Robert O. Jones and Olle Gunnarsson. The density functional formalism, its application and prospects. *Reviews of Modern Physics* **61**(3), 689-746, 1989
- [25] Walter Kohn. An essay on condensed matter physics in the twentieth century. *Review of Modern Physics* **71**(2), 59-77, 1999
- [26] Walter Kohn. Nobel lecture: Electronic structure of matter-wave functions and density functionals. *Review of Modern Physics* **71**(5), 1253-1266, 1999
- [27] David Sholl and Janice A. Steckel. Density Functional Theory: A Practical Introduction, *Wiley*, 2009

- [28] Richard M. Martin. *Electronic Structure: Basic Theory and Practical Methods*. Cambridge University Press, 2008
- [29] John P. Perdew and Alex Zunger. Self-interaction correction to density functional approximations for many-electron systems. *Physical Review B* **23**(10), 5048-5079, 1981
- [30] David M. Ceperley and Berni J. Alder. Ground State of the Electron Gas by a Stochastic Method. *Physical Review Letters* **45**(7), 566-569, 1980
- [31] John P. Perdew, Kieron Burke and Matthias Ernzerhof. Generalized Gradient Approximation Made Simple, *Physical Review Letters* **77**(18), 3865-3868, 1996
- [32] Axel D. Becke. A new mixing of Hartree-Fock and local density-functional theories. *The Journal of Chemical Physics* **98**(2), 1372-1377, 1993
- [33] Iann C. Gerber and János G. Ángyán. Hybrid functional with separated range. *Chemical Physics Letters* **415**(1-3), 100-105, 2005
- [34] Axel D. Becke. Density-functional thermochemistry. III. The role of exact exchange. *Journal of Chemical Physics* **98**(7), 5648-5652, 1993
- [35] P. J. Stephens, F. J. Devlin, C. F. Chabalowski and M. J. Frisch. Ab Initio Calculation of Vibrational Absorption and Circular Dichroism Spectra Using Density Functional Force Fields. *Journal of Chemical Physics* **98**(45), 11623-11627, 1994
- [36] K. Kim and K. D. Jordan. Comparison of Density Functional and MP2 Calculations on the Water Monomer and Dimer. *Journal of Chemical Physics* **98**(40), 10089-10094, 1994
- [37] Axel D. Becke. Density-functional exchange-energy approximation with correct asymptotic behavior. *Physical Review A* **38**(6), 3098-3100, 1988
- [38] Chengteh Lee; Weitao Yang; Robert G. Parr. Development of the Colle-Salvetti correlation-energy formula into a functional of the electron density. *Physical Review B* **37**(2), 785-789, 1988
- [39] S. H. Vosko; L. Wilk; M. Nusair. Accurate spin-dependent electron liquid correlation energies for local spin density calculations: a critical analysis. *Canadian Journal of Physics* **58**(8), 1200-1211, 1980
- [40] Johannes Diderik van der Waals. *Over de Continuïteit van den Gas- en Vloeistoftoestand*. (Dissertation), Universit t Leiden, 1873
- [41] Igor E. Dzyaloshinskii, Evgeny M. Lifshitz and Lev P. Pitaevskii. The General Theory of van der Waals Forces. *Advances in Physics* **10**(38), 165-209, 1961

- [42] Fritz London. The general theory of molecular forces. *Transactions of the Faraday Society* **33**, 8–26, 1937
- [43] Hugo C. Hamaker. The London-van der Waals Attraction between Spherical Particles. *Physica* **4**(10), 1058-1072, 1937
- [44] Alexandre Tkatchenko and Matthias Scheffler, Accurate Molecular Van Der Waals Interactions from Ground-State Electron Density and Free-Atom Reference Data. *Physical Review Letters* **102**(7), 073005, 2009
- [45] George Kresse and Jürgen Hafner. Ab initio molecular dynamics for liquid metals. *Physical Review B* **47**(1), 558-561, 1993
- [46] George Kresse and Jürgen Hafner. Ab initio molecular-dynamics simulation of the liquid-metal-amorphous-semiconductor transition in germanium. *Physical Review B* **49**(20), 14251-14269, 1994
- [47] George Kresse and Jürgen Furthmüller. Efficiency of ab-initio total energy calculations for metals and semiconductors using a plane-wave basis set. *Computational Materials Science* **6**(1), 15-50, 1996
- [48] George Kresse and Jürgen Furthmüller. Efficient iterative schemes for ab initio total-energy calculations using a plane-wave basis set. *Physical Review B* **54**(16), 11169-11186, 1996
- [49] Peter E. Blöchl. Projector augmented-wave method. *Physical Review B* **50**(24), 17953–17979, 1994
- [50] Peter E. Blöchl, Clemens J. Först and Johannes Schimpl. The Projector Augmented Wave Method: ab-initio molecular dynamics with full wave functions. *Bulletin of Materials Science* **26**(1), 33-41, 2003
- [51] George Kresse and Daniel Joubert. From ultrasoft pseudopotentials to the projector augmented-wave method. *Physical Review B* **59**(3), 1758-1775, 1999
- [52] N. Troullier and José Luriaas Martins. Efficient pseudopotentials for plane-wave calculations. *Physical Review B* **43**(3), 1993–2006, 1991
- [53] Dario Knebl. Shockley surface states from first principles. (Master's thesis), University of Graz, 2013
- [54] Georg Heimel, Lorenz Romaner, Egbert Zojer Jean-Luc Brédas. A theoretical view on self-assembled monolayers in organic electronic devices. *Proc. SPIE* **6999**, 2008
- [55] Gabriel Merino, Thomas Heine and Seifert Gotthard. The Induced Magnetic Field in Cyclic Molecules. *Chemistry: A European Journal* **10**(17), 4367-4371, 2004

- [56] Dani Setiawan, Elfi Kraka and Dieter Cremer. Quantitative Assessment of Aromaticity and Antiaromaticity Utilizing Vibrational Spectroscopy. *Journal of Organic Chemistry* **81**(20), 9669-9686, 2016
- [57] Jacek Kruszewski, Tadeusz Marek Krygowski. Definition of Aromaticity Basing on the Harmonic Oscillator Model. *Tetrahedron Letters* **13**(36), 3839–3842, 1972
- [58] Tadeusz Marek Krygowski. Crystallographic Studies of Inter- and Intramolecular Interactions Reflected in Aromatic Character of π -Electron Systems. *Journal of Chemical Information and Computer Science* **33**(1), 70–78, 1993
- [59] Tadeusz Marek Krygowski, Michal Cyranski. Separation of the Energetic and Geometric Contributions to the Aromaticity of π -Electron Carbocyclics. *Tetrahedron* **52**(5), 1713–1722, 1996
- [60] Tadeusz Marek Krygowski, Michal Cyranski. Separation of the Energetic and Geometric Contributions to the Aromaticity. Part IV. A General Model for the π -Electron Systems. *Tetrahedron* **52**(30), 10255–10264, 1996
- [61] Walter A. Harrison. Electronic Structure and the Properties of Solids. *Dover Publications*, 1989
- [62] Charles Kittel. Introduction to Solid State Physics (7th edition), *Wiley*, 1996
- [63] Albert Einstein. Über einen die Erzeugung und Verwandlung des Lichtes betreffenden heuristischen Gesichtspunkt. *Annalen der Physik* **322**(6), 132-148, 1905
- [64] Andrea Damascelli. Probing the Electronic Structure of Complex Systems by ARPES. *Phys. Scr.* **2004**(T109), 61-74, 2004
- [65] Andrea Damascelli, Zahid Hussain and Zhi-Xun Shen. Angle-resolved photoemission studies of the cuprate superconductors. *Rev. Mod. Phys.* **75**(2), 473-541, 2003
- [66] Peter Puschnig, Stephen Berkebile, Alexander J. Fleming, Georg Koller, Konstantin Emtsev, Thomas Seyller, John D. Riley, Claudia Ambrosch-Draxl, Falko P. Netzer and Michael G. Ramsey. Reconstruction of Molecular Orbital Densities from Photoemission Data. *Science* **326**(5953), 702-706, 2009
- [67] P. J. Feibelman, D.E. Eastman. Photoemission spectroscopy – correspondence between quantum theory and experimental phenomenology. *Phys. Rev. B.* **10**(12), 4932, 1974
- [68] Peter Puschnig and Daniel Lüftner. Simulation of angle-resolved photoemission spectra by approximating the final state by a plane wave: From graphene to polycyclic aromatic hydrocarbon molecules. *Journal of Electron Spectroscopy and Related Phenomena* **200**, 193 – 208, 2015
- [69] Peter Puschnig and Michael G. Ramsey. Photoemission Tomography: Valence Band Photoemission as a Quantitative Method for Investigating Molecular Films. *Encyclopedea of Interfacial Chemistry*, 380-391, 2018

- [70] Hannes Offenbacher, Daniel Lüftner, Thomas Ules, Eva Maria Reinisch, Georg Koller, Peter Puschnig and Michael G. Ramsey. Orbital tomography: Molecular band maps, momentum maps and the imaging of real space orbitals of adsorbed molecules. *Journal of Electron Spectroscopy and Related Phenomena* **204**, 92-101, 2015
- [71] S. Moser. An experimentalist's guide to the matrix element in angle resolved photoemission. *Journal of Electron Spectroscopy and Related Phenomena* **214**, 29-52, 2017
- [72] Daniel Lüftner, Simon Weiß, Xiaosheng Yang, Philipp Hurdax, Vitaliy Feyer, Alexander Gottwald, Georg Koller, Serguei Soubatch, Peter Puschnig, Michael G. Ramsey and F. Stefan Tautz. Understanding the photoemission distribution of strongly interacting two-dimensional overlayers, *Physical Review B* **96**(12), 123402, 2017
- [73] Erich Hückel. Quantentheoretische Beiträge zum Benzolproblem- I. Die Elektronenkonfiguration des Benzols und verwandter Verbindungen. *Zeitschrift für Physik* **70**, 204-286, 1931
- [74] Erich Hückel. Quantentheoretische Beiträge zum Benzolproblem- II. Quantentheorie der Induzierten Polaritäten. *Zeitschrift für Physik* **72**, 310-337, 1931
- [75] Erich Hückel. Quantentheoretische Beiträge zum Problem der Aromatischen und Ungesättigten Verbindungen. III. *Zeitschrift für Physik* **76**, 628-648, 1932
- [76] Erich Hückel. Die freie Radikale der Organischen Chemie. Quantentheoretische Beiträge zum Problem der Aromatischen und Ungesättigten Verbindungen. IV. *Zeitschrift für Physik* **83**, 632-668, 1933
- [77] Werner Kutzelnigg. What I Like About Hückel Theory. *Journal of Computational Chemistry* **28**(1), 25-34, 2016
- [78] Prokop Hapala, Ruslan Temirov, F. Stefan Tautz and Pavel Jelínek. Origin of High-Resolution IETS-STM Images of Organic Molecules with Functionalized Tips. *Physical Review Letters* **113**(22-28), 226101, 2014
- [79] Pavel Jelinek. High resolution SPM imaging of organic molecules with functionalized tips. *Journal of Physics: Condensed Matter* **29**(34), 343002, 2017
- [80] Prokop Hapala, Georgy Kichin, Christian Wagner, F. Stefan Tautz, Ruslan Temirov and Pavel Jelínek. Mechanism of high-resolution STM/AFM imaging with functionalized tips. *Physical Review B* **90**(8), 085421, 2014
- [81] Prokop Hapala, Martin Švec, Oleksandr Stetsovych, Nadine J. van der Heijden, Martin Ondráček, Joost van der Lit, Pingo Mutombo, Ingmar Swart and Pavel Jelínek. Mapping the electrostatic force field of single molecules from high-resolution scanning probe images. *Nature Communications* **7**, 11560, 2016
- [82] Prokop Hapala. URL: <https://github.com/ProkopHapala/ProbeParticleModel>, 15.01.2021

- [83] Chunchen Liu, María Eugenia Sandoval-Salinas, Yongseok Hong, Tullimilli Y. Gopalakrishna, Hoa Phan, Naoki Aratani, Tun Seng Herng, Jun Ding, Hiroko Yamada, Dongho Kim, David Casanova and Jishan Wu. Macrocyclic Polyradicaloids with Unusual Super-ring Structure and Global Aromaticity. *Chem.* **4**(7), 1586–1595, 2018
- [84] Jun-ichi Aihara, Masakazu Makino, Toshumasa Ishida and Jerry R. Dias. Analytical Study of Superaromaticity in Cycloarenes and Related Coronoid Hydro-carbons. *J. Phys. Chem. A.* **117**(22), 4688–4697, 2013
- [85] Roy MacWeeny. The Diamagnetic Anisotropy of Large Aromatic Systems: III Structures with Hexagonal Symmetry. *Proc. Phys. Soc., London, Sect. A* **64**(10), 921-930, 1951
- [86] Jun-ichi Aihara. On the Number of Aromatic Sextets in a Benzenoid Hydrocarbon. *Bull. Chem. Soc. Jpn.* **49**(5), 1429-14230, 1976
- [87] N. J. Simon, E. S. Drexler and R. R. Reed. Properties of copper and copper alloys at cryogenic temperatures. *Final report*, United States: N. p., Web., 1992
- [88] M. Valiev, E. J. Bylaska, N. Govind, K. Kowalski, T. P. Staatsma, H. J. J. Van Dam, D. Wang, J. Nieplocha, E. Apra, T. L. Wundus and W. A. de Jong. NWChem: A Comprehensive and Scalable Open-Source Solution for Large Scale Molecular Simulations. *Comput. Phys. Commun.* **181**(9), 1477-1489, 2010
- [89] Dominik Brandstetter, Xiaosheng Yang, Daniel Lüftner, F. Stefan Tautz and Peter Puschnig. kMap.py: A Python program for simulation and data analysis in photoemission tomography. *Comput. Phys, Commun.*, 107905, 2021
- [90] Wikipedia article: Kekulene. URL: <https://en.wikipedia.org/wiki/Kekulene>, 15.01.2021